

Discrete optics in inhomogeneous waveguide arrays

Dissertation
zur Erlangung des akademischen Grades
doctor rerum naturalium (Dr. rer. nat.)

vorgelegt dem Rat der Physikalisch-Astronomischen Fakultät
der Friedrich-Schiller Universität Jena
von Diplomingenieur Henrike Trompeter,
geboren am 9. April 1976 in Detmold

Gutachter

1. Prof. Dr. Falk Lederer
Institut für Festkörpertheorie und –optik
Friedrich-Schiller-Universität Jena
2. Prof. Dr. Roberto Morandotti
INRS-EMT
University of Quebec
3. Prof. Dr. George I. Stegeman
College of Optics & Photonics: CREOL & FPCE
University of Central Florida

Tag der letzten Rigorosumsprüfung: 28.04.2006

Tag der öffentlichen Verteidigung: 13.06.2006

Contents

1. Introduction	2
2. Basic equations	7
2.1. Maxwell's equations and the wave equation.....	7
2.2. Eigenvalue problem and band structure	8
3. Defects and interfaces in waveguide arrays	13
3.1. Coupled mode theory	13
3.2. Homogeneous waveguide arrays.....	17
3.3. Localized states at defect waveguides.....	19
3.3.1 Theory.....	19
3.3.2 Experiment.....	23
3.3.3 Bound states at the edges of waveguide arrays.....	27
3.4. LiNbO ₂ optical switch.....	29
3.4.1 Analytical investigations.....	30
3.4.2 BPM-simulations	33
3.5. Interfaces in waveguide arrays.....	36
3.5.1 Bound states at interfaces	37
3.5.2 Reflection and transmission at interfaces	40
4. Photonic Zener tunnelling in planar waveguide arrays	46
4.1. Theory	46
4.2. Experiment and discussion.....	59
5. Bloch oscillation and Zener tunnelling in two-dimensional photonic lattices	72
5.1. Optically induced index changes in photorefractive crystals.....	73
5.2. Preparations.....	76
5.3. Results of simulations and experiments	82
6. Conclusions	90
7. Bibliography	93

1. Introduction

Optics is one of the oldest branches of physics. For a long time its focus laid on imaging systems, but during the last century this changed. With the investigation of new materials optics found its way into signal transfer and processing. Fibre-optic cables revolutionized telecommunications. One of the most recently introduced fields of research is optics in artificial materials, nano-structures with optimized properties. Analogue to the advances in semiconductor physics, which have allowed us to tailor the conducting properties of certain materials and thereby initiated the transistor revolution in electronics, artificial materials now allow to tailor as well the propagation of light.

One example of artificial materials are so called meta materials, sub-wavelength structures, where e.g. refraction and diffraction can be varied to a large extent [Pendry03]. Photonic crystals are another prominent example. They are periodic structures, where light propagation may be strongly affected and even controlled [Notomi00, Freymanna03]. Waveguide arrays are simpler but also promising candidates, where light propagation can be considerably modified compared with that in bulk materials. Planar or one-dimensional waveguide arrays are periodic in one transverse direction and translational invariant with respect to the direction of propagation while two-dimensional arrays are periodically modulated in both transverse directions. The gap between photonic crystals and waveguide arrays is bridged by photonic crystal fibres, which are periodic in transverse direction. Hence, some of the effects investigated in waveguide arrays can likewise be observed in photonic crystal fibres.

Currently linear and nonlinear dynamics in discrete or periodic optical systems as waveguide arrays are subject of active research. Due to the periodic nature of these systems many

similarities with quantum-mechanics or solid state physics are found, what is often reflected in the terminology for their description. Particles in periodic potentials as electrons in crystalline solids or custom-made semiconductor superlattices, Bose-Einstein condensates in optical lattices as well as photons in periodic refractive index structures have energies confined to bands in momentum space, which may be separated by gaps [Bloch28]. The periodicity of these systems leads to new and exciting effects.

If the light inside the array is well confined to the waveguides and the evolution of the light is restricted to the energy transfer between the evanescent tails (tight binding) we speak of a *discrete* system. Discrete diffraction and refraction in homogeneous arrays were demonstrated to deviate considerably from that in bulk materials [Somekh73, Eisenberg98, Pertsch02]. Experiments mainly have been performed in one-dimensional polymer or semiconductor arrays and in photonic lattices in photorefractive crystals. Recently first experimental observations on two dimensional discrete optical systems have been reported [Pertsch04, Fleischer03].

After the investigation of homogeneous arrays, inhomogeneous structures started to attract attention. First investigations of inhomogeneous waveguide arrays disclosed that the optical field performs photonic Bloch-oscillations across the array if an additional transverse force is produced by a transverse linear refractive index gradient [Pertsch99, Morandotti99].

Hence the waveguide array itself can be regarded as an artificial, tailor-made material with new, peculiar properties. In particular it is worthwhile to study how arrays perform as basic materials of waveguide optics.

The aim of this work is to investigate theoretically as well as experimentally the propagation of waves in inhomogeneous waveguide arrays. To this end the propagation in two different types of waveguides arrays, either with a local inhomogeneity or with a superimposed transverse refractive index gradient, is analysed.

In chapter 1 an introduction into the topics, discussed in this work is presented. The basic equations to describe propagation inside a waveguide array are Maxwell's equations. They are introduced in chapter 2, where also the eigenvalue problem for waveguide arrays is derived.

In chapter 3 the localization and reflection of light at inhomogeneities or more precisely defects and interfaces in waveguide arrays are investigated. Where light spreads in homogeneous arrays, it is reflected [Morandotti03] or trapped [Peschel99] by inhomogeneities. Defect modes can have new and exciting properties as it is demonstrated for photonic crystal fibres. In these structures single mode operation is obtained in a huge wavelength domain [Birkls97], extremely small [Russel03] or large [Knight98] effective mode areas are achieved and almost arbitrary values of the group velocity dispersion [Mogilevtsev98] can be reached. In this work basic features of defect

and interface modes in waveguide arrays are investigated where the existence of various types of guided modes is predicted by means of a coupled mode theory and experimentally confirmed in polymer waveguide arrays. To this end a single waveguide and its spacing to adjacent waveguides was varied with respect to the otherwise homogeneous array. The existence of four different types of bound states is predicted and experimental examples for each of them are given. Furthermore, an optical switch based on an electro-optically controllable defect is theoretically investigated as an example for an application of defect modes. For this purpose a lithium niobate waveguide array is analyzed, where an electric field is induced by electrodes and changes the refractive index for a transversely localized area that contains two waveguides. By applying different voltages to the electrodes the light propagation inside the array can be strongly influenced and switching or beam steering can be realized. Interfaces are induced into waveguide arrays by an abrupt change of the waveguides effective index and spacing. The conditions for the existence of interface modes, which are not known from conventional bulk media, are calculated analytically. Furthermore, the reflection and transmission coefficients of interfaces are determined.

The topic of chapter 4 is photonic Zener tunnelling. Zener tunnelling was originally predicted for an electron moving in a periodic potential with a superimposed constant electric field. Since many decades particle dynamics in periodic potentials or lattices has been an exciting subject of research in various branches of physics. It is known that in this environment the particle's energy is confined to bands in momentum space, which may be separated by gaps. On the basis of Bloch's theory [Bloch28] Zener predicted in 1934 [Zener34] that for this scenario electron wave packets do not delocalize but undergo periodic oscillations (Bloch oscillations). Zener argued that Bloch oscillations do not persist forever, but are damped by e.g. interband transitions, an effect, which is now called Zener tunnelling.

In spite of the early prediction of Bloch oscillations their unambiguous experimental verification failed for many decades. The reason was that these oscillations to appear require the coherence of wave functions, usually destroyed by particle-particle scattering in bulk semiconductors. In 1960 Wannier [Wannier60] proved that Bloch oscillations are evoked by the superposition of spatially localized states with equally spaced discrete energy levels (Wannier-Stark ladder - WSL), thus paving the way for spectroscopic measurements. However, only the invention of semiconductor superlattices (SLs) [Esaki70] led to the observation of electronic WSLs [Mendez88] and Bloch oscillations [Feldmann92]. Moreover, accounting for the fact that these fundamental effects require only a Bloch particle/wave (coherent wave in a lattice) exposed to a linear potential they have been proven in other physical settings as e.g. ultra-cold atoms in

accelerated optical lattices [Dahan96], photons in photonic lattices [Pertsch99a, Morandotti99], i.e. dielectric waveguide arrays, or superlattices [Sapienza03, Agarwal04], i.e. multilayer stacks (or 1D photonic crystals) with coupled cavities.

Zener breakdown of Bloch oscillations is expected to happen when the energy difference imposed on a period of the periodic lattice by the linear potential reaches the order of the gap between the bands. It sets a tight upper frequency limit to THz radiation generated by Bloch-oscillations. In view of applications the control of this breakdown is even more relevant, because in contrast to ideal Bloch oscillations it induces a DC current of particles. Examples are the electrical breakdown in dielectrics [Zener34] or in Zener diodes (see [Esaki74] and references therein), electrical conduction along nanotubes [Bourlon04] and through SLs [Sibille98], pair tunnelling through Josephson junctions [Ithier05] and spin tunnelling in molecular magnets [Paulsen95]. In some experiments the different time constants of the decay of Bloch oscillations and spectral broadening of the resonances were attributed to Zener tunnelling [Sibille98]. However, despite of the impressive progress of spectral transmission measurements in biased semiconductor SLs [Rosam01], it remains difficult to distinguish Zener tunnelling from the unavoidable dephasing, which also limits the lifetime of Bloch oscillations performed by e.g. electrons or cold atoms.

Unlike electrons photons may overcome this limit, because photon-photon interactions caused by optical nonlinearities can be neglected for common intensity levels. This has been proven by the observation of Zener tunnelling in spectral and time-resolved transmission measurements in photonic SLs composed of a Bragg mirror with chains of embedded defects of linearly varying resonance frequency [Ghulinyan05]. In this experiment it was attempted to create an identical environment for photons as electrons encounter in semiconductor SLs. Both enhanced transmission peaks and damped Bloch oscillations due to Zener tunnelling have been observed. But optics can even do better in really providing a laboratory for a direct visual observation of Bloch oscillations and Zener tunnelling. This has been verified in recent experiments on photonic Bloch oscillations [Pertsch99a, Morandotti99] in waveguide arrays. There the lattice was formed by an array of evanescently coupled waveguides, where the external potential was mimicked by a linear variation of the effective indices of the modes. This can be achieved by either applying a temperature gradient across a thermo-optic material [Pertsch99a] or by changing the waveguide geometry [Morandotti99]. The major difference to the common SL setup is that the temporal dynamics of the photons is mapped onto the spatial evolution of light along the propagation direction. Thus instead of having to resolve fast temporal oscillations and transmission spectra one can easily follow the path of light down the array.

In this work the first direct visual observation of Zener tunnelling and the associated decay of Bloch oscillations are presented. To this end light is fed into the waveguide array and its propagation along the sample is visualized by monitoring the optical fluorescence above of the array. By simultaneously heating and cooling the opposite array sides the required transverse index gradient, which stimulated Bloch oscillations, is achieved by the thermo-optic effect in polymer waveguide arrays. For an increasing index gradient a comprehensive picture of the coherent tunnelling phenomena to higher order bands, viz. Zener tunnelling, associated with the decay of Bloch oscillations is directly observed.

Furthermore, the first demonstration of Bloch oscillations and Zener tunnelling in a two dimensional lattice is presented. For this purpose a two-dimensional grating and an index gradient are optically induced in a photorefractive crystal [Efremidis02, Fleischer03, Neshev03]. The propagation of a light beam in the resulting structure is investigated by measuring the intensity distribution at the output facet of the crystal. In accordance with detailed numerical simulations, the measurements give clear evidence of 2D Bloch Oscillations and Zener tunnelling. Moreover the motion of the light beams was also detected directly in Fourier space. The measurements demonstrate the motion of a light beam through the first Brillouin zone corresponding to Bloch oscillations in real space for the first time. Additionally they provide important information about the tunnelling process into higher order bands.

2. Basic equations

Starting from Maxwell's equations the basic equations to describe light propagation in periodic systems are introduced. The evolution of the electric field is described by the wave equation. Furthermore, the eigenvalue problem is derived for a planar waveguide array. Its solution provides the characteristic information of a periodic system as the band structure and Bloch modes. The general results of this chapter provide the basis for more detailed investigations in the following chapters of this work.

2.1. Maxwell's equations and the wave equation

Maxwell's equations are the basis for the description of the propagation of light. In a dielectric medium, in which there are no free electric charges or currents, they can be written in Fourier space for monochromatic fields as

$$\begin{aligned}\nabla \times \mathbf{E}(\mathbf{r}, \omega) &= i\omega \mathbf{B}(\mathbf{r}, \omega), & \nabla \times \mathbf{H}(\mathbf{r}, \omega) &= -i\omega \mathbf{D}(\mathbf{r}, \omega), \\ \nabla \cdot \mathbf{D}(\mathbf{r}, \omega) &= 0, & \nabla \cdot \mathbf{H}(\mathbf{r}, \omega) &= 0.\end{aligned}\tag{1}$$

$\mathbf{E}(\mathbf{r}, \omega)$ and $\mathbf{H}(\mathbf{r}, \omega)$ are the electric and magnetic fields, $\mathbf{D}(\mathbf{r}, \omega)$ is the dielectric displacement and $\mathbf{B}(\mathbf{r}, \omega)$ the magnetic induction at a fixed frequency ω . The influence of the material and thus the relation between the different electric as well as the different magnetic variables is described for non magnetic materials by the equations

$$\begin{aligned}\mathbf{D}(\mathbf{r}, \omega) &= \varepsilon_0 \mathbf{E}(\mathbf{r}, \omega) + \mathbf{P}(\mathbf{r}, \omega), \\ \mathbf{B}(\mathbf{r}, \omega) &= \mu_0 \mathbf{H}(\mathbf{r}, \omega).\end{aligned}\tag{2}$$

ϵ_0 is the dielectric constant, μ_0 the magnetic permeability of vacuum and $\mathbf{P}(\mathbf{r}, \omega)$ the polarization. Because we investigate linear waveguide arrays, no nonlinear contributions exist and we can express the polarization as $\mathbf{P}(\mathbf{r}, \omega) = \epsilon_0 \chi(\mathbf{r}, \omega) \mathbf{E}(\mathbf{r}, \omega) = \epsilon_0 [\epsilon(\mathbf{r}, \omega) - 1] \mathbf{E}(\mathbf{r}, \omega)$, where $\chi(\mathbf{r}, \omega)$ is the susceptibility and $\epsilon(\mathbf{r}, \omega)$ the dielectric function. Since waveguide optics usually deals with non-magnetic materials no magnetization is assumed and the magnetic permeability is always identical to that of vacuum μ_0 . In general the variables in Fourier space are connected to the variables in real space by a Fourier transformation. Because we investigate monochromatic fields at a fixed frequency ω , the electro-magnetic fields can be written in the following form

$$\hat{\mathbf{V}}(\mathbf{r}, t) = \text{Re}\{\mathbf{V}(\mathbf{r}, \omega)e^{-i\omega t}\}. \quad (3)$$

Inserting eq. (2) in eq. (1) and eliminating $\mathbf{B}(\mathbf{r}, \omega)$ and $\mathbf{D}(\mathbf{r}, \omega)$ gives us a set of equations for the electric and magnetic fields

$$\begin{aligned} \nabla \times \mathbf{E}(\mathbf{r}, \omega) &= i\omega\mu_0 \mathbf{H}(\mathbf{r}, \omega), & \nabla \times \mathbf{H}(\mathbf{r}, \omega) &= -i\omega\epsilon_0 \epsilon(\mathbf{r}, \omega) \mathbf{E}(\mathbf{r}, \omega), \\ \nabla \cdot [\epsilon(\mathbf{r}, \omega) \mathbf{E}(\mathbf{r}, \omega)] &= 0, & \nabla \cdot \mathbf{H}(\mathbf{r}, \omega) &= 0. \end{aligned} \quad (4)$$

From this set of equations the wave equation is derived by taking the curl of the first of these four equations and then inserting $\nabla \times \mathbf{H}(\mathbf{r}, \omega)$. In the following $\nabla \cdot \mathbf{E}(\mathbf{r}, \omega)$ is expressed through

$$\nabla \cdot \mathbf{E}(\mathbf{r}, \omega) = -\frac{\nabla \epsilon(\mathbf{r}, \omega)}{\epsilon(\mathbf{r}, \omega)} \mathbf{E}(\mathbf{r}, \omega) \quad (5)$$

and we obtain

$$\Delta \mathbf{E}(\mathbf{r}, \omega) + \epsilon(\mathbf{r}, \omega) \frac{\omega^2}{c^2} \mathbf{E}(\mathbf{r}, \omega) + \nabla \{[\nabla \ln \epsilon(\mathbf{r}, \omega)] \mathbf{E}(\mathbf{r}, \omega)\} = 0. \quad (6)$$

Here $c = 1/\sqrt{\epsilon_0\mu_0}$ is the vacuum speed of light and Δ the Laplacian operator

$$\Delta = \frac{\partial^2}{\partial x^2} + \frac{\partial^2}{\partial y^2} + \frac{\partial^2}{\partial z^2}. \quad (7)$$

The wave equation (6) describes the propagation of the electric field $\mathbf{E}(\mathbf{r}, \omega)$. $\mathbf{H}(\mathbf{r}, \omega)$ can be calculated from $\mathbf{E}(\mathbf{r}, \omega)$ with the help of Maxwell's equations.

2.2. Eigenvalue problem and band structure

In this section the eigenvalue equation is derived for a one-dimensional waveguide array (see Fig. 1), which is homogeneous in the propagation direction z , periodic in x and finite in y .

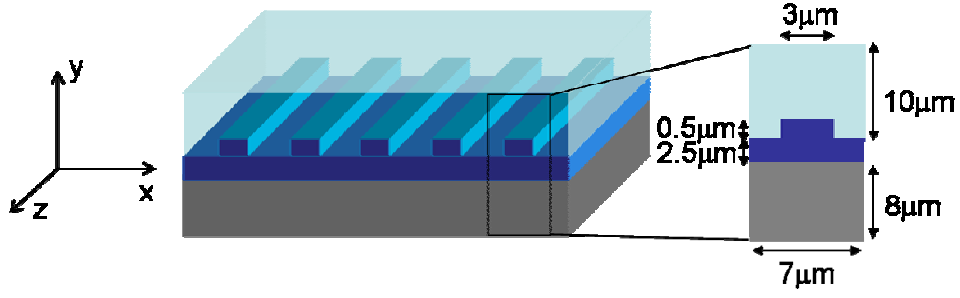


Fig. 1. Schematic representation of a polymer waveguide array with typical values of the geometry.

In the following we only consider monochromatic fields and thus omit the frequency ω in the corresponding arguments. We insert stationary propagating fields

$$\mathbf{E}(\mathbf{r}) = \mathbf{E}_0(x, y)e^{i\beta z} \quad (8)$$

into eq. (6) and obtain

$$\left[-\beta^2 + \Delta_t\right] \mathbf{E}_0(x, y) + \boldsymbol{\varepsilon}(x, y) \frac{\omega^2}{c^2} \mathbf{E}_0(x, y) + (\nabla_t + i\beta \mathbf{u}_z) [\nabla_t \ln \boldsymbol{\varepsilon}(x, y) \mathbf{E}_0(x, y)] = 0. \quad (9)$$

$\nabla_t = \mathbf{u}_x \partial_x + \mathbf{u}_y \partial_y$ and $\Delta_t = \partial_x^2 + \partial_y^2$ are the transverse Nabla and Laplace operator and β the longitudinal wave number. \mathbf{u}_x , \mathbf{u}_y and \mathbf{u}_z are the unit vectors in x -, y - and z -direction. The first term of this equation includes the evolution during propagation and diffraction, while the influence of the periodic modulation of $\boldsymbol{\varepsilon}(x, y)$ is given by the second term. The last term mixes between the different vector components of the electric field $\mathbf{E}(\mathbf{r})$. In this equation the transverse components decouple from the z -component and an equation for $\mathbf{E}_t(x, y)$, which contains the x - and y -components of the electric field only, can be determined as

$$\left[-\beta^2 + \Delta_t\right] \mathbf{E}_t(x, y) + \boldsymbol{\varepsilon}(x, y) \frac{\omega^2}{c^2} \mathbf{E}_t(x, y) + \nabla_t \left\{ [\nabla_t \ln \boldsymbol{\varepsilon}(x, y)] \mathbf{E}_t(x, y) \right\} = 0. \quad (10)$$

For periodicity in x -direction the dielectric function $\boldsymbol{\varepsilon}(x, y) = \boldsymbol{\varepsilon}(x + d, y)$ and $\ln \boldsymbol{\varepsilon}(x, y) = \ln \boldsymbol{\varepsilon}(x + d, y)$ can be expanded into Fourier series

$$\boldsymbol{\varepsilon}(x, y) = \sum_{m=-\infty}^{\infty} \boldsymbol{\varepsilon}_m(y) e^{igmx} \quad \text{and} \quad \ln \boldsymbol{\varepsilon}(x, y) = \sum_{m=-\infty}^{\infty} \mathbf{l}_m(y) e^{igmx}, \quad (11)$$

with g being the absolute value of the normalized grating vector $\mathbf{g} = \mathbf{u}_x 2\pi/d$. The transverse electric field vector is expanded into plane waves and thus can be written as

$$\mathbf{E}_t(x, y) = \int_{-\infty}^{+\infty} \mathbf{E}_t(k, y) e^{ikx} dk, \quad (12)$$

with the transverse wave number k . For reasons of simplicity, we distinguish the quantities in real and Fourier space only by their arguments. The eigenvalue problem for the eigenvalue β^2 can be derived. Therefore eqs. (11) and (12) are inserted into eq. (10) and

$$\int_{-\infty}^{+\infty} \left\{ -(\beta^2 + k^2 + \frac{\partial^2}{\partial y^2}) \mathbf{E}_t(k, y) + \sum_m \boldsymbol{\varepsilon}_m \frac{\omega^2}{\varepsilon^2} \mathbf{E}_t(k - mg, y) + \sum_m \left[ik \mathbf{u}_x + \mathbf{u}_y \frac{\partial}{\partial y} \right] \left[igm E_x(k - mg, y) \mathbf{I}_m + \left(\frac{\partial}{\partial y} \mathbf{I}_m \right) E_y(k - mg, y) \right] \right\} e^{ikx} dk = 0 \quad (13)$$

follows after substituting $k' = k + igm$ for terms containing $\exp(i(k + mg)x)$ and renaming k' into k . E_x and E_y are the x - and y -component of \mathbf{E}_t . Because this equation must hold for all values of k , the integrand itself must be zero. Then the eigenvalue problem can be written for $-g/2 \leq k_0 \leq g/2$ as

$$\beta^2(k_0) \tilde{\mathbf{E}}_t(k_0, y) = \mathbf{M}(k_0, y) \tilde{\mathbf{E}}_t(k_0, y) \quad \text{with} \quad \tilde{\mathbf{E}}_t(k_0, y) = \begin{pmatrix} \vdots \\ \mathbf{E}_t(k_0 + g, y) \\ \mathbf{E}_t(k_0, y) \\ \mathbf{E}_t(k_0 - g, y) \\ \vdots \end{pmatrix}, \quad (14)$$

where $\tilde{\mathbf{E}}_t(k_0, y)$ is the eigensolution to the eigenvalue $\beta^2(k_0)$ and $\mathbf{M}(k_0, y)$ an operator, which follows from eq. (13). Each $\mathbf{E}_t(k_0, y)$ is connected only to Fourier components at $k_0 + mg$ with $-\infty < m < +\infty$. Therefore the corresponding solution in real space, which we denote as $\mathbf{E}_{t, k_0}(x, y)$, can be written as a product of an x -periodic contribution $\boldsymbol{\Psi}_{k_0}(x, y) = \boldsymbol{\Psi}_{k_0}(x + d, y)$ and a phase term $e^{ik_0 x}$

$$\mathbf{E}_{t, k_0}(x, y) = \sum_m \mathbf{E}_{t, m}(k_0 - mg, y) e^{-imgx} e^{ik_0 x} = \boldsymbol{\Psi}_{k_0}(x, y) e^{ik_0 x}. \quad (15)$$

This conclusion is known as *Bloch theorem* with k_0 being the *Bloch vector* of the *Bloch wave* $\mathbf{E}_{t, k_0}(x, y)$.

In the following we examine the dependence of the propagation constant β on the Bloch vector k_0 . For each k_0 a discrete number of solutions β can be calculated. We distinguish these solutions by their indices n . All solutions β_n with the same index n are accounted to one so-called band. Therefore n is called band index. The relation between the transverse wave number k_0 and the longitudinal wave number β (drawn in the β - k_0 -plane) is called band

structure or diffraction relation. The areas of the band structure, where no propagation constants β exist for any value of k_0 , are called band gaps. Obviously the band structure has to be periodic in k_0 with a period of g . Therefore it is sufficient to examine only one period of the band structure. We use the interval $-g/2 \leq k_0 \leq g/2$, which is called first Brillouin zone. As the band structure is symmetric around $k_0=0$, it will be investigated only for $0 \leq k_0 \leq g/2$ in the following. To calculate the band structure powerful tools are available, which are not discussed here. For our calculations the program *MIT Photonic-Bands* has been used (for information on MIT Photonic-Bands see [Johnson01]). The full set of solutions includes a discrete set of modes, which can be localized inside the guides (waveguide modes) or inside the cladding (cladding modes). However, if the cladding is sufficiently thick, the bands of the cladding modes move closer together and can be approximated by a continuum of modes, as it appears for a bulk material of the same refractive index as the cladding. Furthermore we have to distinguish between modes with a main component of the electric field which is x -polarized and those, with a y -polarized main component.

An example of a band structure for mainly x -polarized modes is given in Fig. 2, where the first three waveguide bands and the continuum of the cladding modes are shown. We found that for our structures the bands of the corresponding y -polarized modes look very similar and are almost indistinguishable from the bands of the mainly x -polarized modes, if plotted together in the same diagram.

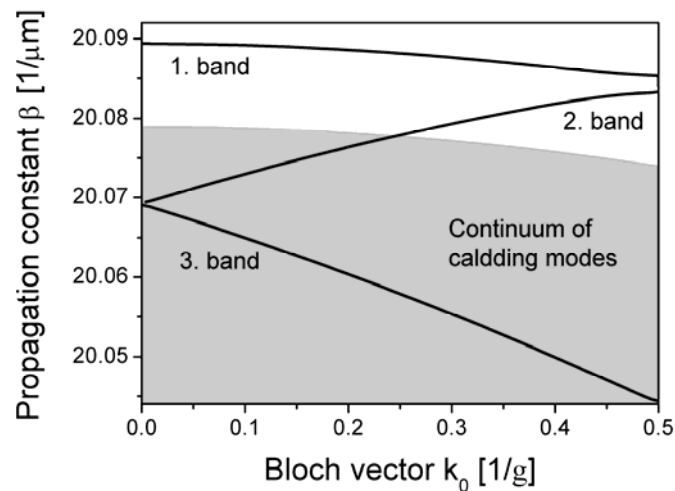


Fig. 2 Band structure of a waveguide array as depicted in Fig. 1. The refractive index for the substrate is $n_s=1.4570$, for the waveguide $n_{co}=1.5615$ and for the cladding $n_{cl}=1.5595$ at a wavelength of $\lambda=488\text{nm}$. Already the second band dips into the continuum of cladding modes.

The band structure determines the propagation of light inside the corresponding waveguide array. The first derivative $\delta\beta_n/\delta k_0$ describes the effective propagation direction of light inside the respective band n for each value of k_0 . Light inside the first band travels straight along the waveguides at the extrema $k_0=0$ and $k_0=g/2$ and has a maximum transverse slope at the inflection point in between. The second derivative $\delta^2\beta/\delta k_0^2$ and thus the curvature gives information about the diffraction properties. Positive $\delta^2\beta/\delta k_0^2$ correspond to anormal diffraction and negative $\delta^2\beta/\delta k_0^2$ to normal diffraction. Light in the first band experiences normal diffraction in the centre of the Brillouin zone (e.g. $k_0=0$) and anormal diffraction at its edges.

The modal fields of the three waveguide bands for the Bloch vector $k_0=0$ are depicted in Fig. 3 inside one unit cell of the corresponding structure (see Fig. 1).

The mode of the first band is centred inside the unit cell. Due to the weak guiding in x -direction only a weak modulation of the field appears in x . In contrast to this, maxima of the mode of the second band are centred in the low index region and a minimum appears inside the waveguide. While the modal fields in the first two bands are symmetric in x with respect to the centre of the waveguides, the modal field of the third band is anti-symmetric with respect to the to the waveguides centre.

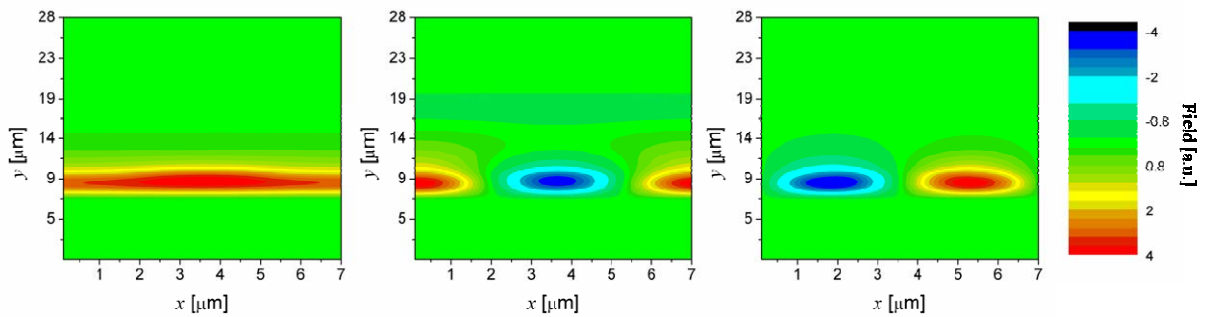


Fig. 3 Modal fields of the first three waveguide bands for the Bloch vector $k_0=0$.

The eigenvalue problem for two dimensional waveguide arrays with rectangular symmetry can be derived analogous to the one-dimensional case. The y -dependence of the dielectric function is then periodic as well. Thus it has to be developed into a Fourier-series too and the single summation in eq. (13) has to be replaced by a double summation. As a result the Bloch theorem is expanded into both transverse directions. An example of a two-dimensional square lattice and the corresponding band structure is given in chapter 5.

3. Defects and interfaces in waveguide arrays

The subject of this chapter is the investigation of local defects and interfaces in otherwise homogeneous waveguide arrays. The propagation of light in homogeneous waveguide arrays has been demonstrated to deviate considerably from the propagation in bulk materials [Somekh73, Pertsch02]. Experimental observations of discrete diffraction and refraction have been performed in polymer waveguide arrays. A natural arising question is how the propagation of light in such arrays is influenced by local defects or interfaces. Defects can be created by locally changing the width of the waveguides or their spacing. Interfaces can be introduced by an abrupt change of these quantities.

Here the formation of localized states at defects consisting of a single waveguide is calculated based on a coupled mode theory. Defects are shown to be either attractive or repulsive. The results are verified in experiments in polymer waveguide arrays. Furthermore theoretical investigations on an electro-optical switch in a LiNbO_3 -array are presented as an example for an application of the defect modes. In the last part of this chapter, the existence of bound states at interfaces is analyzed and the transmission and reflection coefficients for Bloch waves are calculated

3.1. Coupled mode theory

As all investigations in this chapter are based on one-dimensional waveguide arrays consisting of weakly coupled single-mode waveguides, a *coupled mode theory* [Börner90] or *tight binding approximation* can be used for the theoretical analysis. Then the field evolution inside the array

is described by the superposition of the evolution of the modal fields of the single waveguides, while the interaction between the waveguides is included by the coupling between the evanescent tails of the modal fields. In the theoretical model the influence of neighbouring waveguides on each waveguide is described by a weak perturbation. The field evolution along the n -th waveguide is given by

$$\begin{aligned}\hat{\mathbf{E}}_n(\mathbf{r}, t) &= \text{Re}\{a_n(z, \omega)\mathbf{e}_n(x, y, \omega)e^{-i\omega t}\}, \\ \hat{\mathbf{H}}_n(\mathbf{r}, t) &= \text{Re}\{b_n(z, \omega)\mathbf{h}_n(x, y, \omega)e^{-i\omega t}\},\end{aligned}\quad (16)$$

with the mode structures $\mathbf{e}_n(x, y, \omega)$ and $\mathbf{h}_n(x, y, \omega)$ and the z -dependent amplitudes $a_n(z, \omega)$ and $b_n(z, \omega)$. Without any perturbation the amplitudes evolve harmonically in z $a_n(z, \omega) = a_n^+(0, \omega)\exp[i\beta_n(\omega)z] + a_n^-(0, \omega)\exp[-i\beta_n(\omega)z]$ with the propagation constant $\beta_n(\omega)$ and the amplitudes of the forward and backward propagating waves a_n^+ and a_n^- . To simplify following equations we normalize the modal fields $\mathbf{e}_n(x, y, \omega)$ and $\mathbf{h}_n(x, y, \omega)$

$$\frac{1}{2}\text{Re}\left\{\int_{-\infty}^{+\infty}\int_{-\infty}^{+\infty}[\mathbf{e}_n(x, y, \omega)\times\mathbf{h}_n^*(x, y, \omega)]\mathbf{u}_z dx dy\right\} = P_0. \quad (17)$$

P_0 is the normalization power for all modes and \mathbf{u}_z the unit vector in z -direction. \mathbf{h}_n^* denotes the complex conjugate of \mathbf{h}_n .

In the following we want to derive the dynamics of the fields, which is determined by coupling between adjacent waveguides. Therefore we describe the evolution of the amplitudes by a perturbation theory and derive a coupled mode description via the well known reciprocity theorem. Because we assume monochromatic fields the frequency ω is omitted in the arguments and all considerations are performed in frequency space.

The field vectors for each waveguide have to obey Maxwell's equations, where we now introduce a perturbation polarization $\mathbf{\Pi}_n(\mathbf{r})$:

$$\begin{aligned}\text{(a)} \quad \nabla\times\mathbf{E}_n(\mathbf{r}) - i\omega\mu_0\mathbf{H}_n(\mathbf{r}) &= 0, & \text{(c)} \quad \nabla\times\mathbf{H}_n(\mathbf{r}) + i\omega\varepsilon_0\varepsilon_n(\mathbf{r})\mathbf{E}_n(\mathbf{r}) &= -i\omega\mathbf{\Pi}_n(\mathbf{r}), \\ \text{(b)} \quad \nabla\cdot\varepsilon_n(\mathbf{r})\mathbf{E}_n(\mathbf{r}) &= 0, & \text{(d)} \quad \nabla\cdot\mathbf{H}_n(\mathbf{r}) &= 0.\end{aligned}\quad (18)$$

$\varepsilon_n(\mathbf{r})$ contains the refractive index distribution of the considered waveguide. As we investigate isotropic materials, it is a scalar. We assume, that in the unperturbed waveguide $\mathbf{\Pi}_n(\mathbf{r})=0$ only a forward propagating wave $\mathbf{E}_{n,u}(\mathbf{r})=\mathbf{e}_n(x, y)\exp(i\beta_n z)$ is excited. The field of the perturbed waveguide can be written as $\mathbf{E}_{n,p}(\mathbf{r})=a_n(z)\mathbf{e}_n(x, y)$ for $\mathbf{\Pi}_n(\mathbf{r})=\mathbf{P}_n(\mathbf{r})$. The perturbation should be weak, so that the original shape of the modes of the waveguides is preserved. Then the evolution of the field during the propagation can be described by a z -dependent amplitude

$a_n(z)$. The fields of the unperturbed as well as of the perturbed system have to fulfil the corresponding Maxwell's equations (18). We multiply $\mathbf{H}_{n,u}^*$ with eq. (18) (a) and $\mathbf{E}_{n,p}$ with the conjugate complex of eq. (18) (b). Then we subtract the latter one from the first and obtain

$$\nabla \cdot [\mathbf{E}_{n,p} \times \mathbf{H}_{n,u}^*] = i\omega\mu_0 \mathbf{H}_{n,p}^* \mathbf{H}_{n,u} - i\omega\varepsilon_0\varepsilon_n \mathbf{E}_{n,p} \mathbf{E}_{n,u}^*, \quad (19)$$

where $*$ indicates the complex conjugate. For simplicity reasons the arguments are not written here. In the same way we proceed with $\mathbf{E}_{n,u}^*$ and eq. (18) (b) and $\mathbf{H}_{n,p}$ and [eq. (18) (a)] $*$. We subtract the result from eq. (19) and obtain

$$\nabla \cdot [\mathbf{E}_{n,p} \times \mathbf{H}_{n,u}^* + \mathbf{E}_{n,u}^* \times \mathbf{H}_{n,p}] = i\omega \mathbf{E}_{n,u}^* \mathbf{P}_n. \quad (20)$$

Next we integrate this equation over the entire transverse plane (x and y)

$$\int_{-\infty}^{+\infty} \int_{-\infty}^{+\infty} \left\{ \frac{\partial}{\partial z} [\mathbf{E}_{n,p} \times \mathbf{H}_{n,u}^* + \mathbf{E}_{n,u}^* \times \mathbf{H}_{n,p}] \right\}_z dx dy = i\omega \int_{-\infty}^{+\infty} \int_{-\infty}^{+\infty} \mathbf{E}_{n,u}^* \mathbf{P}_n dx dy. \quad (21)$$

Only the z -component of the divergence and thus the transverse components of the field vectors contribute to the left part of this equation.

If we examine two modes of the same waveguide instead of the unperturbed and perturbed fields, the orthogonality relation follows from eq. (21)

$$\int_{-\infty}^{+\infty} \int_{-\infty}^{+\infty} [\mathbf{e}_{n,1}(x, y, \omega) \times \mathbf{h}_{n,2}^*(x, y, \omega)]_z dx dy = 0, \quad (22)$$

which states, that without a perturbation no coupling takes place between modes of the same waveguide, e.g. between the fundamental modes of different polarization.

We insert our ansatz for the fields of the unperturbed and perturbed system in eq. (21). Furthermore we consider only forward propagating waves $a_n = a_n^+$, since we assume P_n does not efficiently couple modes of different propagation directions. As we deal with arrays, which are homogeneous in propagation direction, this is always fulfilled. Then we obtain for the n -th waveguide

$$\left[\frac{\partial}{\partial z} - i\beta_n \right] a_n(z) = \frac{i\omega}{4P_0} \int_{-\infty}^{+\infty} \int_{-\infty}^{+\infty} \mathbf{e}_n^*(x, y) \mathbf{P}_n(\mathbf{r}) dx dy. \quad (23)$$

Since in this work linear systems are investigated, only linear contributions to the polarization are considered. Then the polarization can be split up into two parts $\mathbf{P}_n(\mathbf{r}) = \mathbf{P}_{n,l}(\mathbf{r}) + \mathbf{P}_{n,c}(\mathbf{r})$. $\mathbf{P}_{n,l}(\mathbf{r})$ is the polarisation due to 'local perturbations' caused by deviations of the dielectric function of the waveguide $\Delta\varepsilon_n(x, y)$ from the original solution assumed for the unperturbed waveguide. $\mathbf{P}_{n,c}(\mathbf{r})$ contains the influence of coupling to other waveguides. The first contributions to the polarisation $\mathbf{P}_{n,l}(\mathbf{r})$ reads as

$$\mathbf{P}_{n,l}(\mathbf{r}) = \varepsilon_0 \Delta \varepsilon_n(x, y) \mathbf{e}_n(x, y) a_n(z). \quad (24)$$

Inserting eq. (24) in eq. (23), we obtain an equation for a disturbed single waveguide

$$\left[i \frac{\partial}{\partial z} + \beta_n + \alpha_n \right] a_n(z) = 0, \quad (25)$$

with α_n being the detuning coefficient

$$\alpha_n = \frac{\omega}{4P_0} \varepsilon_0 \int_{-\infty}^{+\infty} \int_{-\infty}^{+\infty} \Delta \varepsilon_n(x, y) \mathbf{e}_n^*(x, y) \mathbf{e}_n(x, y) dx dy. \quad (26)$$

Consequently, a change of the considered waveguide itself, e.g. in the shape of the cross section or the refractive index, leads to an additional contribution to the propagation constant of the mode of the perturbed waveguide.

Next we have a look at the coupling between different guides. Since we investigate arrays, each waveguide is surrounded by two other waveguides, one to its left and one to its right. The interaction takes place by energy exchange via the overlap of the evanescent tails of the modes of the different guides.

We complete our mathematical model of the polarization by describing its second part $\mathbf{P}_{n,c}(\mathbf{r})$, which contains the influence of all other waveguides on the field in the waveguide under consideration. The contribution of the additional waveguides to the polarization read as

$$\mathbf{P}_{n,c}(x, y) = \varepsilon_0 \sum_{n'=1}^N \Delta \varepsilon_n(x, y) a_{n'}(z) \mathbf{e}_{n'}(x, y). \quad (27)$$

$\Delta \varepsilon_n(x, y)$ is the deviation of the dielectric function from the unperturbed system for the n -th waveguide. $a_{n'}(z)$ and $\mathbf{e}_{n'}(x, y)$ are the amplitude and modal field of the n' -th waveguide. Inserting eq. (27) in eq. (23) we obtain a differential equation for the modal amplitude of the n -th waveguide

$$\left[i \frac{\partial}{\partial z} + \beta_n + \tilde{\alpha}_n \right] a_n(z) + \sum_{\substack{n'=1 \\ n' \neq n}}^N c_{n,n'} a_{n'}(z) = 0. \quad (28)$$

$c_{n,n'}$ is the coupling coefficient for the waveguides n and n' and is given by

$$c_{n,n'} = \frac{\varepsilon_0 \omega}{4P_0} \int_{-\infty}^{+\infty} \int_{-\infty}^{+\infty} \Delta \varepsilon_n(x, y) \mathbf{e}_n^*(x, y) \mathbf{e}_{n'}(x, y) dx dy. \quad (29)$$

The term $n'=n$ gives an additional contribution to the propagation constant

$$\tilde{\alpha}_n = \frac{\varepsilon_0 \omega}{4P_0} \int_{-\infty}^{+\infty} \int_{-\infty}^{+\infty} \Delta \varepsilon_n(x, y) \mathbf{e}_n^*(x, y) \mathbf{e}_n(x, y) dx dy. \quad (30)$$

This small correction is combined to one variable with the propagation constant β_n to $\tilde{\beta}_n$. Furthermore we assume in the following only the coupling coefficients between adjacent waveguides to supply substantial contributions and thus all others can be neglected. Then the resulting coupled mode equations become

$$\left[i \frac{\partial}{\partial z} + \tilde{\beta}_n + \alpha_n \right] a_n(z) + c_{n,n-1} a_{n-1}(z) + c_{n,n+1} a_{n+1}(z) = 0. \quad (31)$$

These equations describe the evolution of the modal amplitude $a_n(z)$ of the n -th waveguide in a one-dimensional linear waveguide array, where nearest neighbour interaction is assumed only.

3.2. Homogeneous waveguide arrays

Before discussing inhomogeneous waveguide arrays, fundamental effects in homogeneous arrays are introduced in this section [Pertsch02]. For homogeneous arrays all coupling and propagation constants have the same value $c_n = c_a$ and $\tilde{\beta}_n = \beta_0$. Then eq. (31) reads as

$$\left(i \frac{\partial}{\partial z} + \beta_0 \right) a_n + c_a (a_{n-1} + a_{n+1}) = 0. \quad (32)$$

Eigensolutions of this equation are plane waves or Bloch modes of the form

$$a_n = a e^{i\beta z + i\kappa n}, \quad (33)$$

where κ is the normalized Bloch vector or the phase difference between adjacent guides corresponding to a tilt of the beam. In comparison to the Bloch waves introduced in the last chapter (cp. eq. (15)), for a coupled mode theory the continuous periodical contribution $\Psi(x, y) = \Psi(x + d, y)$ is replaced by a constant amplitude a . The normalized Bloch vector κ is obtained from the Bloch vector k by normalization to $1/d$, with d being the lattice period.

Inserting this ansatz into eq. (32) we find β to be entirely defined by κ giving the so-called diffraction relation or band structure (Fig. 4)

$$\beta = \beta_0 + 2c_a \cos(\kappa). \quad (34)$$

In contrast to bulk media the range of propagation constants β of freely propagating waves is limited. Its width depends on the coupling constant c_a and its position is defined by the wave number of the individual guides β_0 . While the exact solution of the eigenvalue problem (see 2.2) provides also higher order bands, they are neglected in this approximation and do not appear as a solution of the coupled mode equations, where we obtain only a single band. Outside this band only waves exist, which decay exponentially in transverse direction. As a

consequence of the coupled mode approximation the shape of the diffraction relation for the band is sinusoidal.

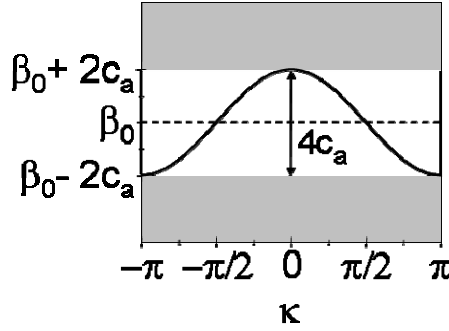


Fig. 4. Diffraction relation (band structure) of Bloch waves in a homogeneous waveguide array.

The propagation inside a homogeneous array can be calculated analytically [Jones65, Yellin95]. To this end the propagation is described in Fourier space using the discrete Fourier transform

$$\tilde{a}(\kappa, z) = \frac{1}{2\pi} \sum_n a_n(z) e^{-i\kappa n}, \quad a_n(z) = \int_{-\pi}^{+\pi} \tilde{a}(\kappa, z) e^{i\kappa n} d\kappa, \quad (35)$$

which relates the modal amplitudes to the amplitudes of discrete plane waves. The evolution of an arbitrary excitation $\tilde{a}(\kappa, z = 0)$ in Fourier space is described by $\tilde{a}(\kappa, z) = \tilde{a}(\kappa, z = 0) \exp[i\beta(\kappa)z]$, where $\beta(\kappa)$ is given by the diffraction relation (34). Transforming the amplitudes at a propagation distance z back into the spatial domain, we obtain the general solution of the diffracted field $a_n(z)$ for an arbitrary initial distribution $a_n(0)$

$$a_n(z) = \sum_{m=-\infty}^{\infty} G_{n,m}(z) a_m(0) e^{i\beta_0 z} \quad \text{with} \quad G_{n,m} = i^{n-m} J_{n-m}(2c_a z), \quad (36)$$

with $G_{n,m}$ being the Green's function of an array and J_{n-m} the Bessel function of the first kind. The propagation inside an array is depicted in Fig. 5. The picture on the left hand side shows the discrete diffraction pattern, as it appears if a single waveguide of the array is excited. In contrast to diffraction in a bulk medium the two main intensity maxima are located at the edges of the diffraction pattern instead of the centre. However, this changes as the excitation becomes broader. If several guides are excited by a Gaussian-like beam, also the envelope of the diffraction pattern is Gaussian, as is appears in a homogeneous medium too (see Fig. 5).

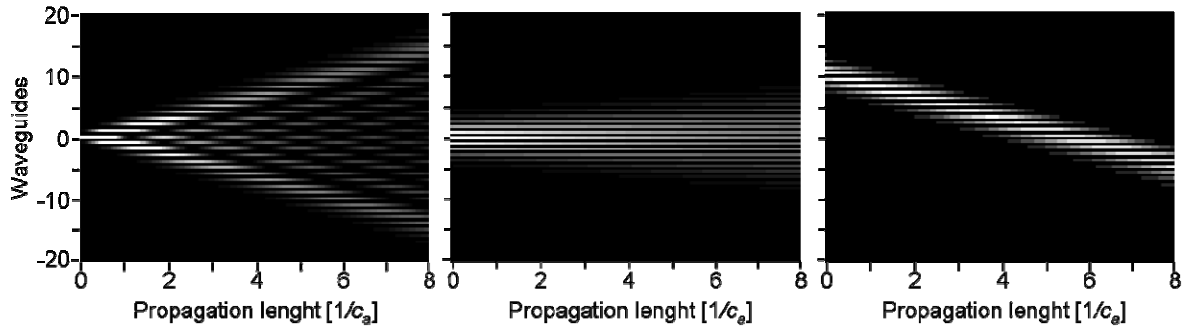


Fig. 5 Diffraction for excitation of a single waveguide (left) and with a broad beam (centre) and propagation without diffraction at $\kappa=\pi/2$ (right).

The reason for this dependence on the width of the excitation can be explained with help of the band structure. A small excitation corresponds in Fourier space to a broad distribution. Thus all components with all possible transverse wave vectors κ exist, most of them propagating with high transverse velocities as indicated by the position of the intensity maxima. In contrast to that, at broad excitation only κ close to the centre of the Brillouin zone corresponding to small transverse velocities are excited.

Another interesting case is the propagation of a broad beam with a transverse wave number of $\kappa=\pi/2$, where the beam propagates almost without diffraction (see Fig. 5 right). As it can be seen from the band structure, the curvature of the diffraction relation is zero for this κ and thus up to second order no diffraction occurs.

3.3. Localized states at defect waveguides

The aim of this section is to investigate theoretically and experimentally basic features of defect modes in waveguide arrays. Areas of existence for different types of modes are predicted and experimentally confirmed.

3.3.1 Theory

The existence of bound states at a single defect waveguide in an otherwise homogeneous waveguide array is investigated. Only symmetric defects are considered, where the propagation constant and the coupling constant of the guide change. This can be achieved by varying the width of the corresponding guide or its spacing to neighbouring guides (see Fig. 6).

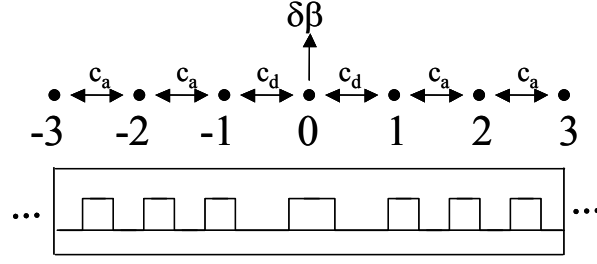


Fig. 6. Schematic representation of a waveguide array with a defect consisting of a single guide with changed width and spacing to its neighbours.

The propagation in such an array with a defect at $n=0$ is described by the following set of coupled mode equations:

$$\begin{aligned}
 n = 0: & \quad \left(i \frac{\partial}{\partial z} + \beta_0 + \delta\beta \right) a_0 + c_d (a_{-1} + a_1) = 0, \\
 n = \pm 1: & \quad \left(i \frac{\partial}{\partial z} + \beta_0 \right) a_{\pm 1} + c_d a_0 + c_a a_{\pm 2} = 0, \\
 |n| \geq 2: & \quad \left(i \frac{\partial}{\partial z} + \beta_0 \right) a_n + c_a (a_{n-1} + a_{n+1}) = 0.
 \end{aligned} \tag{37}$$

c_d is the modified coupling constant for the defect and $\delta\beta$ is the change of the propagation constant of the defect. Any mode bound to a defect must have the form

$$a_n(z) = A_n \exp(i\beta_d z) \tag{38}$$

with constant amplitudes A_n . To determine whether the defect can indeed carry a guided mode we have to perform some mathematics. Because exponentially decaying tails are required, the field shapes are described by

$$A_{\pm|n|} = A_{\pm 1} \gamma^{|n|-1} \quad \text{for } |n| \geq 2, \tag{39}$$

where

$$|\gamma| < 1 \tag{40}$$

holds. Inserting the ansatz (38) and (39) into eq. (37) we immediately obtain the propagation constant of guided modes as a continuation of the diffraction relation (34) as

$$\beta_d = \beta_0 + c_a \left(\gamma + \frac{1}{\gamma} \right). \tag{41}$$

Because we restrict ourselves to symmetric defects respective guided modes must be either symmetric or antisymmetric. For an antisymmetric mode ($A_{+1} = -A_{-1}$) the field amplitude at guide $n=0$ must vanish ($A_0=0$) for symmetry reasons. Hence all changes induced by the defect

in eq. (37) have no effect and the defect itself becomes invisible for antisymmetric modes. Consequently no field is bound and no guided mode with odd symmetry exists. Therefore only symmetric modes have to be considered. Assuming $A_{+1} = A_{-1}$ and inserting eqs. (38), (39) and (41) into eq. (37) we end up with an eigenvalue problem for the transverse decay rate of the field structure γ as

$$\frac{1}{\gamma} = \frac{\delta\beta}{2c_a} \pm \sqrt{\left(\frac{\delta\beta}{2c_a}\right)^2 + 2\left(\frac{c_d}{c_a}\right)^2 - 1}. \quad (42)$$

If $(c_d/c_a)^2 > 1 - \delta\beta/(2c_a)$ holds; γ is positive and fulfils inequality (40), i.e., $0 < \gamma < 1$. The respective guided mode is called “unstaggered” because it possesses a flat phase (see Fig. 7 (a)). Following eq. (41) its propagation constant lies above the band of Bloch states of the homogenous array. However, γ can also be negative if the condition $(c_d/c_a)^2 > 1 + \delta\beta/(2c_a)$ is fulfilled giving rise to the formation of a staggered mode with a phase difference π between adjacent waveguides (see Fig. 7 (b)). In contrast to guided modes in conventional materials the wave number of the respective guided mode is below those of the continuous states in the homogenous array.

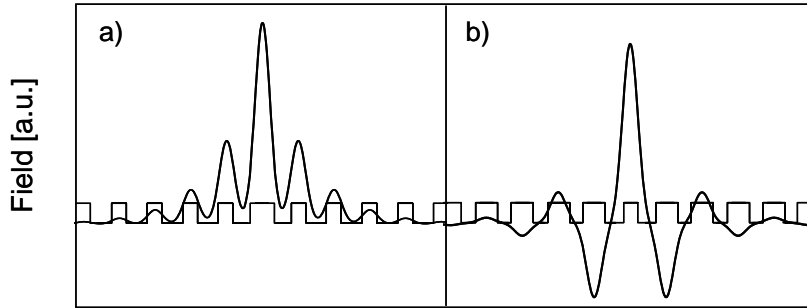


Fig. 7. Field of (a) an unstaggered and (b) a staggered mode at a defect guide.

In the parameter space defined by c_d/c_a and $\delta\beta/c_a$ we can find areas without guided modes, with single mode waveguiding, either a staggered or an unstaggered mode, or domains with both types of modes coexisting (see Fig. 8).

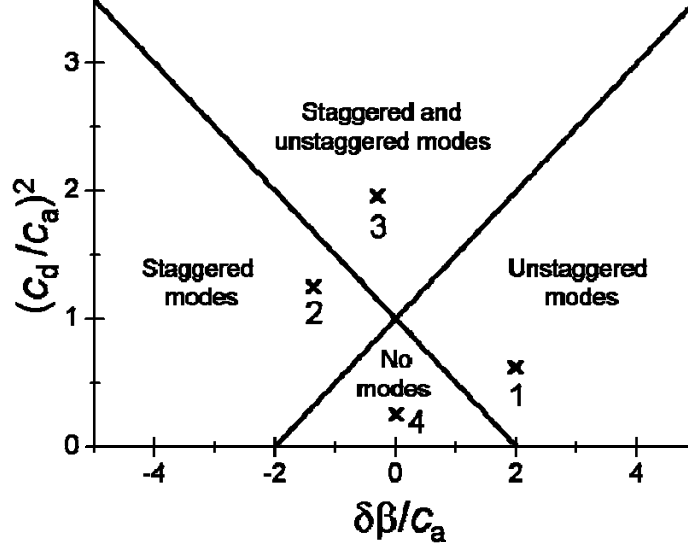


Fig. 8. Regions of existence for symmetric staggered and unstaggered modes in the $(c_d/c_a)^2$ - $\delta\beta/c_a$ -plane.

To a certain extent waveguiding in conventional materials is reproduced. For instance we find an unstaggered mode, if only the refractive index of the defect guide is increased compared to the homogeneous array: $\delta\beta > 0$. However, contrary to waveguiding in homogeneous media a localized state also appears in form of a staggered mode, if the wave number of the central guide is decreased: $\delta\beta < 0$.

To understand the peculiarities of waveguide arrays it is useful to assume that the defect itself forms its own tiny array with an individual band structure extending between the boundaries $\beta_0 + \delta\beta \pm 2c_d$ (see Fig. 9). As soon as this “defect band” extends further than that of the homogeneous array, a localized state can be formed. The respective wave number β_d must be contained in the “defect band” but missed in the band of the homogeneous array.

This simple picture also explains that if the coupling around the defect is increased $c_d > c_a$ we find both staggered and unstaggered modes to appear (see Fig. 9 (c)) on both sides of the band of the homogeneous array. In contrast to that, no guidance is observed for a decreased coupling $c_d < c_a$. In this case all wave numbers of the defect band are phase matched to waves of the homogenous array (see Fig. 9 (d)).

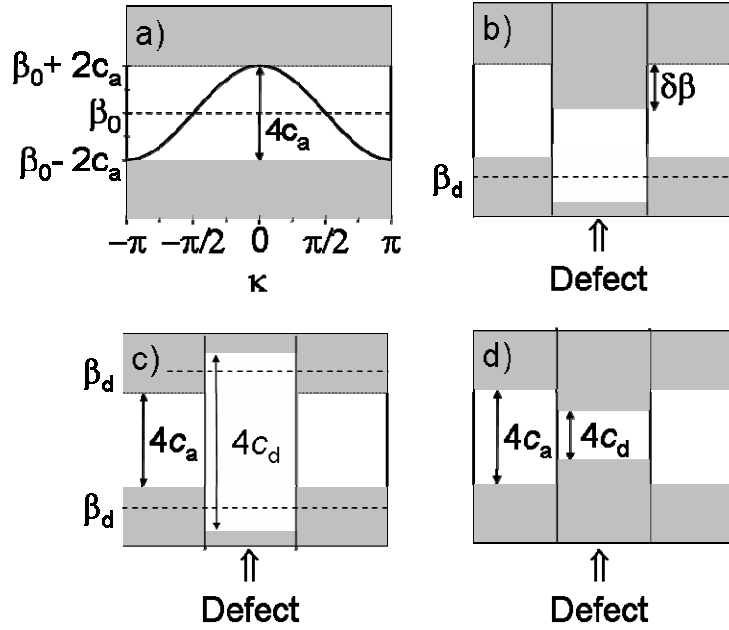


Fig. 9. Diffraction relation of Bloch modes and the formation of defect modes. (a) Diffraction relation of Bloch-waves (longitudinal vs. transverse wave number) in a homogeneous waveguide array (propagation constant of unperturbed waveguide: β_0 , coupling constant c_a). In the shaded regions only evanescent waves exist. (b) Shift of the band structure and formation of a staggered mode (wave number β_d) around a defect with a wave number reduced by $\delta\beta$. (c) Expansion of the band structure and formation of staggered and unstaggered modes around a defect with increased coupling ($c_d > c_a$) (d) Compression of the band structure around a defect with reduced coupling ($c_d < c_a$).

While this simple picture provides a very intuitive description for the existence of defect modes, it cannot give quantitative information. In particular, the picture fails for simultaneous variation of wave number $\delta\beta$ and coupling c_d of the defect. The main reason is the lack of a continuous density of states in the “defect array”. If the number of waveguides in the “defect array” would be infinitely large the above mentioned method to determine guided defect modes would become exact.

3.3.2 Experiment

We are now going to compare the theoretical predictions with experimental results. To this end waveguide arrays consisting of 101 waveguides were fabricated of an inorganic-organic hybrid polymer [Houbertz03] ($n_{co}=1.547 @ 633\text{nm}$) on thermally oxidized silicon wafers ($n_{sub}=1.457 @$

633nm) with a polymer cladding ($n_{cl}=1.544 @ 633\text{nm}$) (see Fig. 10). The samples were fabricated by UV lithography [Streppel02] on 4 inch wafers leading to propagation lengths up to 7cm. All waveguides have the same height of $3.5\mu\text{m}$. Waveguide widths between 2.5 and $4.5\mu\text{m}$ provide low loss single mode wave-guiding ($<0.04\text{dB/cm @ 633 nm}$) and a waveguide spacing between 4 and $5\mu\text{m}$ ensures an efficient evanescent coupling of the nearest neighbouring guides.

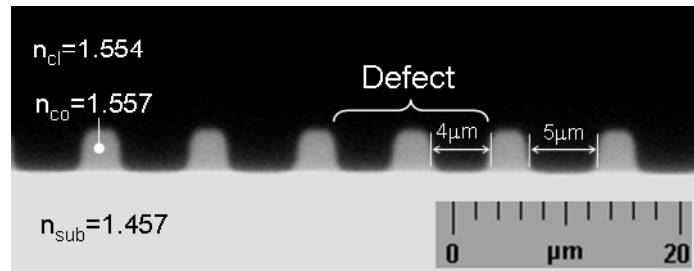


Fig. 10 Cross section of a polymer waveguide array with a defect. The defect is introduced by reducing the waveguide spacing compared with the homogenous array.

Keeping in mind that the properties of a mode guided by the defect depend solely on the two parameters $\delta\beta/c_a$ and c_d/c_a we fabricated samples to test defects belonging to the four distinct areas in the parameter plane (see Fig. 8). To introduce defect guides we varied width and spacing of the corresponding waveguide. Where a modification of the waveguide spacing solely influences the coupling between the neighbouring waveguides, a variation of the width of a guide does not only change the wave number of the defect but alters the coupling as well. Compared to the deliberately induced perturbations conventional fabrication tolerances are much smaller and originate almost exclusively from a variation of the waveguide layer thickness due to the spin coating process. The spatial scale of resulting inhomogeneities is comparable with the width of the wafer. Hence, our structures are mainly subject to a constant drift of parameters. Comparing samples originating from different parts of the wafer we found the strength of the coupling to change by approximately 5%. Within one sample no transverse variations of the array parameters could be observed.

A single waveguide excitation was implemented by focusing a HeNe laser beam on the entrance facet with a microscope objective. The light emitted from the end faced was detected by a CCD-camera.

First we checked the existence of an unstaggered mode by creating a single guide with increased width of $3.5\mu\text{m}$ compared with $3\mu\text{m}$ in the homogeneous part of the array. As a

consequence the propagation constant of the defect guide is increased ($\delta\beta/c_a=2$). But additionally the coupling is slightly decreased $c_d/c_a=0.8$ (see cross 1 in Fig. 8). Similar to conventional waveguiding light concentrates around the region of higher effective index and the modal fields have a flat phase (see Fig. 11 (a)).

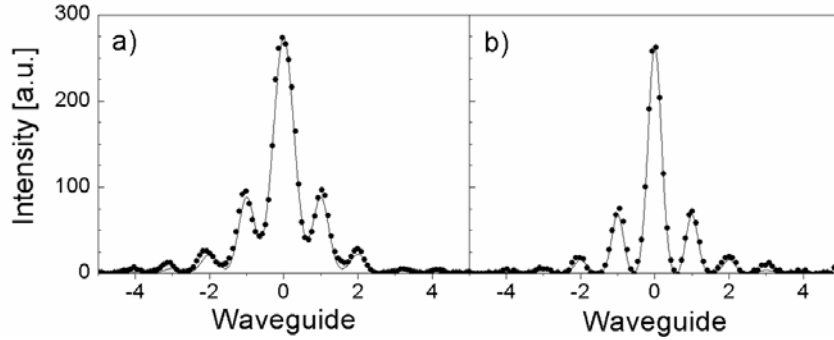


Fig. 11. Intensity of an unstaggered and a staggered mode for a dominant change of the propagation constant of the defect. (a) Field distribution of an unstaggered defect mode for $\delta\beta/c_a=2.0$ and $c_d/c_a=0.8$ (cross 1 in Fig. 8), solid line: theory, dots: experiment. (b) Field distribution of a staggered defect mode for $\delta\beta/c_a=-1.4$ and $c_d/c_a=1.1$ (cross 2 in fig. 4), solid line: theory, dots: experiment.

Next we investigated deviations from classical waveguiding mechanisms. Hence we looked for a staggered mode by decreasing the width of the defect waveguide ($3\mu\text{m}$ compared with $3.5\mu\text{m}$ in the remaining array). Again the resulting decrease of the propagation constant of the defect ($\delta\beta/c_a=-1.4$) is accompanied by a small increase of the coupling constant ($c_d/c_a=1.1$, see cross 2 in Fig. 8). In fact we also observed a guided mode (see Fig. 11 (b)), whose shape differs considerably from that of an unstaggered one. Because fields in adjacent guides are π out of phase, the intensity of a staggered mode becomes zero between the waveguides due to destructive interference of respective modal fields. Hence, in contrast to the unstaggered mode, which is bound by total internal reflection, the guiding mechanism of the staggered state relies on Bragg reflection on the periodic structure of the array.

In case of a dominant change of the coupling constant c_d , two different regions occur in the $\delta\beta/c_a-(c_d/c_a)^2$ -plane. For an increase of the defect coupling $c_d > c_a$ both, unstaggered and staggered modes exist. A nearly exclusive increase of the coupling constant c_d was experimentally achieved by decreasing the spacing between the centre waveguide and its neighbours (spacing: $4\mu\text{m}$ compared with $5\mu\text{m}$ in the rest of the array). The corresponding parameters are $c_d/c_a=1.4$ and $\delta\beta/c_a=-0.3$ (see cross 3 in Fig. 8). An input beam centred on a

single waveguide always excites both modes. At the end facet of the array an interference pattern is observed depending on the actual phase difference between the two bound states. Since both modes have different propagation constants their phase relation changes on propagation. More important, already the initial phase difference depends on the point of excitation. If the exciting beam is shifted from the defect guide ($n=0$) towards its neighbour ($n=\pm 1$) the phase difference between the staggered and unstaggered modes changes by π . Hence, by varying the waveguide of excitation we can switch between destructive and constructive interference in e.g. the defect guide at the output facet (compare Fig. 12).

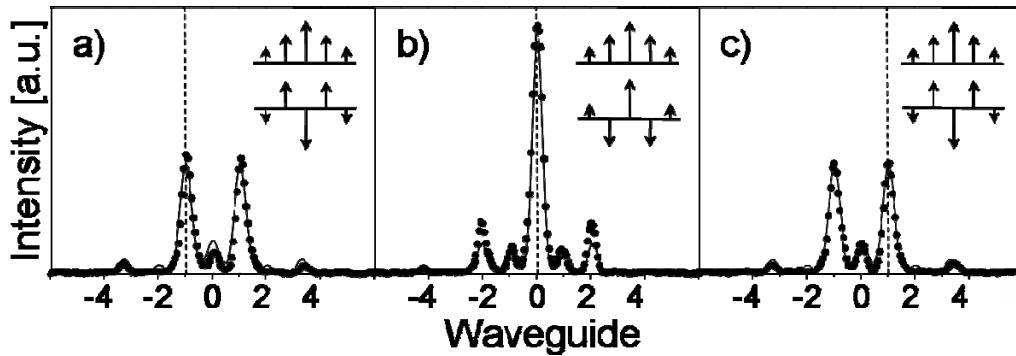


Fig. 12. Interference pattern of a staggered and an unstaggered defect mode for dominant change of the coupling constant ($\delta\beta/c_a = -0.3$ and $c_d/c_a = 1.4$, cross 3 in Fig. 8) of the defect at a propagation distance of 59,95mm. Dots: experiment, lines: theory, dashed line: position of the excitation. (b) Intensity distribution for an excitation of the defect waveguide. (a) and (c) Intensity distribution for an excitation of the left and right nearest neighbour waveguide of the defect. Insets: schematic diagrams of the modal amplitude of the unstaggered and staggered mode, the superposition of both modal fields produces the actual interference pattern.

Because the phase of the staggered mode alternates whereas that of the unstaggered one remains flat a constructive interference of both modes on the defect site is accompanied by destructive interference in the neighbouring site and vice versa. Hence we either observe a maximum in guide $n=0$ or $n=\pm 1$. Even if the initial excitation is asymmetric with respect to the defect guide we never observe an asymmetric guided field at the output. Hence, as predicted no asymmetric mode exists, although the defect is multimode.

The analytical theory predicts that there are no bound states if the coupling constant of the defect waveguide is decreased ($c_d < c_a$ - cross 4 in Fig. 8). This is somehow contra intuitive. Because the defect tends to be isolated due to the reduced coupling one would even expect

improved guiding properties. Again the simplified model of the local band around the defect helps to explain the effect (see Fig. 9 (d)). A decrease of the coupling constant results in a band shrinkage. Hence all states of the defect band are phase matched to those of the homogenous array. Light from the defect predominantly couples into Bloch modes of the middle of the band, which have a high transverse velocity. Hence, the excitation will leave a defect with reduced coupling very quickly as demonstrated in the experiment (see Fig. 13 (a) and (b)). In contrast to an excitation in the homogenous array, where parts of the field also propagate straight (see Fig. 13 (c) and (d)), the defect repels the light causing a dark region around it.

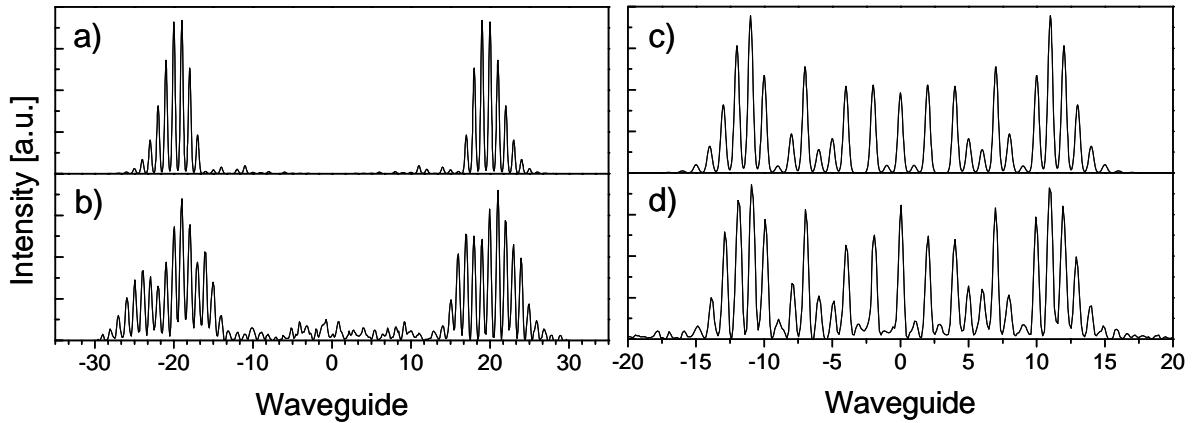


Fig. 13 Diffraction pattern for an excitation of a repulsive defect ((a) theory, (b) experiment) with reduced coupling ($c_d/c_a=0.5$, $\delta\beta/c_a=0$, cross 4 in Fig. 8) and in a homogeneous array ((c) theory, (d) experiment).

3.3.3 Bound states at the edges of waveguide arrays

Besides the bound states at the induced defects, we often found localized states at the edges of the arrays. They appear when the outermost waveguide or its neighbour is excited. An example of a measured intensity distribution is given in Fig. 14. Clearly a localized state bound to mainly three waveguides exists. Moving the excitation between the two outermost guides we found the intensity distribution varying, which indicates the existence of more than one localized state.

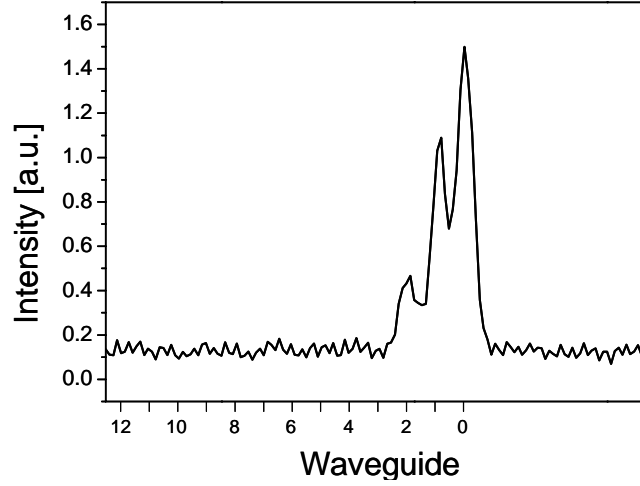


Fig. 14 Measured intensity profile of a bound state at the right edge of a waveguide array.

To understand the origin of these modes we again perform some analytics. We investigate the simple case that only the outermost waveguide and the coupling constant to its neighbour vary from the homogeneous array. The coupled mode equations for this problem are

$$\begin{aligned}
 n = 0: & \quad \left(i \frac{\partial}{\partial z} + \beta_0 + \delta\beta \right) a_0 + c_d a_1 = 0, \\
 n = 1: & \quad \left(i \frac{\partial}{\partial z} + \beta_0 \right) a_1 + c_d a_0 + c_a a_2 = 0, \\
 n > 1: & \quad \left(i \frac{\partial}{\partial z} + \beta_0 \right) a_n + c_a (a_{n-1} + a_{n+1}) = 0,
 \end{aligned} \tag{43}$$

with $n=0$ being the index of the outermost waveguide. Analogous to section 3.3.1 we calculate bound states $a_n(z) = A_n \exp(i\beta_d z)$ with $A_n = \gamma A_{n-1}$ for $n > 1$ with $|\gamma| > 1$. We find that an unstaggered state exists if $(c_d/c_a)^2 < 1 - \delta\beta/c_a$. Additionally a staggered mode appears for $(c_d/c_a)^2 < 1 - \delta\beta/c_a$, which makes the defect multimode. Consequently, modes can exist already if only one waveguide is different from the homogeneous array, but no modes exist at the edge of a completely homogeneous array. From this result we can follow that in our case some variation of the waveguides close to the edges of the array must exist. If a localized state exists for one perturbed waveguide also for more than one perturbed guide localized states can exist.

To find out what happen at the edges our arrays we examined them under a microscope. As expected the guides at the edges are strongly deformed (see Fig. 15), but the situation is much more complicated than assumed in our simple analytical model.

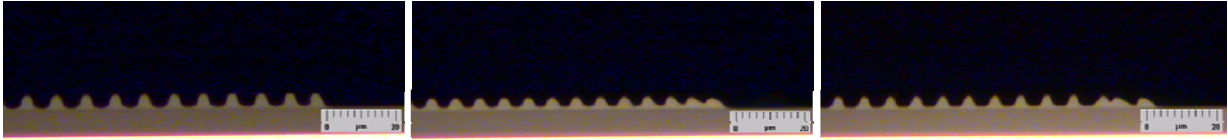


Fig. 15 Strongly deformed waveguides at the edges of the waveguide arrays.

The spacing between the two or three outermost waveguides becomes effectively reduced as the waveguides are tilted towards each other. Additionally due to a strong deformation of the guides a large change of the propagation constant has to be expected. Even if for this complex structure no analytical description is possible, it is quite sure that the strong deformation causes the observed localized states.

3.4. LiNbO₂ optical switch

In the previous section basic features of a single defect were investigated. The aim of this section is to evaluate possibilities for an application of defects for optical switching. To this end an electro-optical controllable defect in a waveguide array is theoretically investigated as an example. Therefore, a homogeneous waveguide array of titanium in-diffused waveguides in lithium niobate (Ti:LiNbO₃) is assumed. A defect is electro-optically induced by electrodes on top of the array. For the following calculations an array consisting of 81 waveguides in a z-cut LiNbO₃-substrate is considered. To take into account the influence of electrodes with an applied voltage onto the array, BPM-simulations are performed. The creation of a symmetric single defect as investigated in the last section is not possible in this configuration. To produce a change in the refractive index the electric field has to be oriented vertical to the surface, as only in this case the largest electro optic coefficient r_{33} is used. This leads to a structure where at minimum two waveguides are influenced by the electro-optic effect. Fig. 16 shows an example of the structures that are under investigation in this work.

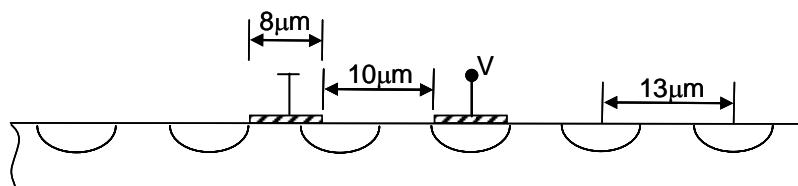


Fig. 16 Schematic representation of cross section of electro-optical controlled defect.

Two different possibilities for switching or signal processing are investigated. The first one is based on bound states or defect modes while the second one is based on the reflection of a tilted beam. However, the aim of this work is not to present a true device but to perform a proof of principle.

3.4.1 Analytical investigations

Before designing a device in this section more general analytical examinations are made, which give basic information about the investigated structure. The existence of bound states and the reflection and transmission coefficients are estimated by using a coupled mode theory. For the analytical calculations we assume only two waveguides to be perturbed by the field of the electrodes. Furthermore the coupling constant is assumed to be fixed, which is only an approximation. The perturbations for the two waveguides can be different, as it is the case for the structure shown in Fig. 16. Then the coupled mode equations read as

$$\begin{aligned}
n = 0: & \quad \left(i \frac{\partial}{\partial z} + \beta_0 + \delta\beta_0\right)a_0 + c_a (a_1 + a_{-1}) = 0, \\
n = 1: & \quad \left(i \frac{\partial}{\partial z} + \beta_0 + \delta\beta_1\right)a_1 + c_a (a_0 + a_2) = 0, \\
\text{else:} & \quad \left(i \frac{\partial}{\partial z} + \beta_0\right)a_n + c_a (a_{n-1} + a_{n+1}) = 0,
\end{aligned} \tag{44}$$

with the perturbations $\delta\beta_0$ and $\delta\beta_1$.

A) Bound states

For bound states the z -dependence of the amplitudes is described by

$$a_n = A_n e^{i\beta_a z}, \tag{45}$$

with constant amplitudes A_n . To the left and right of the defect guide the amplitude has to decay exponentially, what can be described by the ansatz

$$\begin{aligned}
n > 1: & \quad A_n = \gamma A_{n-1}, \\
n < 0: & \quad A_n = \gamma A_{n+1},
\end{aligned} \tag{46}$$

with $|\gamma| < 1$. Inserting eqs.(45) and (46) into the coupled mode equations (44) we obtain

$$\frac{1}{\gamma} = \frac{\delta\beta_0 + \delta\beta_1}{2c_a} \pm \sqrt{\left(\frac{\delta\beta_0 + \delta\beta_1}{2c_a}\right)^2 - \frac{\delta\beta_0 \delta\beta_1}{c_a^2} + 1}. \tag{47}$$

From the condition $|\gamma| < 1$ a relation between $\delta\beta_0/c_a$ and $\delta\beta_1/c_a$ can be calculated, which is visualized in Fig. 17. For all different areas of the $\delta\beta_0/c_a - \delta\beta_1/c_a$ -plane an example of the solutions for the parameter marked by the crosses is depicted.

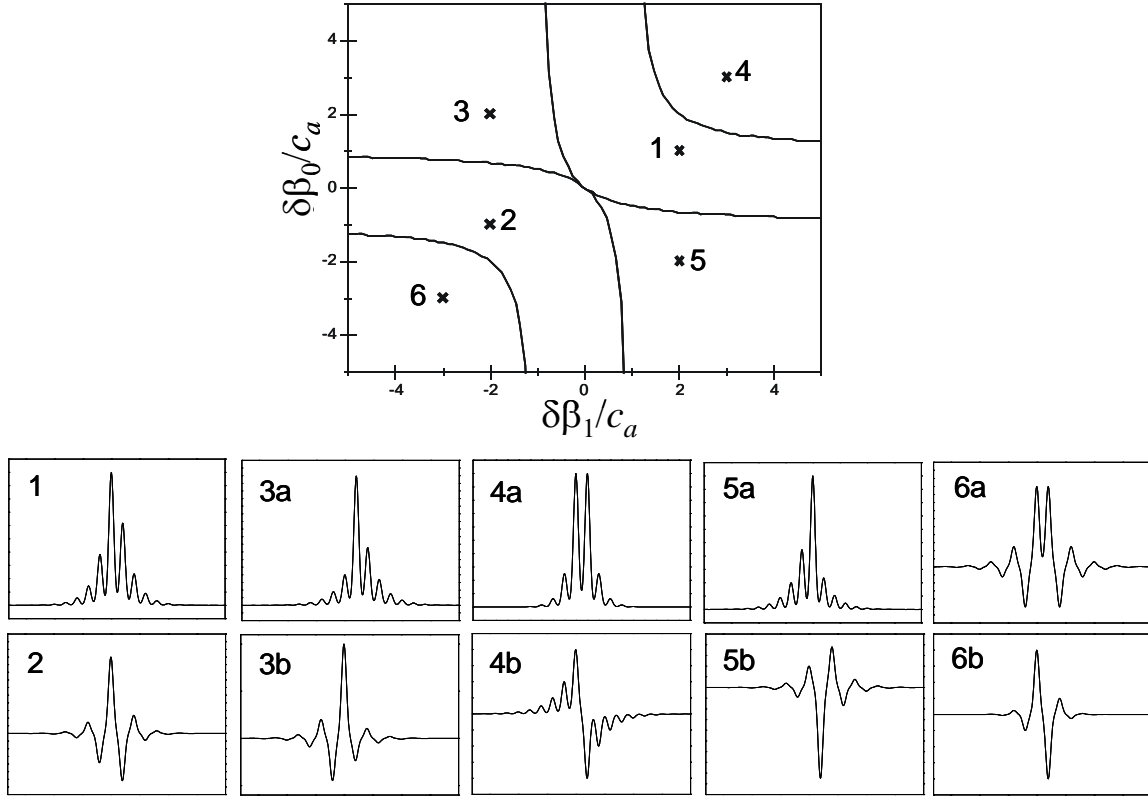


Fig. 17. Top: Regions of existence for different types of modes in the $\delta\beta_0/c_a - \delta\beta_1/c_a$ -plane. Crosses mark parameter for examples. Bottom: Modes corresponding to parameters marked in the parameter plane.

We distinguish between different modes by means of their symmetry properties. For points 4 and 6 in the parameter plane the defect is symmetric, as the perturbations $\delta\beta_0$ and $\delta\beta_1$ have the same value. In this case we classify the modes as unstaggered (4a), staggered (6b), twisted unstaggered (4b) and twisted staggered (6a) [Darmanyán98]. If the defect itself is asymmetric, also the modes become asymmetric. However, we can still distinguish unstaggered asymmetric (1, 3a and 5a) and staggered asymmetric modes (2, 3b and 5b). Only in those areas of the parameter plane, where points 1 and 2 are located, the defect is single mode; otherwise always two modes exist.

B) Reflection and transmission

The coefficients for the reflection and transmission of Bloch waves at the defect are calculated.

For this purpose we make an ansatz

$$\begin{aligned}
 n < 0: & \quad \bar{a}_n = e^{ikn} + \rho e^{-ikn}, \\
 n = 0: & \quad \bar{a}_0, \\
 n = 1: & \quad \bar{a}_1, \\
 n > 1: & \quad \bar{a}_n = \tau e^{ikn},
 \end{aligned} \tag{48}$$

with $a_n = \bar{a}_n e^{i\beta z}$, τ being the transmission coefficient and ρ the reflection coefficient for the corresponding Bloch wave. β has to fulfil the dispersion relation $\beta = \beta_0 + 2c_a \cos \kappa$. Eq. (48) is inserted into the coupled mode equations (44). From the result, the transmission can be calculated as

$$\tau = \frac{(1 - e^{-2i\kappa}) e^{-2i\kappa}}{-b_3 \{b_0 [b_1 b_3 - 1] - b_3\} + [b_1 b_3 - 1]}, \tag{49}$$

$$\text{with } b_0 = (\beta - \beta_0 - \delta\beta_0) / c_a, b_1 = (\beta - \beta_0 - \delta\beta_1) / c_a, b_3 = (\beta - \beta_0) / c_a - e^{i\kappa}$$

and the reflection as

$$\rho = -e^{-2i\kappa} + \tau e^{i\kappa} \{b_0 [b_1 - 1] - k\}. \tag{50}$$

Fig. 18 shows the reflection in dependence of the transverse wave number κ of a defect for different values of the perturbations $\delta\beta_0$ and $\delta\beta_1$.

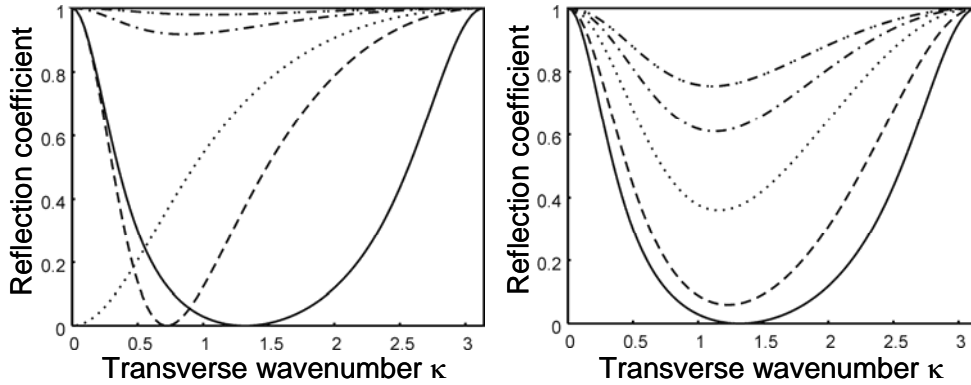


Fig. 18. Reflection coefficient of Bloch waves at a defect consisting of two perturbed waveguides. (a) Symmetric defect $\delta\beta_1 = \delta\beta_2 = \delta\beta$ with parameters $\delta\beta = 0.5$ (solid), 1.5 (dashed), 2 (dots), 3 (dash dot) and 4 (dash dot dot). (b) Asymmetric defect with $\delta\beta_0 = 0.5$ and $\delta\beta_1 = 0.5$ (solid), 1 (dashed), 2 (dots), 3 (dash dot) and 4 (dash dot dot).

In Fig. 18 (a) symmetric defects $\delta\beta_0=\delta\beta_1$ are considered. For weak perturbation the reflection approaches zero for one specific value of κ . The value of this κ becomes smaller for stronger perturbation until it vanishes for $(\beta_0+\delta\beta_0)/c_a=2$. Fig. 18 (b) displays the reflection for different asymmetric defects. Here mainly the minimum of the reflection changes, as it grows with an increasing perturbation.

3.4.2 BPM-simulations

Having made some simple analytical investigation in the last section, now examples for a device which makes use of the discussed effects are given. To model the propagation inside the array with a defect under realistic conditions numerical simulations (beam propagation method - BPM) are used. To derive the basic equation for a BPM we introduce two approximations into the wave equation (7), which are the scalar and the paraxial approximation. We assume an x -polarized electric field and propagation in z -direction. For small refractive index variations we can approximate the electric field as $\mathbf{E}(\mathbf{r}) \approx \mathbf{u}_x u(x, y, z) \exp(i\beta z)$ with a slowly varying amplitude $u(x, y, z)$ and a fast oscillating phase term. Because $|\partial u / \partial z| \ll |\beta|$, second z -derivatives of $u(x, y, z)$ can be neglected. Furthermore we neglect derivatives of the refractive index distribution, because $|\nabla \varepsilon(x, y)| \ll |\varepsilon(x, y)|$. The dielectric function is expressed in terms of the refractive index $\varepsilon(x, y) = n^2 + 2n\Delta n(x, y)$, where the average refractive index n is defined by $\beta = n\omega/c$. $\Delta n(x, y)$ includes deviations from the average refractive index n . Then we obtain the so-called scalar wave equation, which reads as

$$\left[2i\beta \frac{\partial}{\partial z} + \frac{\partial^2}{\partial x^2} + \frac{\partial^2}{\partial y^2} + 2\Delta n(x, y) \frac{\omega}{c} \beta \right] u(x, y, z) = 0. \quad (51)$$

This simplified equation is the basis for the BPM simulations, where it is solved numerically [Roey81].

The diffusion profile of the waveguides as well as the influence of the electrodes is included in the simulations. The investigated setup has a geometry as shown in Fig. 16 with one strongly and one weakly perturbed guide. The advantage of this structure is, that it is possible to create single mode defects.

The parameters for the fabrication process are assumed for the BPM simulations as follows: thickness of Ti-layer $0.98\mu\text{m}$, width of Ti-strips $7.0\mu\text{m}$, vertical diffusion depth $5.78\mu\text{m}$, horizontal diffusion depth $4.5\mu\text{m}$. All waveguide arrays were designed for a wavelength of $1.55\mu\text{m}$ and transverse magnetic (TM) polarization. Furthermore, we used typical process

parameter, as they can be found in [Strake88, Crank75, Hocker77]. The calculation of the electric field of the electrodes is based on [Jin91]. Values for the electro-optic coefficients are taken from the literature [Karth91].

Two different excitations are investigated for the same array, the excitation of the defect guide itself and the excitation inside the homogeneous part of the arrays with a broad tilted beam. While in the first configuration the array can be used as an on-off-switch in the second configuration it can be used as a branch with a controllable ratio of the power in the two outputs. As for both investigations exactly the same technical parameters are used, in case of an experimental verification the same sample could be used for the investigation of the bound state and the reflection. For the single waveguide excitation light is coupled into the guide underneath one of the electrodes. If no voltage is applied the light diffracts (see Fig. 19 (a)) and only a small part remains in the excited guide. If a voltage is applied a defect guide is formed and the light establishes a bound state (see Fig. 19 (b)).

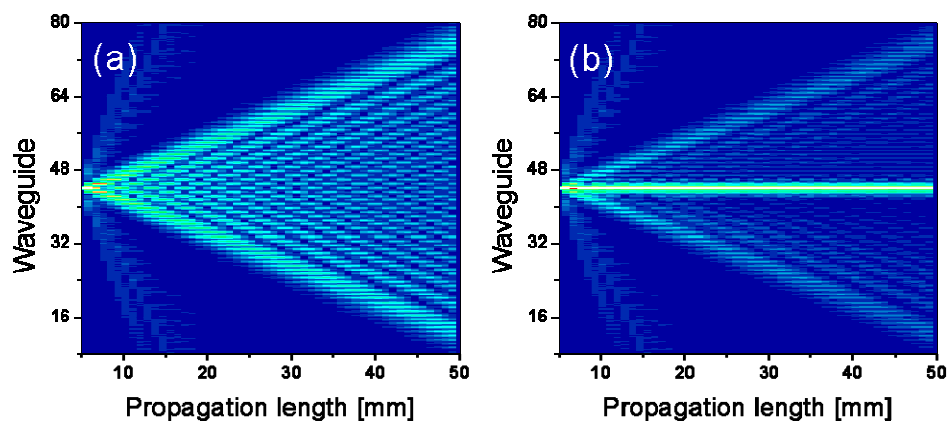


Fig. 19 Simulation of propagation inside the waveguide array with a controllable defect. (a) Voltage 0V, discrete diffraction. (b) 30V, localized state.

The transmission of the defect guide in dependence of the voltage is displayed in Fig. 20. Effectively an on-off switch is formed, with the output being the defect guide.

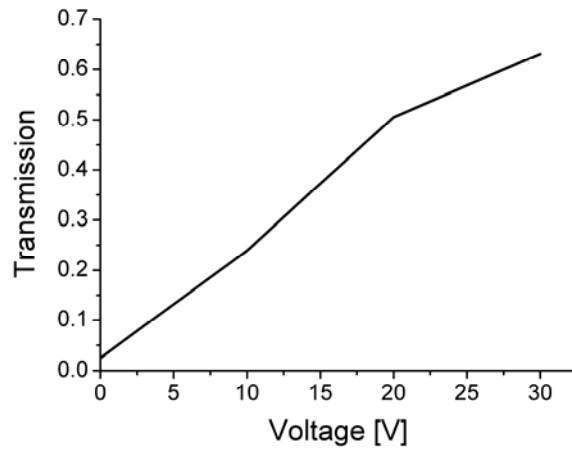


Fig. 20. Transmission of a switch based on a controllable defect in dependence of the applied voltage.

For another investigation the excitation of several waveguides with a tilted broad beam is assumed. While the investigations of the first demonstrated system are focused on an on-off-switch, this system acts as a controllable Y-branch, where the ratio of the two output beams can be changed by the applied voltage.

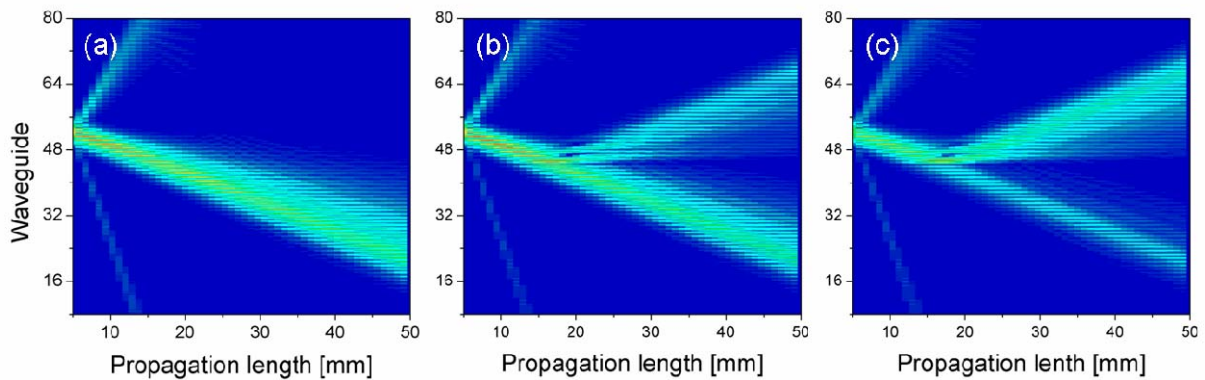


Fig. 21 Propagation of a broad beam with a transverse wavenumber of $\pi/2$ and its reflection and transmission at a defect for (a) 0V, (b) 20V and (c) 30V.

For this system the angle of the incident beam is chosen so, that the beam propagates at the angle that provides the lowest diffraction, which is the case if the phase difference between adjacent guides is $\pi/2$. In the investigated system the excitation is located $120\mu\text{m}$ away from the defect at an angle of 0.737° . While the beam propagates, it hits the defect and is partly reflected and transmitted (see Fig. 21). Thereby the strength of reflection can be controlled by the applied voltage. For complete reflection an even stronger defect would be necessary. The maximal voltage is limited by the breakdown voltage in air, which is already reached at 30V.

The results are resumed in Fig. 22 in form of a curve for the transmission and reflection in dependence of the voltage.

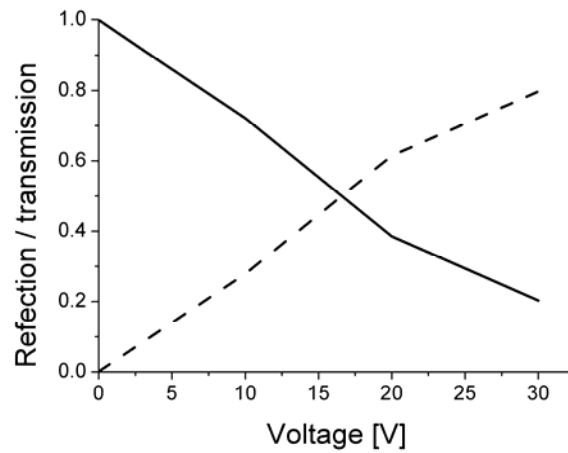


Fig. 22. Transmission (solid line) and reflection (dashed line) of a broad beam at an electro-optically controllable defect in dependence of the applied voltage.

Even if no complete reflection into the second output is possible, the system still provides the possibility to change the ratio between the intensity of the two outputs in a range between 20 and 80% for both outputs.

3.5. Interfaces in waveguide arrays

In this section the propagation of light waves in waveguide arrays with an abrupt change of the parameters of the array is theoretically analyzed. In the following we will refer to these abrupt changes as interfaces. Analogue to the previous sections the analytical investigations are based on a coupled mode theory. Then an interface can be described by a change of the coupling constant and the effective index, as it is schematically depicted in Fig. 23.

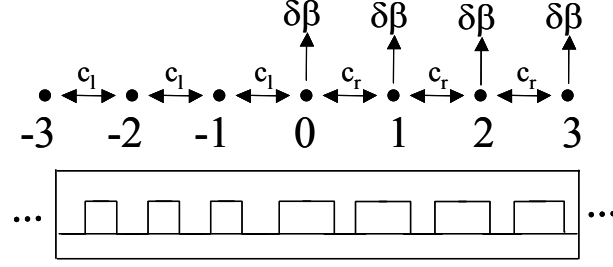


Fig. 23 Schematic representation of an interface in a waveguide array, which is induced by a change of the coupling constant and the effective index of the guides.

The coupled mode equations for this problem read as

$$\begin{aligned}
 n < 0: & \quad \left(i \frac{\partial}{\partial z} + \beta_0 \right) a_n + c_l (a_{n-1} + a_{n+1}) = 0, \\
 n = 0: & \quad \left(i \frac{\partial}{\partial z} + \beta_0 + \delta\beta \right) a_0 + c_l a_{-1} + c_r a_1 = 0, \\
 n > 0: & \quad \left(i \frac{\partial}{\partial z} + \beta_0 + \delta\beta \right) a_n + c_r (a_{n-1} + a_{n+1}) = 0.
 \end{aligned} \tag{52}$$

c_l and c_r are the coupling constants to the left and right of the interface. $\delta\beta$ is the change in the propagation constant for the waveguides of the right hand side of the array.

3.5.1 Bound states at interfaces

Analogue to the calculations on defect modes in section 3.3, we will now investigate if localized states can be found also at interfaces. If these modes exist, they must have the form

$$a_n = A_n e^{\beta_i z} \tag{53}$$

and decay exponentially to the right and left of the interface. Because the right and left part of the array have now different parameters, also the decay factors must be different for the right and left tail. We make the ansatz

$$\begin{aligned}
 A_n &= \gamma_r A_{n-1} \quad \text{for } n \geq 1 \quad \text{and} \\
 A_n &= \gamma_l A_{n+1} \quad \text{for } n \leq 1,
 \end{aligned} \tag{54}$$

where

$$|\gamma_l| < 1 \quad \text{and} \quad |\gamma_r| < 1 \tag{55}$$

must hold. Inserting eq. (54) into the coupled mode equations (52) we obtain for the propagation constant of the interface mode

$$\beta_i = \beta_0 + c_l \left(\gamma_l + \frac{1}{\gamma_l} \right). \quad (56)$$

γ_l and γ_r can be calculated in dependence on the parameters of the array as

$$\gamma_r = \delta\beta \frac{c_r}{c_l^2 - c_r^2} \quad \text{and} \quad \gamma_l = \frac{1}{\delta\beta} \frac{c_l^2 - c_r^2}{c_l}. \quad (57)$$

To determine, if localized states at interfaces exist, we have to find out if these equations can be fulfilled simultaneously with the condition (55). Indeed this is the case for

$$\left| 1 - \left(\frac{c_r}{c_l} \right)^2 \right| < \left| \frac{\delta\beta}{c_l} \right| < \left| \frac{1 - (c_r/c_l)^2}{(c_r/c_l)^2} \right|. \quad (58)$$

We draw the solution of this condition for the normalized parameters c_r/c_l and $\delta\beta/c_l$ (see Fig. 24). Modes can exist for $c_r/c_l < 1$ only and the interface is always single mode. Depending on the sign of $\delta\beta$ the bound state can be either staggered or unstaggered.

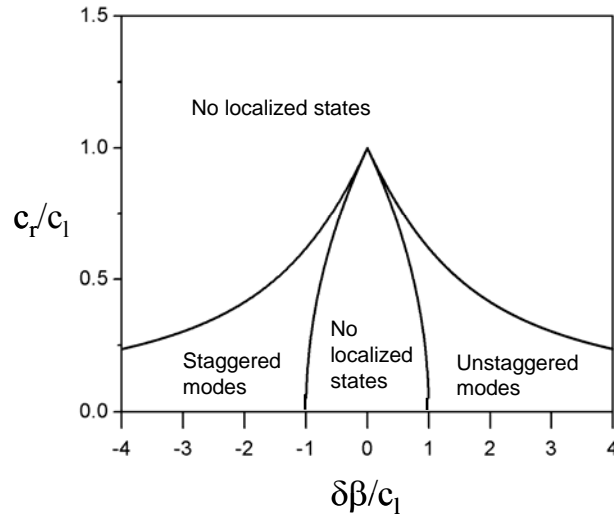


Fig. 24 Areas of existence for staggered or unstaggered localized states at interfaces.

As one expects the propagation constant of the unstaggered and staggered mode lie above and below the bands of the two parts of the array, respectively. Fig. 25 shows examples for an unstaggered and a staggered mode.

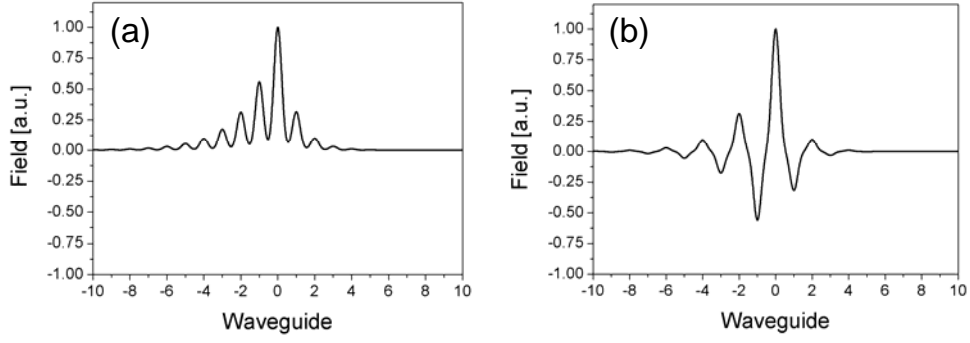


Fig. 25 Fields of the modes for an interface with parameters (a) $\delta\beta/c_l=1.5$ and $c_r/c_l=0.4$ for the unstaggered mode and (b) $\delta\beta/c_l=-1.5$ and $c_r/c_l=0.4$ for the staggered mode.

The tails of the modes adopt the form of the Bloch modes, which lie closest towards them concerning their propagation constant. This determines the shape of the bound state, which has to be unstaggered, if it lies above the bands and staggered below. One would expect that the upper (lower) edges of the bands of both parts of the array have to lie close together in order to allow an unstaggered (staggered) mode to form. The upper (lower) edge of both bands match exactly along the straight line $c_r/c_l=1-\delta\beta/c_l$ ($c_r/c_l=1+\delta\beta/c_l$) and indeed, the existence area of the modes for positive (negative) $\delta\beta$ is located around this line. However, for large absolute values of $\delta\beta$ the existence area extends far away from these lines.

While this picture gives an idea where to search for bound states, it does not explain why they exist. To find the reason, we again use the simple picture of different bands belonging to the different parts of the array. For the left and right part we can determine the extension of the bands as $\beta_0-2c_l \leq \beta \leq \beta_0+2c_l$ and $\beta_0+\delta\beta-2c_r \leq \beta \leq \beta_0+\delta\beta+2c_r$, respectively. For the waveguide $n=0$ the coupling constants to the right and left neighbour have different values. If we imagine a complete array constructed of such guides, we obtain a double-periodic array with a band which extends between $\beta_0+\delta\beta-c_r-c_l$ and $\beta_0+\delta\beta+c_r+c_l$. As an approximation to our system we assign this band to the guide $n=0$. To obtain bound states this band has to include propagation constants β , which lie outside the bands of the homogeneous parts of the array. In the following we examine the case $\delta\beta>0$, which leads to an unstaggered mode. Compared to the band for $n<0$ the bands for $n=0$ and $n>0$ are shifted upwards by $\delta\beta$. Furthermore they shrink or expand depending on the value of c_r in comparison to c_l . Fig. 26 shows the bands of the three different regions of the array for one example with $\delta\beta=c_l$ and $c_r=0.5c_l$.

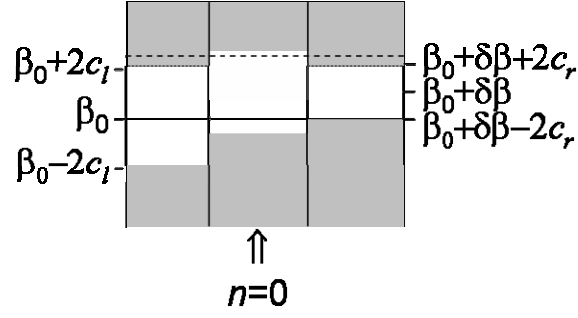


Fig. 26 Illustration of the origin of interface modes. Bands of the three different parts of the array depicted for $\delta\beta=c_l$ and $c_r=0.5c_l$. The dashed line marks the propagation constant β_i of the interface mode.

In this case a localized state can exist, because the band of the interface guide extends to higher values of β than the bands for the two other parts. The propagation constant of the bound state β_i has to be located in this region. From this simple picture follows immediately, that bound states can occur only for $c_l > c_r$. The discussion of the existence of staggered modes follows analogous for $\delta\beta < 0$.

However, while this simple approximation allows estimating the existence of bound states in an intuitive way, it cannot provide quantitative information about the existence area of the interface modes. In particular it fails to explain the upper limit for the existence of bound states.

3.5.2 Reflection and transmission at interfaces

In this section the reflection and transmission coefficients for Bloch waves at interfaces are calculated analytically. To this end we make the ansatz

$$\begin{aligned}
 n < 0: & \quad (e^{i\kappa_1 n} + \rho e^{-i\kappa_1 n})e^{i\beta z}, \\
 n = 0: & \quad A_0 e^{i\beta z}, \\
 n > 0: & \quad \tau e^{i\kappa_r z} e^{i\beta z},
 \end{aligned} \tag{59}$$

with the reflection coefficient ρ and the transmission coefficient τ . The propagation constant β has to be conserved when the Bloch wave passes the interface. However, the effective propagation direction and thus the Bloch vector changes from κ_1 to κ_r . Furthermore in both parts of the array the dispersion relation must be fulfilled

$$\begin{aligned}
 n < 0: & \quad \beta = \beta_0 + 2c_l \cos(\kappa_1), \\
 n > 0: & \quad \beta = \beta_0 + \delta\beta + 2c_r \cos(\kappa_r).
 \end{aligned} \tag{60}$$

From this equations the Bloch vector of the transmitted Bloch wave can be calculated as function of the Bloch vector of the incoming wave

$$\kappa_r = \arccos\left(\frac{2c_l \cos(\kappa_l) - \delta\beta}{2c_r}\right). \quad (61)$$

This new Bloch vector becomes complex valued if the argument of the arccos-function is outside the interval $[-1;1]$. This is the case, if the propagation constant of the incoming wave is not included in the band of the right part of the array. Then no Bloch wave with a propagation constant matched to the incoming wave exists behind the interface and the incoming wave is total reflected. The appearance of total reflection can be illustrated with help of the band structure. We depict the bands to the left and right of the interface analogue to section 3.3.1. As only waves with a positive value of the Bloch vector reach the interface, we depict the bands in the interval $[0;\pi]$. Two examples are shown in Fig. 27. In Fig. 27 (a) the band is shifted up behind the interface because a positive value for $\delta\beta$ is assumed. In this case, no propagation constant exists inside the right part of the array for Bloch waves from the bottom of the band of the left part. Therefore, such a wave would be completely reflected. An analogous situation occurs for a shrinking of the band due to a decrease of the coupling constant (see Fig. 27 (b)), where total reflection appears if the incoming wave travels at the top or bottom of the respective band.

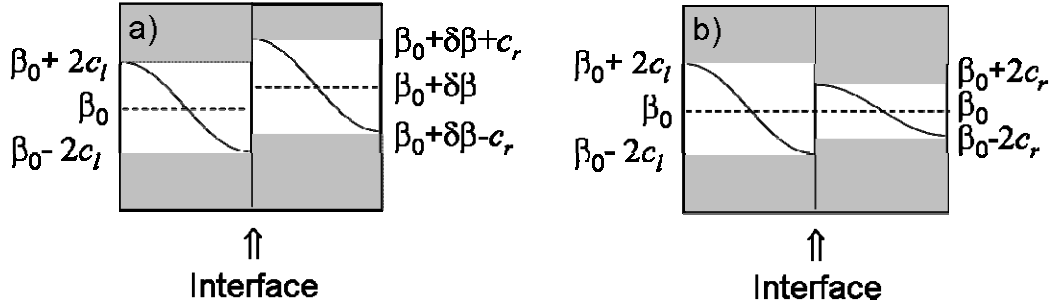


Fig. 27 Bands to the left and right of an interface for (a) $c_l = c_r$ and $\delta\beta > 0$, (b) $\delta\beta = 0$ and $c_r < c_l$.

To calculate the reflection coefficient, ansatz (59) is inserted into the coupled mode equations (52) and we obtain

$$\rho = -\frac{\left[-\beta \frac{c_l}{c_r} + \frac{\delta\beta}{c_r} + e^{i\kappa_r}\right] \left[\left(\beta - \frac{\delta\beta}{c_l}\right)(\beta - e^{-i\kappa_l}) - 1\right] + \frac{c_r}{c_l} [\beta - e^{-i\kappa_l}]}{\left[-\beta \frac{c_l}{c_r} + \frac{\delta\beta}{c_r} + e^{i\kappa_r}\right] \left[\left(\beta - \frac{\delta\beta}{c_l}\right)(\beta - e^{i\kappa_l}) - 1\right] + \frac{c_r}{c_l} [\beta - e^{i\kappa_l}]} e^{-2i\kappa_l}, \quad (62)$$

where β has to fulfil (60). From the reflection coefficient we determine the transmission coefficient

$$\tau = \frac{c_l}{c_r} e^{-i\kappa_r} \left\{ \left[\beta - \frac{\delta\beta}{c_l} \right] \left[\beta \left(e^{-i\kappa_l} + \rho e^{i\kappa_l} \right) - e^{-2i\kappa_l} - \rho e^{2i\kappa_l} \right] - e^{-i\kappa_l} - \rho e^{i\kappa_l} \right\}. \quad (63)$$

To analyze the results we calculate the coefficients for different parameters and depict the results for examples. Therefore we use parameters, which are normalized to c_l . This is useful as ρ and τ depend only on c_r/c_l and $\delta\beta/c_l$ and not on the absolute values of c_r and $\delta\beta$. Both, reflection and transmission coefficient are complex numbers. The incoming Bloch wave is split up into a reflected and transmitted part, which can experience a phase shift with respect to the incoming wave. Two examples for the coefficients in dependence of the Bloch vector of the incoming wave are depicted in Fig. 28. Concerning the appearance of total reflection, the results are in agreement with the explanation given to Fig. 27. It might be astonishing that the transmitted wave does not vanish in this case. However, this becomes clear keeping in mind that the transmitted wave can either be a Bloch wave or decay exponentially in case of an imaginary κ_r . As both cases are included, the transmission coefficient τ does not vanish even for total reflection $|\rho|=1$.

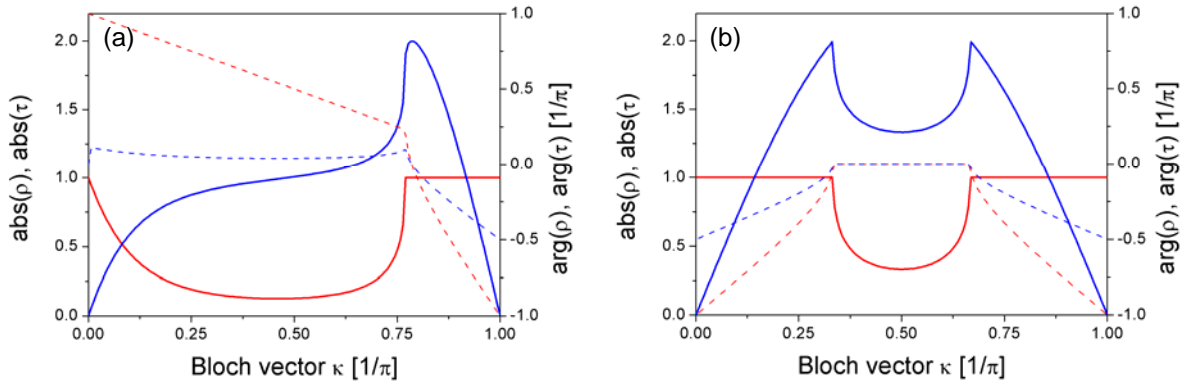


Fig. 28 Absolute value (solid) and argument (dashed) of the reflection (red) and transmission (blue) coefficients for (a) $\delta\beta=0.5c_l$ and $c_r=c_l$. and (b) $\delta\beta=0$ and $c_r=0.5c_l$.

To derive a quantity that represents the energy conservation, we examine the energy flow inside the array. To this end we start from a homogeneous array. The evolution of the energy inside a single guide is determined by the energy exchange between the respective guide and its neighbours

$$\frac{\partial}{\partial z} |A_n|^2 = ic_a \left[A_n^* (A_{n+1} + A_{n-1}) - A_n (A_{n+1}^* + A_{n-1}^*) \right], \quad (64)$$

with $a_n=A_n\exp(i\beta z)$. The energy inside a cluster of guides extending from $-N$ to N is given by

$$Q = \sum_{n=-N}^N |A_n|^2. \quad (65)$$

Energy can escape the cluster only via the two outermost waveguides. This is reflected in the corresponding equation

$$\frac{\partial}{\partial z} Q = ic_a \left[A_{-N}^* A_{-N-1} - A_{-N} A_{-N-1}^* + A_N^* A_{N+1} - A_N A_{N+1}^* \right], \quad (66)$$

where only the amplitudes of the outermost guides and their neighbours outside the cluster contribute.

To determine the energy flow we assume a cluster including all guides from $n=-\infty$ to $n=-1$. The energy change in this cluster, which corresponds to the left part of the array, is given by

$$\frac{\partial}{\partial z} Q_l = ic_a \left[A_0^* A_1 - A_0 A_1^* \right] = 2c_a \operatorname{Im} \left[A_0 A_1^* \right]. \quad (67)$$

Assuming a plane wave $A_n=A\cdot\exp(i\kappa n)$, this equation becomes

$$\frac{\partial}{\partial z} Q_l = \begin{cases} -2c_a |A|^2 \sin(\kappa) & \text{if } \kappa \text{ is real.} \\ 0 & \text{if } \kappa \text{ is imaginary.} \end{cases} \quad (68)$$

As expected no energy flow exists for evanescent waves (κ imaginary). To find a quantity, that represents the conservation of the energy, we analyse the energy flow of the incoming, transmitted and reflected waves. Assuming that the energy, transported by the reflected and transmitted wave, equals the energy of the incoming wave, the coefficients have to fulfil

$$c_l \sin(\kappa_l) = |\rho|^2 c_l \sin(\kappa_l) + |\tau|^2 c_r \sin(\kappa_r). \quad (69)$$

With eq. (61) we can derive from this equation

$$1 = |\rho|^2 + \frac{1}{\sin(\kappa_l)} \sqrt{\frac{c_r^2}{c_l^2} - \left(\cos(\kappa_l) - \frac{\delta\beta}{2c_l} \right)^2} |\tau|^2, \quad (70)$$

which represents the conservation of the energy inside the array. We introduce reflection and transmission coefficients for the energy

$$R = |\rho|^2 \quad \text{and} \quad T = \frac{1}{\sin(\kappa_l)} \sqrt{\frac{c_r^2}{c_l^2} - \left(\cos(\kappa_l) - \frac{\delta\beta}{2c_l} \right)^2} |\tau|^2 \quad (71)$$

and depict them in Fig. 29.

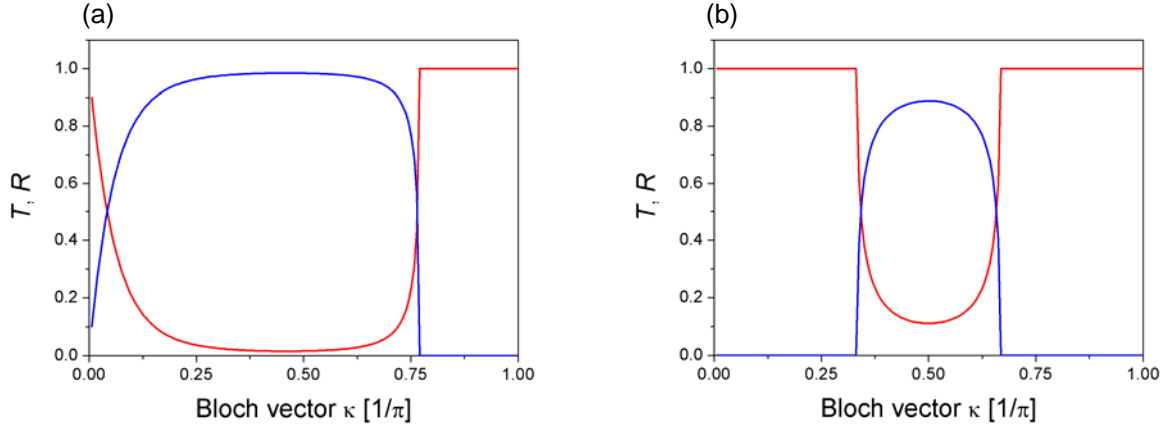


Fig. 29 Reflection R (red) and transmission T (blue) of energy at an interface inside a waveguide array for (a) $\delta\beta=0.5c_l$ and $c_r=c_l$ and (b) $\delta\beta=0$ and $c_r=0.5c_l$.

As expected, the transmission T grows with decreasing reflection R and vice versa. Their sum is constant, which reflects the conservation of the energy.

Next we investigate the propagation direction of the transmitted wave in dependence of the propagation direction of the incident wave. For each light wave the propagation direction is related to the first derivative of the band and thus to the normal on the band. Keeping in mind that the propagation constant β is conserved at the interface, one can examine the refraction properties comparing the bands of the left and right part of the array (see Fig. 30). This can lead to astonishing properties as illustrated in two examples in Fig. 31.

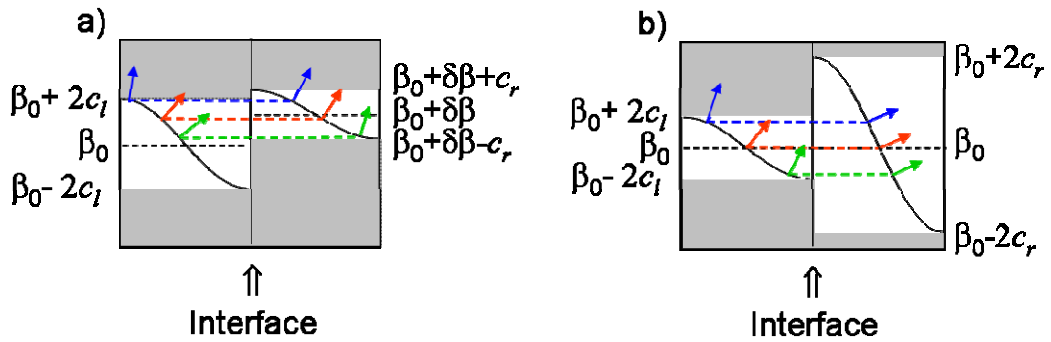


Fig. 31 Bands to the left and right of an interface for (a) $c_l > c_r$ and $\delta\beta > 0$, (b) $\delta\beta = 0$ and $c_l > c_r$. Arrows of the same colour illustrate the propagation directions of incident and corresponding transmitted beam.

In case of an array with a band structure as depicted in Fig. 31 (a), an increase of the angle of incidence first leads to an increase of the angle of the transmitted Bloch wave. If the angle of incidence exceeds some value, where the corresponding transmitted wave is located at the

inflection point of the band (red arrows), then the angle of the transmitted beam decreases with increasing angle of incidence and can become even zero. However, as the band is shallow, the absolute angles of the transmitted beam are always small. For an interface as depicted in Fig. 31 (b), the angle of incidence can be varied in a wide range while the angle of the transmitted beam keeps almost constant.

Concluding, various investigations of inhomogeneities in waveguide arrays are performed in this chapter. In section 3.3 the range of existence of localized defect states in a waveguide array is analytically determined and experimentally verified. Both, an increase of the coupling constant as well as the variation of the effective index of the defect guide give rise to the formation of localized states. Staggered modes, which are not known from conventional materials, are found. Furthermore it turns out that symmetric defects in waveguide arrays cannot support antisymmetric modes. At the edges of the arrays strong deformation of the waveguides leads to the existence of bound states.

Furthermore, in section 3.4 theoretical investigations on an optical switch based on an electro-optical controllable defect is presented. It is demonstrated that this switch can be used either as an on-off-switch or as a controllable Y-branch.

In the last part of this chapter the propagation of waves in arrays with interfaces is analyzed. In contrast to bulk media, bound states can exist at interfaces in waveguide arrays. Further on, the reflection and transmission coefficients for interfaces are derived.

4. Photonic Zener tunnelling in planar waveguide arrays

In this chapter the field evolution in waveguide arrays with a transversely superimposed linear refractive index distribution is investigated with the aim to experimentally visualize Zener tunnelling. In the first section, an analytical model to describe Bloch oscillations and Zener tunnelling is derived analogue to the quantum mechanical model presented in [Zener34, Holthaus00]. From this model the trajectory of the Bloch oscillations and the tunnelling rate into the second band follow. As the derived model is only an approximation of the real system it is useful to understand the physics, but cannot provide exact quantitative information or describe precisely the field evolution inside the waveguide array. Thus some numerical calculations are presented to obtain more detailed information before discussing the experimental demonstration. Additionally the simulations give the opportunity to pre-estimate the parameters for the fabrication of samples.

In the second part of this chapter an experimental setup for the detection of light inside a planar array is introduced. Measurements of photonic Bloch oscillations accompanied by Zener tunnelling are presented and discussed in comparison with theory.

4.1. Theory

The aim of this section is to derive a simple analytical model to describe the effects of Bloch oscillations and Zener tunnelling. To this end we start from the wave equation (6). We restrict

our investigations to small refractive index variations. Then derivatives of the dielectric function can be neglected. Furthermore we assume an x -polarized electric field and propagation in z -direction. Then the field can be written as $\mathbf{E}(\mathbf{r}) \approx \mathbf{e}_x E_x(x, y, z) \exp(i\beta_0 z)$ with a slowly varying amplitude $E_x(x, y, z)$ and a fast oscillating exponential term. We define the propagation constant β_0 as $\beta_0 = \sqrt{\bar{\varepsilon}} \cdot \omega / c$ with $\bar{\varepsilon}$ being an average value of the dielectric function, e.g. the average of waveguide and cladding index. As $|\partial E_x / \partial z| \ll |\beta_0|$ holds, second z -derivatives of $E_x(x, y, z)$ can be neglected and we obtain a scalar paraxial equation for the x -polarized field

$$\left[2i\beta_0 \frac{\partial}{\partial z} + \frac{\partial^2}{\partial x^2} + \frac{\partial^2}{\partial y^2} + k_0^2 \varepsilon(x, y) - \beta_0^2 \right] E_x(x, y, z) = -\mu_0 \omega^2 P_p(x, y), \quad (72)$$

with $k_0 = \omega / c$. The influence of a superimposed linear potential is included by a polarisation $P_p(x, y)$. $\varepsilon(x, y)$ is the dielectric function, which describes the index distribution of the homogeneous array.

In order to derive an analytical model for Bloch oscillations and Zener tunnelling we simplify equation (72). Therefore we reduce our system to a 1D-problem (Bragg system), as schematically depicted in Fig. 32.

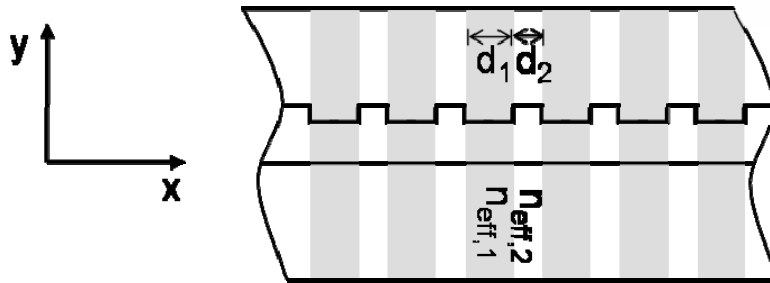


Fig. 32 Scheme for reduction of a 2D waveguide array to a Bragg system.

For a weak modulation in x -direction, we can introduce an effective-index model. In the following we distinguish two different regions, which correspond to an x -position in an area without or with a waveguide ridge. We denote these regions as areas 1 (shaded in Fig. 32) and 2 (white in Fig. 32). If the height of the waveguide ridges is much smaller than their width, we can approximate the shape of the field in y -direction for each area by the modes of the corresponding homogeneous systems consisting of three different layers. Then we can introduce a separation ansatz for the field

$$E_x(x, y, z) = \Phi(x, y) \Psi(x, z). \quad (73)$$

$\Psi(x,z)$ contains the evolution during propagation and $\Phi(x,y)$ the y -dependence of the field in dependence on the transverses position x . It contains x as a parameter which distinguishes only between positions inside the areas 1 and 2. As we assume $\Phi(x,y)$ to be constant inside each area, it can be approximated by the equation for a planar waveguide in both cases

$$\left[\frac{\partial^2}{\partial y^2} + k_0^2 \varepsilon(x, y) - \beta_{eff}^2(x) \right] \Phi(x, y) = 0, \quad (74)$$

with $\beta_{eff}(x) = 2\pi n_{eff}(x)/\lambda$. Here $n_{eff}(x)$ is equal to $n_{eff,1}$ or $n_{eff,2}$ depending of the actual x -position and we obtain a Bragg system of alternating layers with the effective refractive indices $n_{eff,1}$ and $n_{eff,2}$ (see Fig. 32).

We insert eqs. (73) and (74) into eq. (72) and multiply the result by $\Phi(x, y)$. Next we integrate over y and obtain

$$[2i\beta_0 \frac{\partial}{\partial z} + \frac{\partial^2}{\partial x^2} + \beta_{eff}^2(x) - \beta_0^2] \Psi(x, z) = -\mu_0 \omega^2 \frac{\int_{-\infty}^{+\infty} \Phi(x, y) P_p(x, y) dy}{\int_{-\infty}^{+\infty} \Phi^2(x, y) dy}, \quad (75)$$

describing the evolution of $\Psi(x,z)$ during propagation. If we accomplish the integrations over y , this equation becomes independent of y . To calculate this number, the mode profile $\Phi(x,y)$ and the polarisation $P_p(x,y)$ have to be known. $P_p(x,y)$ is the superimposed linear gradient which is induced thermo-optically by heating and cooling the opposite sides of the array. The resulting temperature gradient is converted into a refractive index gradient via the thermo-optic effect inside the polymer material. In a stationary regime of the temperature gradient, the polarisation is given by

$$P_p(x, y) = \varepsilon_0 \chi(x, y) E_x(x, y) \quad \text{with} \quad \chi(x, y) \approx \Theta(y) \frac{\partial \chi}{\partial T} \tau x. \quad (76)$$

Here T is the temperature and τ the transverse thermal gradient $\tau = \partial T / \partial x$, which is assumed to be constant inside the array. $\Theta(y)$ is a step like function, because the thermo-optic coefficient is zero for the substrate but constant inside the waveguides and cladding. However, as the refractive index of the substrate is much lower than the index of the waveguide and cladding material, the overlap of the fields with the substrate material is rather small. Then the influence of $\Theta(y)$ is negligible $\chi(x, y) \approx \chi(x)$ and eq. (75) can be simplified to

$$[2i\beta_0 \frac{\partial}{\partial z} + \frac{\partial^2}{\partial x^2} + \beta_{eff}^2(x) - \beta_0^2] \Psi(x, z) = -\omega^2 \mu_0 \varepsilon_0 \chi(x) \Psi(x, z). \quad (77)$$

Otherwise the integration over y has to be performed. We proceed with the simplified equation (77). In case of a constant refractive index gradient we can write

$$\left[i \frac{\partial}{\partial z} + \frac{1}{2\beta_0} \frac{\partial^2}{\partial x^2} + \frac{\beta_{eff}^2(x) - \beta_0^2}{2\beta_0} - \alpha x \right] \Psi(x, z) = 0, \quad (78)$$

with the gradient

$$\alpha = -\frac{2\pi}{\lambda} n_{th} \tau. \quad (79)$$

n_{th} denotes the thermo-optic coefficient of the polymer, \bar{n} the average refractive index of waveguide and cladding material and λ the vacuum wavelength. Equation (78) is the basis for the following investigations of Bloch oscillation and Zener tunnelling. It is the optical analogon to the quantum mechanical Schrödinger equation of a particle inside a periodic potential with a superimposed linear potential

$$\left[i\hbar \frac{\partial}{\partial t} + \frac{\hbar^2}{2m} \frac{\partial^2}{\partial x^2} - V_{per}(x) - Fx \right] \Psi(x, t) = 0. \quad (80)$$

Comparing both equations we find the evolution in time replaced by an evolution in propagation direction. The periodic potential in the quantum-mechanical system corresponds to the periodic refractive index modulation in optics. Analogous the liner potential is equivalent to a liner refractive index change. This similarity between the quantum-mechanical system and the optical waveguide array enables to find many effects from quantum mechanics to occur as well in periodical optical systems.

Before analysing the influence of the linear gradient, the unperturbed system $\alpha=0$ is examined. Solutions of the unperturbed problem are Bloch waves (cp. section 2.2) of the form

$$\Psi_{n,k}(x, z) = u_{n,k}(x) e^{ikx + i\beta_n(k)z}, \quad (81)$$

with n being the band index and k the transverse wave number (Bloch vector). Inserting the solution (81) into eq. (78) we obtain a z -independent Schrödinger equation

$$\left[\frac{1}{2\beta_0} \frac{\partial^2}{\partial x^2} + \frac{\beta_{eff}^2(x) - \beta_0^2}{2\beta_0} \right] \Psi_{n,k}(x) = \beta_n(k) \Psi_{n,k}(x), \quad (82)$$

with the z -independent Bloch modes

$$\Psi_{n,k}(x) = u_{n,k}(x) e^{ikx}. \quad (83)$$

All field distributions can be expanded into these Bloch modes

$$\Psi(x) = \sum_n \int_{-\pi/a}^{\pi/a} dk g_{n,k} \Psi_{n,k}(x). \quad (84)$$

As both edges of the Brillouin zone are equivalent,

$$g_{n,\pi/a} \Psi_{n,\pi/a}(x) = g_{n,-\pi/a} \Psi_{n,-\pi/a}(x) \quad (85)$$

holds for all Bloch modes. We will need this relation later.

In order to describe the dynamics of a propagating wave packet we investigate a packet which initially ($z=0$) occupies only the first band so that $g_{n,k}=0$ for $n \neq 1$ (even if the following derivation would be possible for a wave packet of a any band n). To simplify the equations we omit the band index in the following equations, keeping in mind that we examine the first band. In particular the wave packet g_k should be smooth and well localized around some value k_c within the first Brillouin zone. Thereby the characteristic width Δk of $|g_k|^2$ has to be small compared with the width of the Brillouin zone. Then $|g(x)|^2$ extends over at least a few lattice periods in real space, with $g(x)$ being the Fourier transform of g_k . For a weak perturbation due to the gradient we assume the dynamics to be completely described by a z -dependent $g_k(z)$. The Bloch modes are assumed to remain unchanged. Then again the field distribution can be expanded into Bloch-modes (see eq. (84)), but this time with z -dependent coefficients $g_k(z)$.

The evolution of $\psi(x,z)$ is given by the Schrödinger equation (78). After integration over the whole first Brillouin zone we can write with (82)

$$\begin{aligned} i \int_{-\frac{\pi}{a}}^{\frac{\pi}{a}} \frac{\partial}{\partial z} g_k(z) \Psi_k dk &= \int_{-\frac{\pi}{a}}^{\frac{\pi}{a}} g_k(z) [-\beta(k) + \alpha x] \Psi_k dk \\ &= - \int_{-\frac{\pi}{a}}^{\frac{\pi}{a}} g_k(z) \beta(k) \Psi_k dk + \int_{-\frac{\pi}{a}}^{\frac{\pi}{a}} \frac{\alpha}{i} g_k u_k \frac{\partial}{\partial k} e^{ikx} dk. \end{aligned} \quad (86)$$

After partial integration of the second term of the right hand side we obtain with (85)

$$i \int_{-\frac{\pi}{a}}^{\frac{\pi}{a}} \frac{\partial}{\partial z} g_k(z) \Psi_k dk = - \int_{-\frac{\pi}{a}}^{\frac{\pi}{a}} g_k(z) \beta(k) \Psi_k dk + \int_{-\frac{\pi}{a}}^{\frac{\pi}{a}} \frac{\alpha}{i} \left[\left(\frac{\partial}{\partial k} g_k \right) u_k + g_k \left(\frac{\partial}{\partial k} u_k \right) \right] e^{ikx} dk. \quad (87)$$

With the assumption of a wave packet that is well localized inside the Brillouin zone and weak k -dependence of u_k (which is a common assumption) we can neglect the k -derivative of u_k and for the integrands the following equation has to hold

$$i \frac{\partial}{\partial z} g_k = -g_k \beta(k) - i\alpha \frac{\partial}{\partial k} g_k. \quad (88)$$

Multiplying this equation with g_k^* and subtracting its conjugate complex we obtain the famous *acceleration theorem*:

$$\frac{\partial}{\partial z} |g_k(z)|^2 = -\alpha \frac{\partial}{\partial k} |g_k(z)|^2. \quad (89)$$

It implies that a linear potential in a periodic system leads to a motion in Fourier space. The solution of this equation takes the form

$$|g_k(z)|^2 = G(k - \alpha z), \quad (90)$$

implying that the wave packet moves through k -space at a constant speed, while preserving its shape. This leads to a linearly growing value for the wave packet's centre

$$k_c(z) = k_0 + \alpha z, \quad (91)$$

with k_0 being the initial position inside the Brillouin zone, which is usually zero corresponding to an excitation with a flat phase. What does this connection between propagation distance z and transverse wave number k mean for the motion of the wave packet in real space? To find out we describe the field by the superposition of the corresponding Bloch modes

$$\Psi(x, z) = \int_{-\frac{\pi}{a}}^{\frac{\pi}{a}} u_k e^{ikx + i\beta(k)z} dk. \quad (92)$$

We develop $\beta(k)$ around the centre of the wave packet k_c into a Taylor series, from which we take only the first two elements, insert them into eq. (92) and obtain

$$\Psi(x, z) = \int_{-\frac{\pi}{a}}^{\frac{\pi}{a}} u_k e^{i(k-k_c)[x + \frac{\partial\beta(k)}{\partial k}|_{k_c} z]} dk \cdot e^{i\beta(k_c)z + ik_c x}. \quad (93)$$

We compare the field for $z=0$ with a field after a certain propagation distance z . Except for a phase, the field distribution at the position z is shifted by $\frac{\partial\beta}{\partial k}|_{k_c} z$ in the transverse direction x .

We call the velocity of the transverse motion during propagation the group velocity v_g of the wave packet

$$v_g = \frac{\partial x}{\partial z} = -\frac{\partial\beta}{\partial k}|_{k_c}. \quad (94)$$

The position of the wave packet at a propagation distance z can be calculated by integration to

$$x_c(z) = -\frac{1}{\alpha} \beta(k_0 + \alpha z) + x_0, \quad (95)$$

with an integration constant x_0 . According to this equation the wave packet moves in real space under the influence of a gradient α along a path of the shape of the corresponding band β . The amplitude and the period of this oscillatory motion are determined by the strength of the gradient α . These oscillations became known as *Bloch oscillations*, although they do not appear in Bloch's ground-breaking paper on quantum-mechanics of electrons in crystal lattices [Bloch28], but seem to be first mentioned by Zener in 1934 [Zener34].

The occurrence of photonic Bloch oscillations can be explained as well in terms of a coupled mode theory, as demonstrated in [Peschel98]. In this case only one cosine-shaped band is taken into account and the oscillations follow a cosine-shaped trajectory in real space, which agrees with the model derived here.

The question Zener traced in 1934 was how the scenario is modified when interband transitions come into play. We are now going to follow his way [Zener34] to solve this problem, but in our case for light waves instead of electrons. When a wave packet is initially prepared in the fundamental band $n=1$, and then cycles through k -space according to the acceleration theorem (89), it experiences a periodically varying energy separation from the next (here second) band and comes closest to it each time it reaches the edge of the Brillouin zone (cp. band structure presented in Fig. 2). So the probability for a transition to the next band is highest there. During this transition the propagation constant β has to be conserved. Fig. 33 schematically depicts the tilt of the bands and gaps due to the gradient in dependence on the transverse coordinate x .

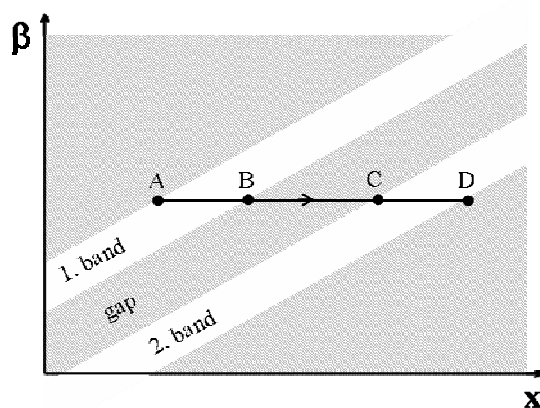


Fig. 33 Schematic band gap diagram in the presence of a linear index gradient. The shaded areas represent zones of forbidden propagation constants (gaps). Light inside the first band tunnels into the second band between points B and C.

A wave packet starts at its excitation in point A and has to follow the horizontal line during propagation. Tunnelling into the second band appears between points B and C. Light inside the first band moves back to point A after reaching point B. The light wave reaches the bottom of the first band and thus comes closest to the second band once per Bloch cycle. At this point it is partially transmitted into the second band and we can estimate the transmission rate [Landau67]

$$|T|^2 \approx \exp\left(-2 \int_B^C dx |\operatorname{Im}[k(x)]|\right), \quad (96)$$

provided that there is no back-feeding from the second band to the initial one. The transmission is determined by the imaginary part of k , which describes the attenuation of the evanescent field inside the gap. The weaker this attenuation is the more light leaks through the gap and the higher the tunnelling becomes. Now we are left with the task to calculate $\operatorname{Im}[k(x)]$ inside the gap. From a perturbation theory for a weak effective index modulation (see [Holthaus00, Kirejew74]) it can be shown that

$$\operatorname{Im}[k(\beta)] \approx \operatorname{Im}[k_{\max}] \sqrt{1 - \frac{(\beta - \beta_c)^2}{(\Delta\beta/2)^2}} \quad (97)$$

holds inside the gap. Here β_c is the value of β in the centre of the gap, k_{\max} the corresponding k -value and $\Delta\beta$ the width of the gap. With the gradient α we can write $\beta - \beta_c \approx \alpha x$. Then we can calculate the integral and obtain for the transmission

$$|T|^2 \approx e^{-\frac{|\operatorname{Im}(k_{\max})\Delta\beta\pi}{2\alpha}|}. \quad (98)$$

As expected, the tunnelling increases with increasing gradient and decreasing band gap. Therefore, to obtain a sufficiently strong coupling at a realistic gradient we have to choose a geometry with fairly small band gap.

To estimate the transmission for a waveguide array, as it is used in this work for the experimental demonstration of Zener tunnelling, the values of $\operatorname{Im}(k_{\max})$ and $\Delta\beta$ have to be determined. The investigated array consists of 3 μm wide and 0.5 μm thick waveguide ribs placed on a 2.5 μm thick polymer layer of the refractive index $n_{Co}=1.5615@ \lambda=488\text{nm}$ with a period of $d=7\mu\text{m}$. The substrate refractive index is $n_s=1.457@ \lambda=488\text{nm}$ and the index of the 10 μm thick cladding $n_{Cl}=1.5595@ \lambda=488\text{nm}$. For this structure the effective indices of the corresponding Bragg system are calculated as $n_{eff,1}=1.5604$ and $n_{eff,2}=1.5602$. We calculate the band structure of the 1D-system using the transfer matrix method [Börner90]. For a Bragg system

of two alternating layers of the thicknesses d_1 and d_2 the equations for the fast propagation constant $\bar{\beta}(k) = \beta_0 + \beta(k)$ read as

$$\cos[\bar{\beta}(k)d] = \frac{M_{11} + M_{22}}{2}$$

with

$$\begin{aligned} M_{11} &= \cos(k_1 d_1) \cos(k_2 d_2) - \frac{k_2}{k_1} \sin(k_1 d_1) \sin(k_2 d_2), & k_1 &= \sqrt{\left(\frac{2\pi}{\lambda} n_{eff,1}\right)^2 - \bar{\beta}^2}, \\ M_{22} &= \cos(k_1 d_1) \cos(k_2 d_2) - \frac{k_1}{k_2} \sin(k_1 d_1) \sin(k_2 d_2), & k_2 &= \sqrt{\left(\frac{2\pi}{\lambda} n_{eff,2}\right)^2 - \bar{\beta}^2}. \end{aligned} \quad (99)$$

The results are depicted in Fig. 34 by the red lines. To check the validity of our effective index model we additionally calculate the band structure for the 2D problem using the band solver MIT Photonic-Bands (black lines) and compare it with the band structure from the effective index approximation (red lines). We obtain excellent agreement between the waveguide bands for both methods. The full problem additionally provides the bands of the cladding modes, which are a discrete set of modes due to the finite thickness of the cladding.

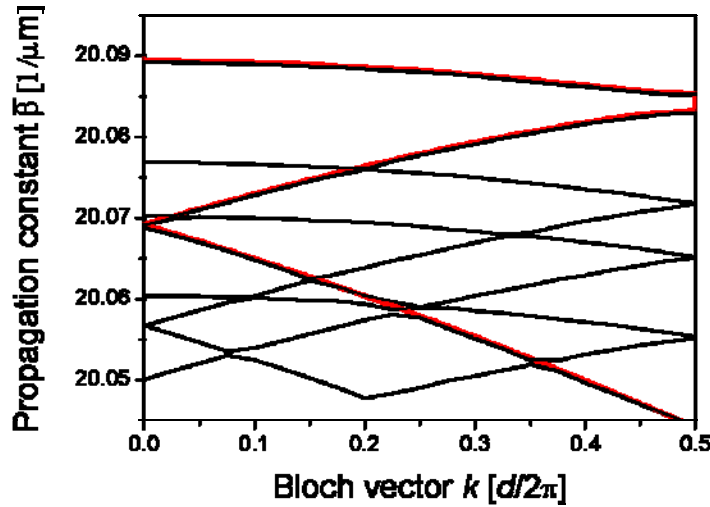


Fig. 34: Band structure for a waveguide array. The black curves show the results for the solution of the 2D problem while red curves show the bands calculated by the transfer matrix method for the corresponding Bragg system.

We can also determine the value of $\text{Im}[k(\bar{\beta})]$ by the transfer matrix method. In Fig. 35 we compare a curve calculated by eq. (97) with the result of the transfer matrix method. We use the parameters $\Delta\beta=0.0011 \mu\text{m}^{-1}$, $\text{Im}(k_{max})=0.049 \mu\text{m}^{-1}$ and $\bar{\beta}_c=20.0843 \mu\text{m}^{-1}$. Both results show good agreement.

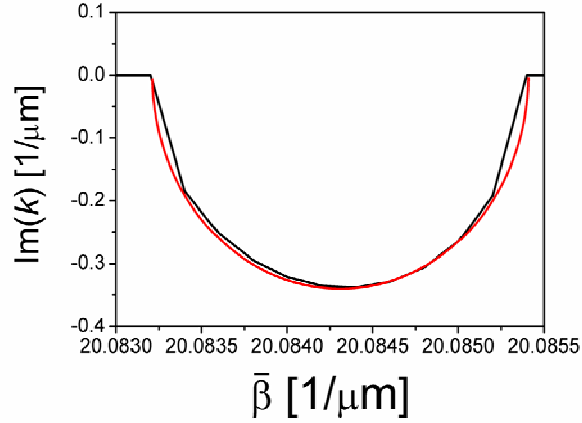


Fig. 35 Comparison of $\text{Im}(k)$ inside the gap calculated by the transfer matrix method (black line) and calculated by eq. (97) with parameters $\Delta\beta=0.0011 \mu\text{m}^{-1}$, $\text{Im}(k_{\text{max}})=0.049 \mu\text{m}^{-1}$ and $\bar{\beta}_c=20.08431 \mu\text{m}^{-1}$.

To calculate the gradient α we use eq. (79) with the thermo-optic coefficient $n_{th}=-2*10^{-4}\text{K}^{-1}$ for the used polymers. The transverse temperature gradient τ is determined by the applied temperature difference ΔT divided through the width W of the sample. The transmission per Bloch oscillation is calculated with the given parameters and depicted in Fig. 36 in dependence of the applied temperature difference.

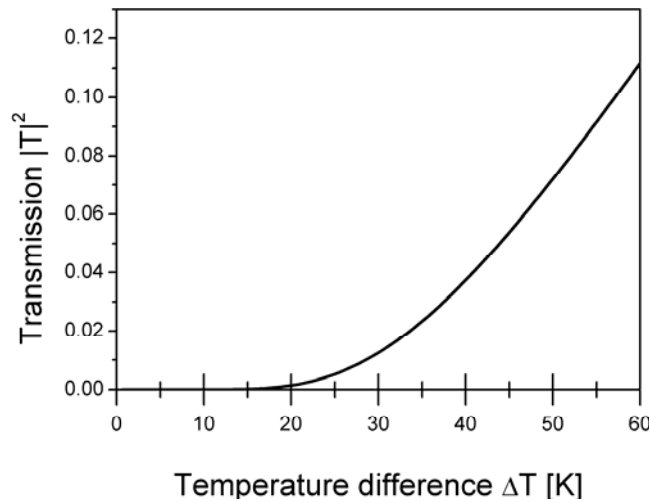


Fig. 36 Transmission from first into second band due to Zener tunnelling in dependence of applied temperature difference.

However, calculating the transmission, the approximate character of the derived model should not be forgotten. Its value is more the qualitative description of the physics of Bloch

oscillations and Zener tunnelling rather than giving exact numbers. To obtain quantitative information numerical simulations have to be used.

In order to fabricate samples for experimental demonstration of Zener tunnelling we investigate how waveguide arrays have to be designed to provide appropriate tunnelling at moderate index gradients. As eq. (98) shows, the tunnelling rate is influenced by different parameters. For the design of samples in particular the possibility to choose the gap width by the geometry parameters is of importance.

To obtain first estimations we compare band structures calculated for different Bragg systems by the transfer matrix method. Fig. 37 shows the dependence of the first band on the refractive indices n_1 and n_2 of the two different layers with thicknesses d_1 and d_2 (compare Fig. 32). In Fig. 37 (a) the influence of a change of the refractive index of the layer corresponding to the waveguides (or index difference between both layers) is illustrated. The value of n_1 is increased by $2 \cdot 10^{-4}$ between the dashed and solid lines and solid and dotted lines, respectively. The main influence of this variation is clearly a change in the gap width. Besides this, only a small deformation of the bands occurs. This dependence can be understood, having the origin of the band structure in mind. For a homogeneous medium the diffraction relation is a circle or a parabola in paraxial approximation. Going over from a homogeneous medium to a periodic structure this relation is folded back into the first Brillouin zone at $k = \pm\pi/d$. For a periodic structure a gap appears at these points. While the energy of the modes from the first band is concentrated in the high index areas, energy of the modes of the second band it is concentrated in the low index areas [Joannopoulos95]. Therefore the propagation constant from the bottom of the first band and the top of the second band must be different. The weaker the modulation or refractive index difference between the two alternating layers, the smaller is the difference between these modes and the smaller is the gap. This leads to a small gap for weak modulation and vice versa.

In Fig. 37 (b) and (c) the influence of the width of the two layers is investigated. In this case especially the shapes of the bands depend strongly on the parameters while only small changes in the gap width are obtained. The variation of d_2 in Fig. 37 (b) corresponds to a variation of a spacing of the respective waveguides. From a coupled mode theory it is known, that the width of a band is directly correlated to the coupling between adjacent guides. In other words we can influence the width of the bands via the spacing of the guides. The larger d_2 the narrower the bands become.

The change in the bandwidth in Fig. 37 (c) can be understood in the same sense. For a narrower waveguide the field laps further out of the guides and thus the coupling increases, leading to a wider band.

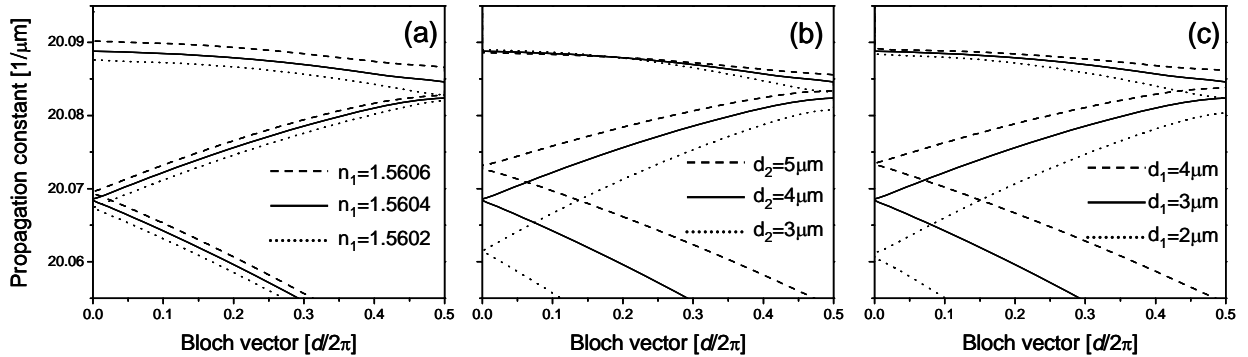


Fig. 37: Band structures of Bragg systems with refractive indices n_1 and n_2 of alternating Bragg layers of thickness d_1 and d_2 . Unless stated otherwise inside the insets, the parameters are $n_1=1.5601$, $n_2=1.5604$, $d_1=3\mu\text{m}$, $d_2=4\mu\text{m}$.

Keeping these results in mind, we design samples for the experimental demonstration of Zener tunnelling. In earlier observations of Bloch oscillations in polymer waveguide arrays [Pertsch99a] samples consisting of weakly coupled channel waveguides have been used. To describe propagation in these samples a coupled mode (tight binding) approximation was applied. Coupling to the second band was neglected because of a large gap. Therefore these structures were unsuitable for our experiments. In order to achieve strong tunnelling we have to decrease the gap width. Referring to the previous investigations on the 1D system, this can be achieved by a weaker periodic modulation. For our samples we reduce the gap width by a change of the geometry from channel to rib waveguides, with an underlying polymer layer as depicted in Fig. 1. Then the index contrast is determined by the ratio between the height of the layer and of the ribs.

To obtain a more precise picture of the field evolution inside the arrays BPM-simulations were performed. The simulated propagation of a broad light beam that excites several waveguides clearly shows Bloch oscillations and Zener tunnelling (see Fig. 38). While the earlier used tight binding model predicts a sinusoidal trajectory [Peschel98, Pertsch99a], we observe a kind of connected parabolas with rounded shapes in the low-index area and almost cusps on the high index side. As predicted by eq. (95), the trajectory resembles the shape of the first band.

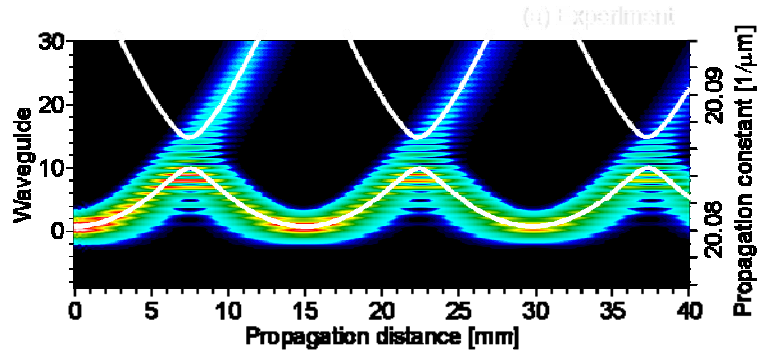


Fig. 38: BPM simulation in comparison with corresponding bands of the structure.

In Fig. 38 the first two bands are plotted on top of the results from a corresponding BPM simulation. The simulation was performed for an array with an $8\ \mu\text{m}$ substrate with a refractive index of $n_s=1.457@ \lambda=488\text{nm}$. The indices of waveguide and cladding material were assumed to be $n_{Co}=1.5615@ \lambda=488\text{nm}$ and $n_{Cl}=1.5595@ \lambda=488\text{nm}$ respectively. The waveguides consisted of $0.5\ \mu\text{m}$ high ribs on a $2.5\ \mu\text{m}$ thick polymer layer with a period of $7\ \mu\text{m}$ at a waveguide width of $3\ \mu\text{m}$. Besides the perfect agreement between the trajectory of the Bloch oscillations and the first band, as well an agreement between the radiation and the second band of the structure is obvious.

In principle, light tunnelled to the second band follows the band structure and may again perform Bloch oscillations. However, in this example the gaps between higher bands are much smaller than the first gap and light successively tunnels towards higher bands without having the chance to complete further oscillations.

For a fixed gradient the tunnelling rate (transmission) can be varied by the geometry parameters and refractive index contrast between waveguide and cladding. An example is given in Fig. 39, where the propagation is depicted for three different ratios of the heights of the layer and the waveguide ribs. Except for these two parameters we used the same values as above.

Obviously the tunnelling rate can be varied in a wide range. For relatively large waveguide ribs we obtain strong guiding, which leads to a large gap to the second band. As a consequence no tunnelling appears in the simulation (Fig. 39 (a)). If the periodic modulation is decreased, the gap becomes smaller. Accordingly the tunnelling grows, as demonstrated in Fig. 39 (b) and (c). A decrease of the modulation was achieved by a reduction of the height of the waveguide ribs and an increase of the underlying layer.

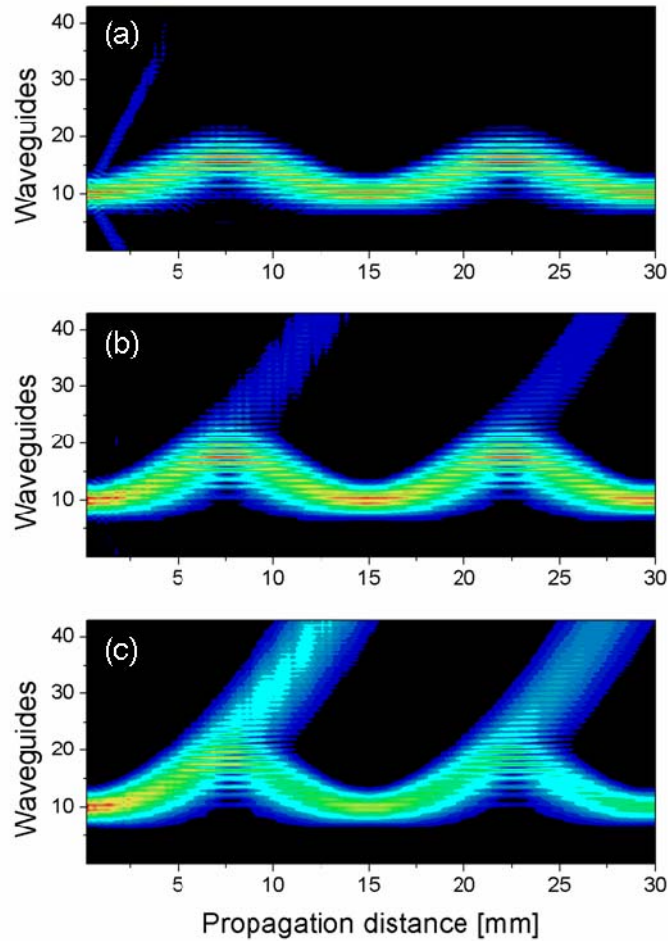


Fig. 39 Simulations of Bloch oscillations and Zener tunnelling inside waveguide arrays with different ratios of layer and rib heights. The sum of layer and rib height was $3 \mu\text{m}$ for all three simulations and the rib height varied from (a) $1 \mu\text{m}$ to (b) $0.5 \mu\text{m}$ and (c) $0.3 \mu\text{m}$.

4.2. Experiment and discussion

To observe Zener tunnelling experimentally a new setup was developed. In earlier experiments on waveguide arrays [Pertsch99a, Pertsch02] the intensity distribution was detected at the output facet of the sample, which does not permit to obtain information about the evolution during the propagation itself. To overcome this limit we established a system, which enables to detect the propagating light from above the array (see Fig. 40).

Using a cylindrical telescope and a microscope objective, a laser beam is coupled into the front facet of the array. The cylindrical telescope enables to create an elliptical spot of variable width in order to excite a predetermined number of waveguides.

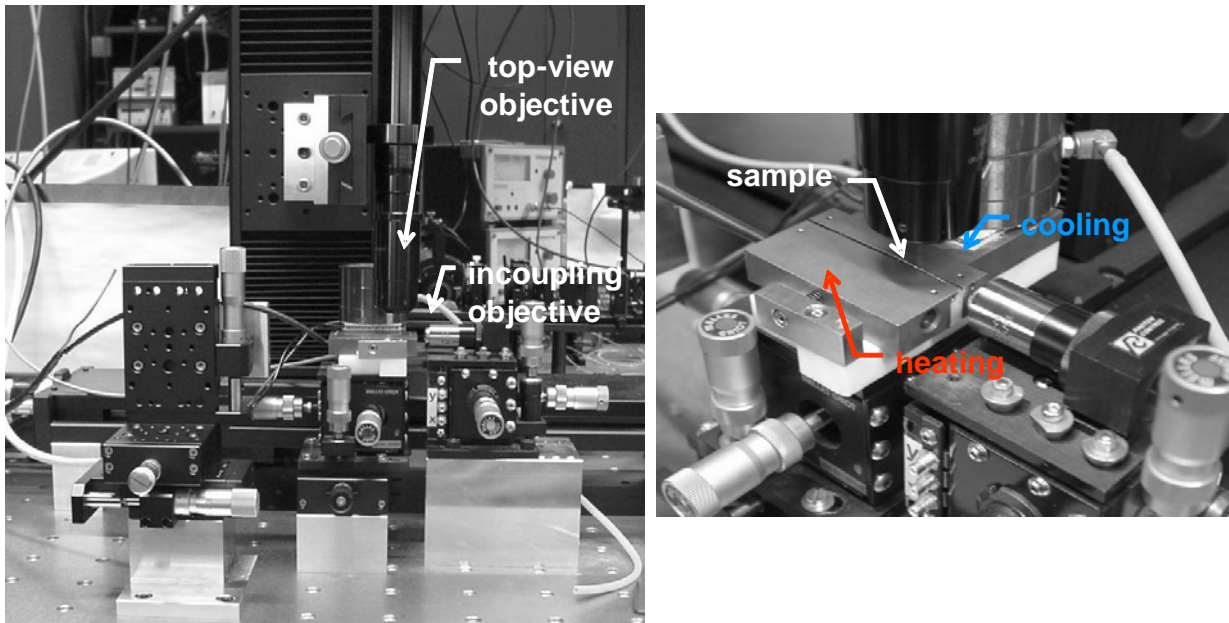


Fig. 40 Experimental setup for visualization of the propagation inside a waveguide array. A top-view objective mounted on a controllable translational stage enables for scanning along the sample. Heating and cooling of the sides of the array is achieved by a special mount consisting of copper blocks.

The array itself is mounted between two copper blocks, enabling to heat and cool the opposite sides of the array to create a refractive index gradient via the thermo-optic effect.

The most intuitive way to obtain information about the evolution of the propagating light is the observation of the scattered light, which escapes the array at the surface of the cladding. To this end an imaging system consisting of a microscope objective and a CCD-camera is mounted vertically above the waveguide array. To be able to resolve single waveguides inside the array we chose a magnification of 10 for this system. This gives us an image of an area of the size of about 1×1 mm. To obtain an image of the whole array, the imaging system is mounted on a translational stage, enabling to scan along the propagation direction. The single pictures for different positions are then composed to a single picture showing the whole array.

First tests of this system were made imaging the propagation in homogeneous arrays or arrays with a defect guide as used in section 3.3.2. However, the results were not of the expected quality as speckle pattern limit the resolution (Fig. 41 (a)).

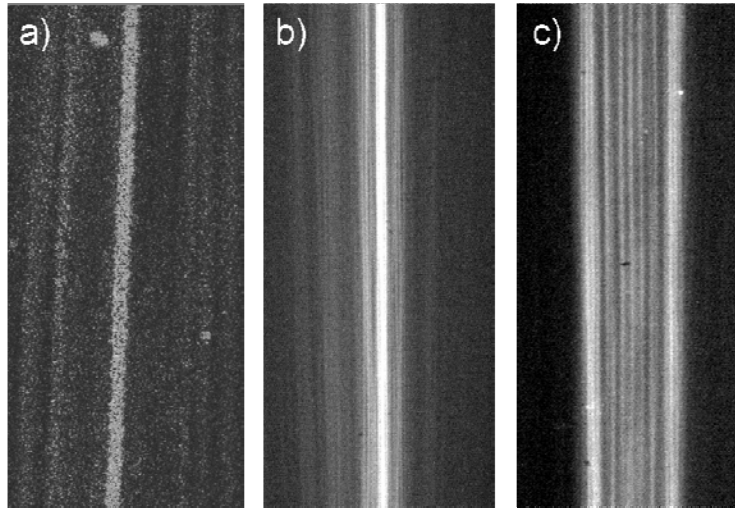


Fig. 41. Examples for direct measurements of propagation. Pictures show single shots of a CCD-camera mounted above the sample. a) Measurement of scattered light of a defect mode shows speckle pattern. b) Measurement of fluorescence of a defect mode with much higher resolution than achieved in a). c) Discrete diffraction measured detecting the fluorescence.

To avoid this problem we record the intrinsic fluorescence of the polymer instead of the scattered light. To excite the fluorescence efficiently, we choose a wavelength of 488nm for our laser beam. The fluorescence of the polymer appears in a wide spectral range of 500-650nm. Fig. 42 shows the measured spectrum of light detected above the cladding of the array.

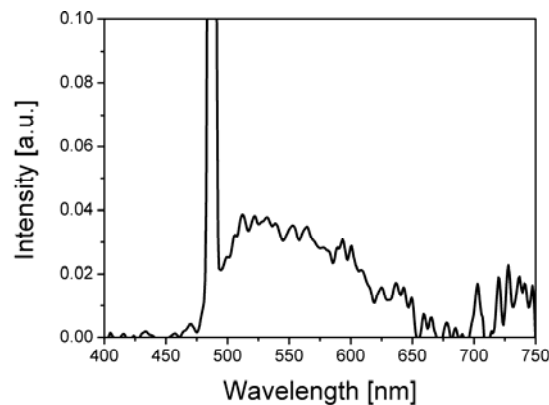


Fig. 42 Spectrum of light detected above the sample. The strong peak around 488nm corresponds to the excitation.

Wavelengths below 530nm are blocked by an edge filter inside the imaging system in order to filter out the excitation wavelength. Relying on this technique the image quality is considerably improved by eliminating the deteriorating speckle pattern. Fig. 41 (a) and (b) show

measurements of the propagation along a defect guide. In Fig. 41 (a) we detected the scattered light and in Fig. 41 (b) the fluorescence. Clearly the resolution is improved by measuring the fluorescence. The diffraction pattern shown in Fig. 41 (c) demonstrates that in this technique single waveguides can be resolved.

A disadvantage of this technique is the strong time dependence of the strength of the fluorescence. During the measurements the fluorescence decays quickly. It is brightest during the first few seconds after which a regime with a slow decay is reached, where measurements can be performed for a couple of minutes. The decay takes place only in regions of the array, where relatively high intensities were obtained before. Thus already after the first measurement the fluorescence becomes inhomogeneous. This usually prohibits further measurements at the same sample.

Since in Fig. 41 only short sections of the propagation were detected, we performed another test to check whether it is possible to observe the evolution for a longer propagation distance. To this end we scanned along a waveguide array and measured the diffraction pattern, which appears at the excitation of a single waveguide. Fig. 43 displays the measurement of discrete diffraction inside the array over a propagation distance of 15mm. To obtain the measurement 16 images were composed to a single picture.

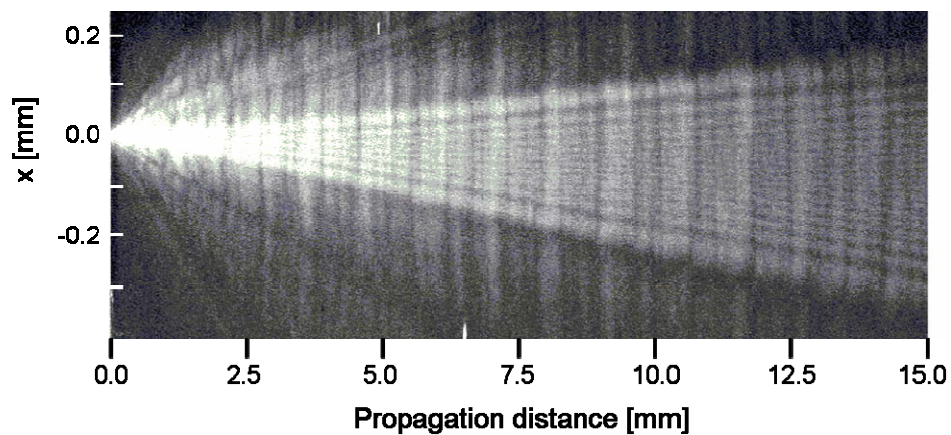


Fig. 43 Discrete diffraction inside a homogeneous waveguide array measured by scanning along the propagation direction and detecting the fluorescence above the array.

For the observation of photonic Zener tunnelling waveguide arrays with a length of 7cm were fabricated by UV lithography from an inorganic-organic polymer ($n_{Co}=1.5615 @ \lambda=488\text{nm}$) on 4" Si-wafers covered with SiO_2 ($n_S=1.457 @ \lambda=488\text{nm}$) with a polymer cladding ($n_{Cl}=1.5595 @ \lambda=488\text{nm}$). Every array consists of 150 ridge waveguides being 2.5 to 3.0 μm wide and

arranged with a period of $d=5.5$ to $7\mu\text{m}$ (see Fig. 1). For a clear observation of photonic Zener tunnelling ridge waveguides of 0.5 and $1\mu\text{m}$ height on a $2.5\mu\text{m}$ -thick waveguiding layer were used.

When applying a temperature drop ΔT between the opposite sides of the array, the thermo-optic effect causes a linearly varying refractive index across the sample. The thermo-optic coefficient of the polymer is $n_{\text{th}}=-2*10^{-4}\text{K}^{-1}$. Consequently, the wave number grows linearly in transverse direction with an inclination of $\alpha=-2\pi n_{\text{th}}\Delta T/(W \lambda)$ (cp. eq. (79)), where $W=1\text{mm}$ is the width of the array and $\lambda=488\text{nm}$ the wavelength of the argon ion laser used in the experiment.

In the following the results of our measurements are discussed in comparison with simulations. To measure Bloch oscillations and Zener tunnelling a $25\mu\text{m}$ wide elliptical input beam is used to illuminate approximately five waveguides. Thus, only a narrow angular spectrum is excited. In addition, the height of the input beam is adjusted to $3\mu\text{m}$ in order to excite mainly modes of the lowest order band. The resulting light propagation in the array with a transverse wave number gradient of $\alpha=6.2*10^{-5}\mu\text{m}^{-2}$ is monitored (see Fig. 44 (a)).

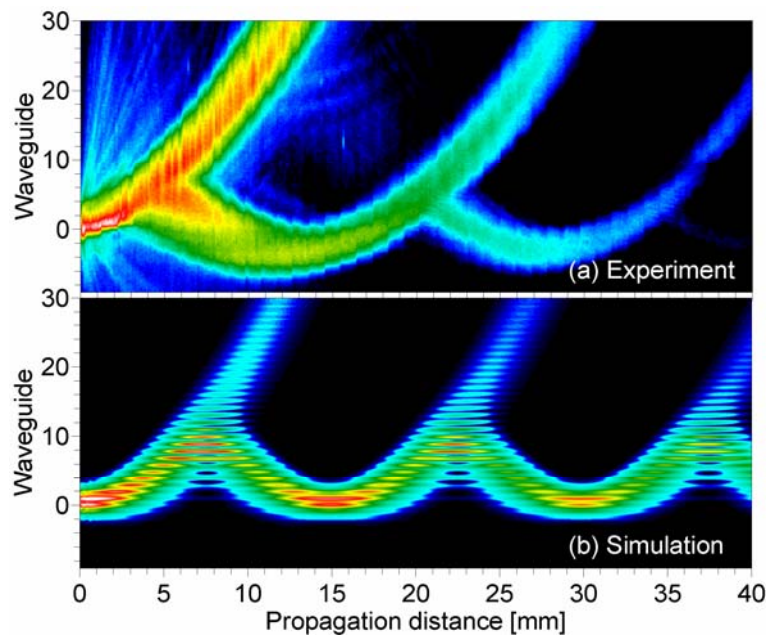


Fig. 44 Bloch oscillations and Zener tunnelling in a waveguide array when several waveguides were excited by a $25\mu\text{m}$ wide elliptical beam. (a) Experiment, (b) corresponding BPM-simulation. (temperature difference $\Delta T=24\text{K}$).

The gradient α is determined from the Bloch oscillations period. From eqs. (79) and (95) it can be easily derived that $\alpha=2\pi/(L_B*d)$, where L_B is the period of the Bloch oscillations. From the measurements we obtain $L_B=14.4\text{mm}$. With the thermo-optic coefficient being $n_{\text{th}}=-2*10^{-4}\text{K}^{-1}$ the temperature difference between the sides of the array is calculated as 24K. With an applied temperature difference of 58K we find that about 58% of the temperature difference drops off at the contacts between the probe and the copper blocks while only 42% contribute to the index gradient. The simulation corresponding to Fig. 44 (a) is depicted in Fig. 44 (b). For both, simulation and experiment we used arrays of 3 μm wide waveguides periodically arranged with a period of 7 μm .

Both, measurement and simulation show that the light performs Bloch oscillations. The trajectory of the oscillations clearly resembles the shape of the first band, as predicted by eq. (95). At the high index side a sharp change in the transverse velocity appears analogue to the shape of the first band at the edge of the Brillouin zone. In contrast to this sharp transition on the low index side the beams trajectory has a parabolic shape, as expected for the acceleration inside a linear potential. It can be recognized from Fig. 44 that light escapes from Bloch oscillations at the high index turning points corresponding to the edge of the Brillouin zone. At these edges the band gap attains its minimum and the tunnelling rate its maximum.

Besides the good qualitative agreement between simulation and measurement also some differences are visible. The experiments show a higher tunnelling rate than the simulations. Moreover a decay of the intensity in propagation direction appears in the measurements. Several reasons might contribute to these effects. One is the nonlinear dependence of the fluorescence on the intensity inside the array. Another reason might be a weaker periodic modulation of the samples than assumed for the simulations. As a result of the lithography process the shape of the waveguides can deviate from the ideal rectangular cross section, which leads to a decrease of the modulation. The decay in propagation direction is caused by a weak absorption, which is the origin of the fluorescence. This absorption was neglected in simulations.

To clearly identify Zener tunneling as the source of the bursts of radiation we varied the index gradient α by changing the temperature difference ΔT . For different measurements and values of ΔT we extracted cross sections along the z -direction from the measurements. We chose these x -positions so, that the tunnelled light just left the first band. The result is shown in Fig. 45 together with one example of the obtained cross sections. The acceleration theorem (89) predicts the period of Bloch oscillations to be proportional to the inverse of the gradient (see eq. (95)). The particular propagation distances, for which outbursts of radiation were detected,

followed the same rule - a $1/\Delta T$ dependence. Hence, the observed radiation was strictly correlated with the Bloch oscillations as expected from Zener tunneling.

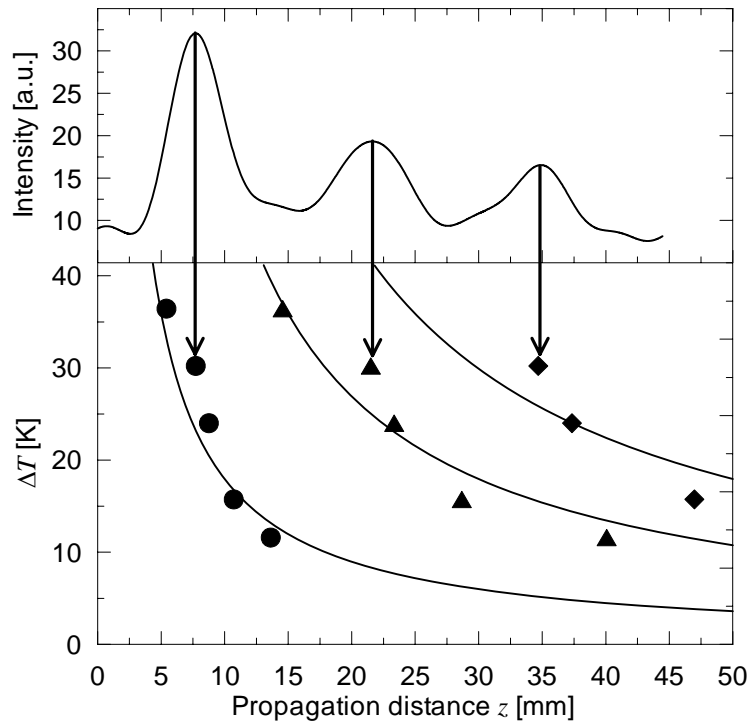


Fig. 45 Position of the radiation due to Zener tunnelling in dependence of the applied temperature difference ΔT . In correspondence to the Bloch oscillation period, a $1/\Delta T$ dependence is observed.

Up to now we have focused on experimental conditions, where photons behave very similar to electrons. To complete the picture another experiment has been carried out, which can be hardly performed in solid-state physics (e.g. semiconductor superlattices). Rather than exciting a few waveguides (narrow Bloch vector spectrum) light was only fed into a single waveguide of the array. In the spectral domain this corresponds to an excitation that extends over the entire Brillouin zone, usually not achievable in semiconductor superlattices. The samples used in this experiment have a period of $6\mu\text{m}$, while the other parameters remain the same as before. While for broad excitations Bloch oscillations are observed as a transverse motion of the centre of the light beam, this centre is now at rest but the field distribution breathes (see Fig. 46).

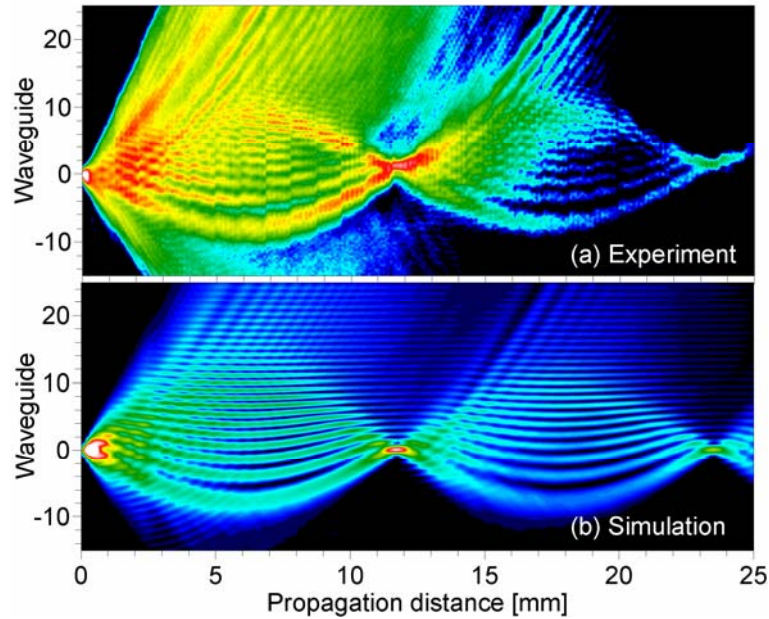


Fig. 46 Bloch oscillations and Zener tunnelling in a waveguide array when the entire Brillouin zone spectrum is excited by shining light in a single waveguide. (a) Experiment, (b) corresponding numerical simulation (temperature difference $\Delta T=35$ K).

The reason for this is that now Bloch waves with all Bloch vectors k are excited. For each Bloch wave the acceleration theorem (89) holds and consequently the superposition of any number of Bloch waves has to evolve periodically under the influence of a linear transverse force. In this respect it is no surprise that Zener tunnelling appears too, but with a different pattern than for a wide beam excitation. Because the entire Brillouin zone is excited and some part of the spectral distribution is always located at the band edge, tunnelling appears upon the whole Bloch oscillations period. However, at the points, where the initial field distribution recovers and light focuses to the initial waveguide, tunnelling is particularly pronounced. If light is concentrated in a single waveguide all radiation escaping due to Zener tunneling is in phase and must follow the same path. Due to constructive interference a well-defined trace of fluorescence can be observed to cross the sample. In contrast radiation emanating between the points of refocusing is distributed over many guides and no coherent enhancement occurs.

The effects discussed so far are in perfect agreement with theory. However, we also obtained measurements which deviate remarkably from the simulations we did so far. Radiation appears where it is not expected and cannot be explained by coupling between first and second band. Fig. 47 shows the propagation inside an array with a period of $5.5\mu\text{m}$ and otherwise the same parameters as above (cp. parameter of measurements shown in Fig. 44 and Fig. 46).

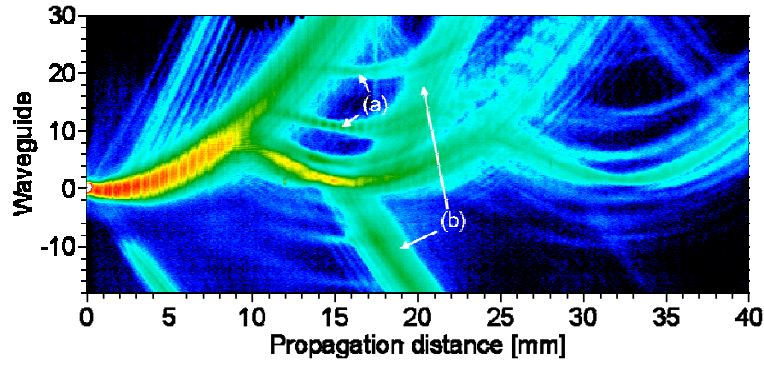


Fig. 47 Experimental observation of a cascade of Bloch oscillations and Zener tunnelling between different bands for an excitation with a broad, more circular beam (as in Fig. 44) and for strong coupling to modes propagating mainly in the cladding (temperature difference $\Delta T=24$ K).

Besides the Bloch oscillations and the tunnelling into the second band clearly additional radiation can be observed. We distinguish two different kinds of radiation, which are marked as (a) and (b). In the following the origin of these effects is discussed.

We start with the discussion of the radiation marked as (a) in Fig. 47, which seems to escape from the second band. To find its origin, we again examine the band structure (Fig. 34). Thereby we take into account the discrete set of cladding modes obtained from the solution of the 2D eigenvalue problem instead of the usually assumed continuum. We know that light tunnels from the first to the second band at the edge of the Brillouin zone. After this point light inside the first band moves further through Fourier space, but also the light in the second band moves with the same transverse velocity. To see what happens during further propagation, we illustrate the path of the light inside the band structure. Tunnelling from the first into the second band is marked as a dashed line at the edge of the first Brillouin zone $k=0.5$. The second band intersects with two cladding modes before reaching again the centre of the Brillouin zone at $k=1$. At the points where the bands intersect, light couples from the second band to the corresponding cladding mode thereby changing its direction of propagation in real space. This coupling is the reason for the experimentally detected radiation out of the second band (Fig. 47 (a)).

From the theoretical investigation we know, that the trajectory of the light in real space has roughly the same shape as the trajectory in Fourier space. Comparing the red curve Fig. 48 (upside down) with Fig. 47, we find this again confirmed. The number of the experimentally detected traces varies between measurements in different samples. These variations are due to different geometries of the samples, e.g. thicker or thinner cladding, causing a different number of cladding modes crossing the second band.

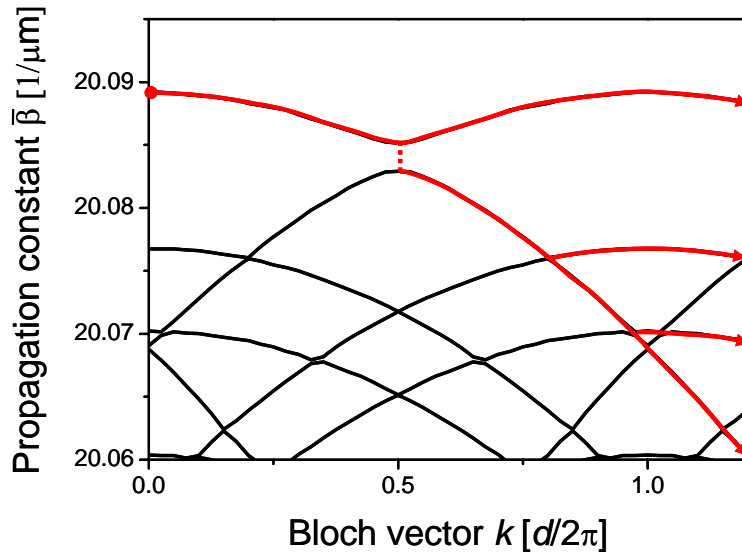


Fig. 48 Path of light in Fourier space for excitation of first band including coupling to cladding modes.

To verify this explanation more simulations were performed. Fig. 49 displays some results. The field distribution along the propagation direction is shown inside the waveguide layer and cladding. While we find the Bloch oscillations and the light inside the second band concentrated in the waveguide layer, the investigated radiation is located mainly inside the cladding, which confirms the occurrence of coupling from the second band into the cladding modes.

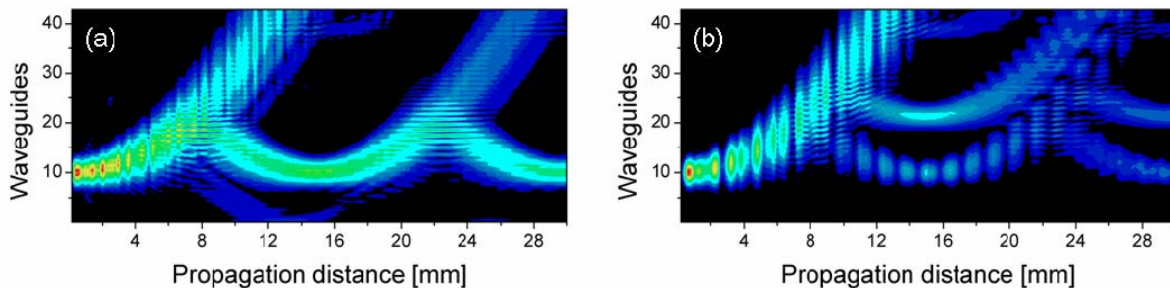


Fig. 49 Numerical results for propagation inside a waveguide array shown inside waveguide layer (a) and cladding (b).

However, we can even learn more from this simple picture. Without coupling of light from the second to higher order bands, light inside the second band would have to perform Bloch oscillations with approximately the shape of the second band. Thus, we would expect the light inside the second band to turn back in the opposite transverse direction when reaching the edge of the Brillouin zone. Obviously this is not the case. The reason is, that most of the light inside

the second band tunnels into the third band (see red curve in Fig. 48), as they are separated by only a tiny gap. The remaining light in the second band is weak and hard to detect in experiments. In Fig. 47 the remaining light in the second band is visible as a weak beam, coming back from the upper edge of the picture. A very similar situation could be observed as well in simulations, which confirms this assumption.

Next we try to find the reason for the radiation marked as (b) in Fig. 47. A strong beam is emitted at a large angle from the light performing Bloch oscillations. It propagates almost on a straight line. This effect cannot be explained in terms of coupling between bands assuming that only the first band is excited, but appears due to the simultaneous excitation of cladding modes at the beginning of the arrays due to imperfect in-coupling. If we again examine the band structure (Fig. 50) we find that the bands of the first cladding modes (blue and red solid lines) have a similar shape as the first waveguide band. They differ mainly by the absolute value of the propagation constant β . Consequently, we expect light in these cladding modes to behave very similar to light inside the first band during propagation. In particular, if we excite the first band of waveguide and cladding modes simultaneously, their diffraction and trajectory should be similar and we cannot distinguish between them by our detection technique. However, there is still an indication for the excitation of cladding modes that we can find in experiment (Fig. 47) and simulation (Fig. 49). This is the beating between the different excited modes, which appears as a modulation in propagation direction. If this beating is visible in the experiment or simulations, we can conclude that we excited both, waveguide and cladding modes.

However, we still do not know the reason for the additional beams found in our measurements (Fig. 47 (b)). These beams propagate at large angles inside the array. Keeping in mind that the angle of propagation is related to the derivative of the respective band, we find the propagation angle of light inside the first waveguide or cladding bands limited. This limit is lower than the propagation angle of the measured beams. Therefore we can attribute them to higher order waveguide or cladding bands. These bands show a steeper characteristic in the band structure diagram and enable for larger propagation angles. Having in mind the relation between maximum propagation angle inside the array and the shape of the corresponding band, we relate the radiation emerging from the Bloch oscillation to propagation inside the third waveguide band (see green line in Fig. 50). We still have to find out, how light couples into this band. The third waveguide band is not excited efficiently. Moreover, the radiation escapes the Bloch oscillations and not the excitation point. For these reasons coupling from other bands must take place. These bands must belong to the cladding modes, which we identified as the reason of the beating in Fig. 47 and Fig. 49. We investigate, if light of these cladding modes

can couple into the third waveguide band. Therefore intersections of the respective bands in Fig. 50 are necessary. One intersection of a cladding band (solid red line) and the third waveguide band (green line) exists. During propagation, a part of the light inside the cladding mode radiates into the third band at this intersection. Afterwards it follows the path marked by the red dashed line.

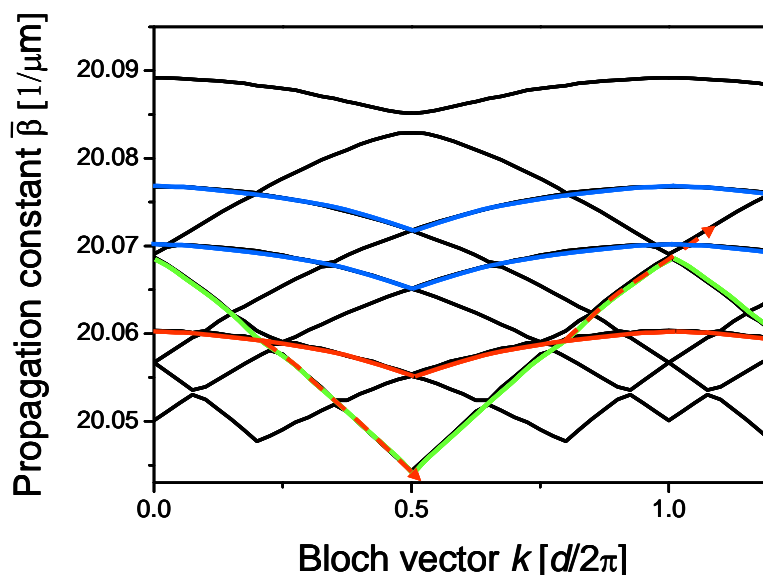


Fig. 50 Band structure of waveguide array to illustrate coupling between third waveguide band (green) and cladding modes. Red lines illustrate the path of light inside the third cladding mode (solid line) and coupling to the third waveguide mode (dashed line).

Remembering that the path of light inside the band structure can be mapped onto the trajectory of light in real space, radiation should appear upwards before reaching the edge of the first Brillouin zone and downwards afterwards. We examine if this agrees with the measurements. In Fig. 47 radiation appears in both directions at the excitation point. However, at this point light that couples into the third band from cladding modes is not distinguishable from light that is directly coupled into the third band at the excitation. To obtain a clear picture the propagation further inside the sample has to be examined. Radiation occurs shortly before and after reaching again the centre of the Brillouin zone. This fits to the picture worked out above, except for the fact that, according to Fig. 50, the distance between the appearances of the radiation should be much larger. Again, the exact position of intersections between different bands depends on the geometry of the samples and the thickness of the cladding, which are not exactly known. Thus for different samples, radiation appears at different points. This was

confirmed by experiments performed in samples with different waveguide and layer geometries.

To suppress the excitation of cladding modes the excitation has to be carefully adjusted to the modes of the first band. For the measurements presented earlier in Fig. 44 and Fig. 46 we used a beam, which was narrow in y -direction. Therefore almost no cladding modes were excited and only Bloch oscillations inside the first band appear. This is confirmed by the fact, that no beating is superimposed to the Bloch oscillations.

In conclusion, in this chapter the first direct visualization of Zener tunnelling was demonstrated. In the first section we found that Zener's theory can be applied to photons. We derived a general theory of Bloch oscillations and Zener tunnelling in waveguide arrays. In the second section we experimentally demonstrated these phenomena. Zener tunnelling was observed as a regular outburst from the Bloch oscillations into higher order bands. If additional cladding modes are excited, the interaction becomes more complex and Bloch oscillations in the first waveguide and cladding bands are observed simultaneously. All measurements are in excellent agreement with simulations.

5. Bloch oscillation and Zener tunnelling in two-dimensional photonic lattices

All direct experimental observations of Bloch oscillations and Zener tunnelling performed so far were limited to so-called one-dimensional lattices [Feldmann92, Dahan96, Pertsch99a, Morandotti99, Sapienza03, Agarwal04, Ghulinyan05]. Hence, the samples were only periodic with respect to one transverse direction. New effects may also be associated with these phenomena in systems of higher dimensionality [Kolovsky03, Witthaut04]. In a two-dimensional periodic potential the wave follows complex Lissajous-type trajectories when the direction of the static force does not coincide with a principal axis of the lattice. Additionally, the process of Zener tunnelling becomes nontrivial as the band gap structure can cause an enhanced tunnelling in preferred directions determined by the lattices symmetries.

In this chapter the first experimental observation of Bloch oscillations and Zener tunnelling in two-dimensional (2D) periodic systems is reported.

A 2D lattice and a transverse refractive index ramp are optically induced into a photorefractive crystal [Efremis02, Fleischer03, Neshev03]. The propagation of a beam in the resulting structure shows Bloch oscillations and tunnelling from the first to higher-order transmission bands of the lattice band spectrum. The associated spectral dynamics are observed by measurements in Fourier space.

5.1. Optically induced index changes in photorefractive crystals

In the experiments on 2D Bloch oscillations and Zener tunnelling performed in this work the photorefractive effect is used to optically induce refractive index structures. For this reason a short introduction to this topic is given before presenting the experimental system. For more detailed information about photorefractive crystals various publications are available, as e.g. [Petrov91, Günter88].

If a photorefractive crystal is illuminated by light of certain wavelengths free charge carriers are generated, which are excited electrons and holes. The reason for this photo-excitation is the presence of impurity centres inside the band gap. These impurity centres serve as source of excited photoelectrons and also as electron trapping centres. An inhomogeneous illumination leads to an inhomogeneous charge carrier distribution inside the crystal. Free electrons and holes are generated in illuminated areas. These charges can move due to two different effects, namely diffusion and drift. For further considerations it has to be taken into account that the mobility of the excited electrons is much higher than the mobility of the holes.

In the diffusion model, the photo-excited electrons quickly diffuse from the illuminated region, where their concentration is higher, toward the dark regions, where their concentration is lower. There they become trapped. Because holes cannot follow so quickly, this results in an inhomogeneous charge distribution. In the dark regions the electrons create a negative charge, while the holes lead to a positive charge in the illuminated regions. The resulting inhomogeneous electric field distribution is transferred into a corresponding refractive index modulation via the electro-optic effect. However, as the strength of the refractive index modulation depends on the illumination intensity and the intrinsic parameters of the crystal only, it is hard to control in experiment.

Instead of the diffusion, we used the drift mechanism in order to create an index modulation. In contrast to the diffusion, the drift occurs only if an external electric field is applied to the crystal. In this case the excited electrons and holes are accelerated by the external field and move until the force created by the external field is compensated by the internal field, which is created by the resulting inhomogeneous charge distribution. The typical distance L_0 , which the electrons move, is called drift length and is proportional to the external field. The drift of the holes is neglected in the following, as their mobility is much smaller than for the electrons. In reality even with an external field always a combination of both effects exists, but in our case drift is much stronger than diffusion, so the latter is neglected.

Fig. 51 illustrates the situation in case of a cosine shaped illumination $I=I_0\cos(x/d)$. The excited electrons move inside the external field while the holes stay where they are generated.

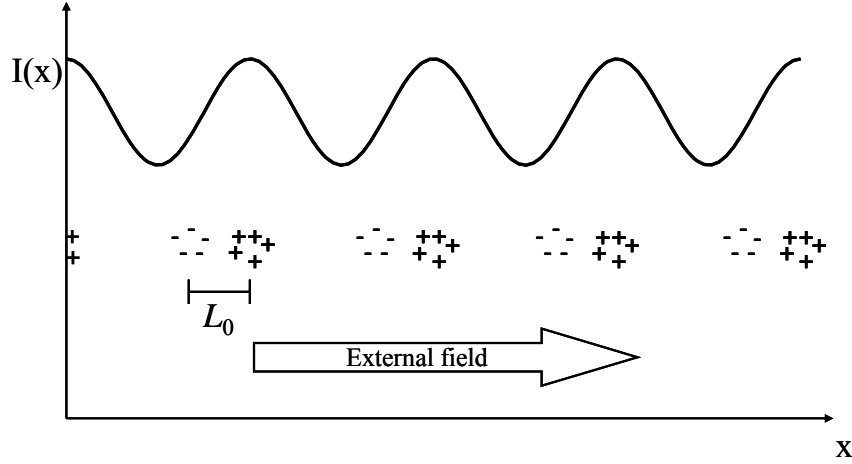


Fig. 51 An inhomogeneous intensity distribution $I(x)$ leads to an inhomogeneous charge distribution due to the motion of charges in an external field.

In the 1D case the inhomogeneous charge distribution leads to a periodic modulation of the electric field of the same period as the intensity of the illumination

$$\rho(x) = \rho_e \left[\cos\left(\frac{x}{d}\right) - \cos\left(\frac{x - L_0}{d}\right) \right]. \quad (100)$$

ρ_e includes the amount of excited electrons and depends on the illumination intensity I . d is the period of the cosine shaped illumination. The internal electric field E_{int} created by this charge distribution is determined by using $\text{div}(\epsilon_0 \epsilon E) = \rho$ and amounts to

$$E_{int}(x) = 2 \frac{d \rho_e}{\epsilon_0 \epsilon} \sin\left(\frac{L_0}{2d}\right) \cos\left(\frac{x - L_0/2}{d}\right), \quad (101)$$

with ϵ being the linear homogeneous dielectric number. For short drift length $L_0 \ll d$, the field can be approximated as

$$E_{int}(x) = \frac{\rho_e}{\epsilon_0 \epsilon} L_0 \cos\left(\frac{x - L_0/2}{d}\right), \quad (102)$$

with an amplitude that is independent of the period d . We obtain from the cosine shaped illumination a cosine shaped electric field, which is shifted by $L_0/2$ with respect to the illumination. As we assumed $L_0 \ll d$ this shift is neglected in the following. The drift length L_0 depends linear on the external field E_{ext} . Therefore also the induced electric field E_{int} evolves linearly with E_{ext} and can be controlled by the applied voltage.

Analogue to this 1D case an illumination which is periodic in both transverse directions can be used to create a field modulated in two dimensions.

To transfer the modulated electric field into a refractive index modulation the electro-optic effect is used. In order to make use of the largest electro-optic coefficient of the strontium barium niobate (SBN) crystal the external field and therefore also the internal field are oriented along the c-axis of the crystal, which corresponds to the x -direction in our notation. The induced refractive index change appears mainly for extraordinary (parallel to c-axis) polarized light. The index change for light which is ordinary (normal to c-axis) polarized is much smaller (\sim factor 20). We assume for the probe beam always extraordinary polarization. The refractive index change saturates for high illuminations to its maximum value. It can be written in a saturable model as

$$\Delta n(x, y) = \gamma \frac{I(x, y)}{I_d + I(x, y)}. \quad (103)$$

$I(x, y)$ is the intensity of the illumination and I_d the so-called dark intensity, including a homogeneous illumination that might exist additionally to the modulated intensity. γ is described by material parameters and the external field

$$\gamma = n_0 r_{eff} E_{ext}, \quad (104)$$

with the linear refractive index n_0 , the relevant effective electro-optic coefficient r_{eff} and the external field E_{ext} .

According to these equations the absolute refractive index change is directly proportional to the drift length and therefore to the external field, what gives us the possibility to control it easily via the applied voltage. Furthermore the induced refractive index change depends nonlinearly on the illumination, as it is of a saturable nature. If the illumination $I(x, y)$ is much weaker than the dark intensity I_d , the refractive index change Δn depends approximately linear on $I(x, y)$. With increasing intensity of the illumination the refractive index change saturates and converges to γ for $I(x, y) \gg I_d$.

So far we looked into a stationary regime, but in reality the described processes are slow. Therefore in experiment also the time dependence has to be taken into account, in order to work in a stationary regime. The speed of the processes depends strongly on the intensities, in particular on I_d . For very low intensities it takes a long time until a stationary regime is obtained, what makes it hard to perform reproducible experiments. This leads to further restrictions on the choice of the intensities.

5.2. Preparations

After introducing the basic effects in photorefractive crystals in the last section, in the following the preparations for experiments are presented together with the equations used in respective simulations.

An optical lattice is induced inside a strontium barium niobate (SBN) crystal by interfering four mutually coherent beams with ordinary polarization. To this end we use an amplitude mask with a diffraction grating, which is imaged by a $4f$ -system into the crystal, as shown in Fig. 52.

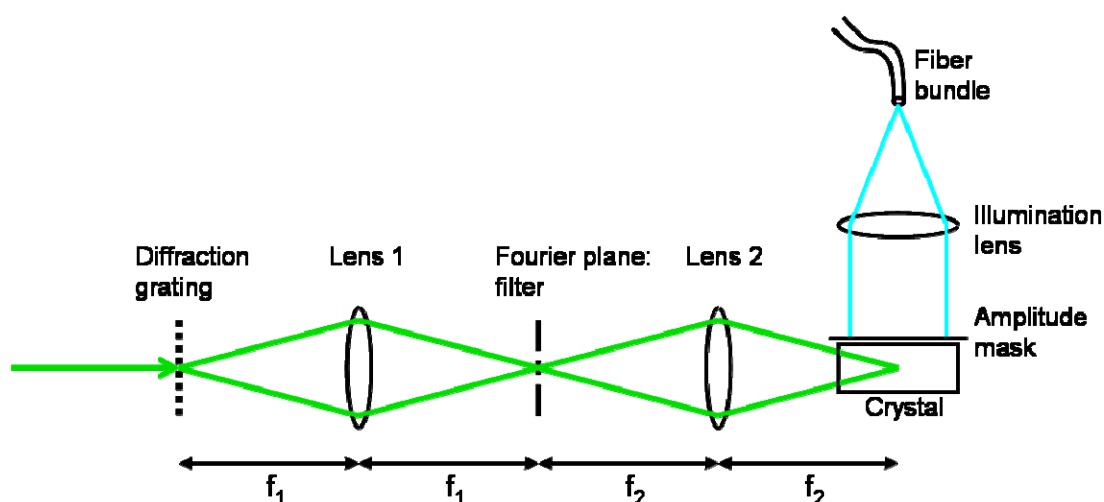


Fig. 52 Schematic representation of experimental setup to optically induce a lattice (green) and a refractive index gradient (blue).

The grating is illuminated by a laser beam. The respective diffraction pattern is found in the Fourier plane. There, an amplitude filter is placed in the optical path. It consists of a mask with four holes, letting pass only the first diffraction order. This ensures a cosine shape of the interference pattern inside the crystal instead of the step like pattern on the mask. The four beams of the first diffraction order are transformed into tilted waves by the second lens. In the crystal they interfere to a square lattice as shown in Fig. 53. The period of the lattice can be varied by the size of the diffraction pattern on the mask and the magnification of the imaging system.

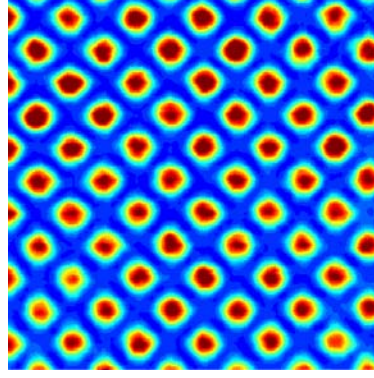


Fig. 53 Measured intensity pattern created by four coherently interfering beams with a lattice period of $d=20 \mu\text{m}$.

For our experiments the pattern is oriented with a tilt of 45° with respect to the principal axes of the resulting lattice in order to minimize effects of the anisotropy of the crystal [Desyatnikov05]. For numerical simulation the intensity distribution of the lattice is described by

$$I_g(x, y) = A \cos^2 \left[\frac{\pi(x+y)}{\sqrt{2}d} \right] \cos^2 \left[\frac{\pi(x-y)}{\sqrt{2}d} \right], \quad (105)$$

with the lattice period d and the amplitude A . Such a periodic light pattern induces a 2D modulation of the refractive index for the extraordinary polarized probe beam. We found that for this lattice orientation the influence of the anisotropy of the crystal on the induced index structure can be neglected. The ordinary polarized lattice beams remain stationary along the whole length of the crystal, as back feeding due to the index change is small for this polarization.

To test the quality of the lattice and to find out what experimental parameters to use, we first checked for discrete diffraction inside the induced lattice. Therefore we launched an extraordinary polarized probe beam having about the same size as the spots forming the lattice and hitting a single channel of increased refractive index at the entrance facet of the crystal. We observed its intensity distribution at the output facet of the crystal with a CCD-camera. We found that the lattice is very homogeneous as we were able to observe a diffraction pattern of a high symmetry for lattice periods of $10\mu\text{m}$ or larger. Fig. 54 shows an example of a diffraction pattern for such a lattice.

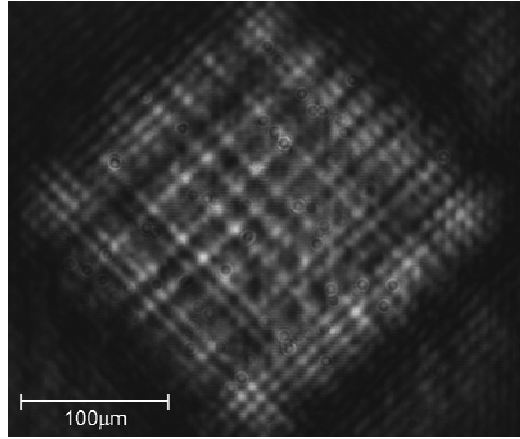


Fig. 54 Measured discrete diffraction in an optically induced 2D-lattice with a period of $d=10 \mu\text{m}$.

Next we investigated how to create the transverse refractive index gradient. Therefore, the crystal was illuminated from the top by a modulated incoherent white light beam (see Fig. 52). The modulation was achieved placing an amplitude mask on top of the crystal. This mask was illuminated by a fibre bundle. In order to collect the light from the fibres, a lens was placed above the amplitude mask. The measured intensity profile of the white light is shown in Fig. 55.

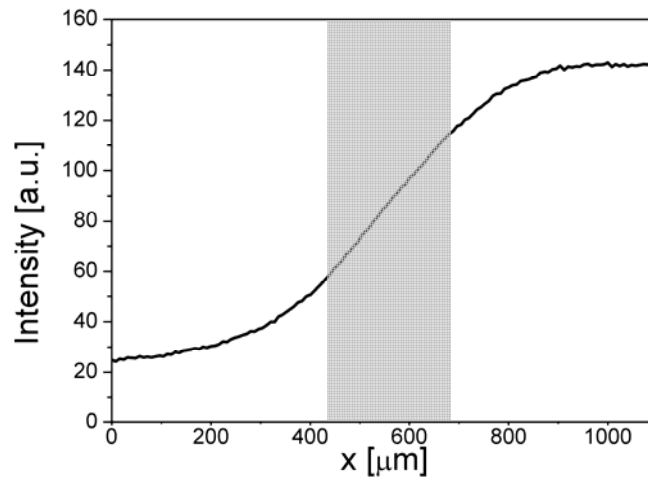


Fig. 55 Intensity distribution of white light illumination measured 3mm underneath the amplitude mask. For comparison: Shaded region illustrates width of area used in experiments.

For simulations it can be well approximated by

$$I_m(x) = B \left[1 + \tanh(x/\eta) \right] / 2, \quad (106)$$

where the parameter η determines the extend of the induced index gradient and B is the amplitude. In the centre of this gradient we find a region with approximately linear dependence. To test the performance of the induced gradient we launched a probe beam in the resulting structure without a superimposed lattice. Measuring the intensity at the output facet we found that the beam experiences a maximum transverse shift of $350\mu\text{m}$ when propagating in the gradient. To obtain this shift we had to apply an external field of $5000\text{V}/\text{cm}$.

After investigating both components, lattice and gradient, separately, the next task was to superimpose them. While it was straightforward to optimize the parameters for gradient and lattice separately, we found it quite hard to get both working at the same time. The reason for this is, that the parameters for a good lattice and a strong gradient are completely different.

To obtain a strong gradient, the white light intensity has to be varied in transverse direction in a wide range. In contrast to that, the lattice would need a medium white light intensity of constant level. Thus, the quality of the lattice is drastically reduced by the gradient. Furthermore we found that the existence of the lattice reduced the gradient, as the background level of light inside the crystal is increased. Even if obviously the amount of light inside the bright region is increased as well, the absolute refractive index contrast is still reduced as we work in a saturated regime on the bright side of the gradient. Hence we had to find a compromise for the different parameters, where we obtain a lattice and gradient of sufficient quality simultaneously. We found that the system works well if we use an external field of $5000\text{V}/\text{cm}$ and a lattice beam with a power of about $100\mu\text{W}$ and a diameter of 3.5mm . The amount of white light to induce the gradient was only slightly lower as in the experiments without a lattice.

To find the parameters for numerical simulations we compared results from experiment and simulation and tried to achieve agreement between both. We describe the total induced refractive index pattern by

$$\Delta n(x, y) = \gamma \frac{I_g(x, y) + I_m(x, y)}{I_d + I_g(x, y) + I_m(x, y)}. \quad (107)$$

The inhomogeneous illumination of the crystal I_m results in an inhomogeneous index distribution. A periodic structure is imposed onto a monotonically increasing background. For a finite region this leads to an almost liner increase of the background, as necessary for the observation of Bloch oscillations. Fig. 56 shows a cross section through the calculated refractive index profile at the position $y=0$.

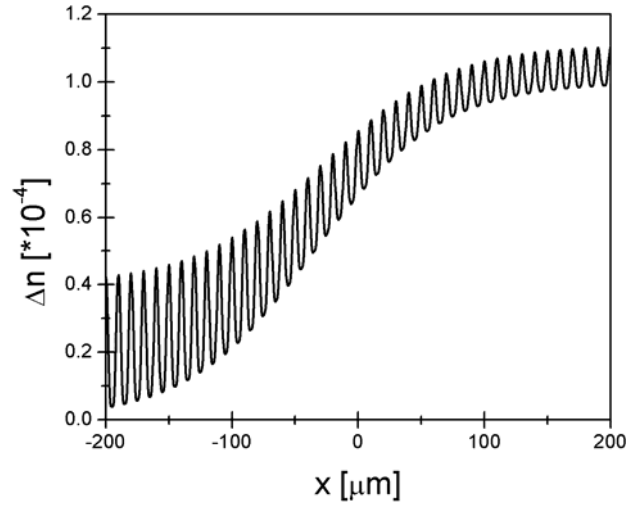


Fig. 56 Cross section through the calculated change of the refractive index inside the crystal at the position $y=0$ for $\gamma=2*10^{-4}$, $A/I_d=0.25$ and $B/I_d=1$.

Because of the saturable character of the photorefractive nonlinearity the contrast of the resulting index gradient varies across the crystal.

We simulated the propagation of an optical beam by solving the corresponding paraxial equation

$$i \frac{\partial E}{\partial z} + \frac{\lambda}{4\pi n_0} \left(\frac{\partial^2}{\partial x^2} + \frac{\partial^2}{\partial y^2} \right) E + \frac{2\pi}{\lambda} \Delta n(x, y) E = 0. \quad (108)$$

For the calculations we used the same parameters as in the experiments, which are the wavelength in vacuum $\lambda=532\text{nm}$, the refractive index $n_0=2.35$, the lattice period $d=20\mu\text{m}$ (measured along diagonal in Fig. 53) and the crystal length $L=23\text{mm}$. The intensities, the exact width of the gradient and the nonlinear coefficient were determined from comparison of theoretical and experimental results as follows: lattice amplitude normalized to dark intensity $A/I_d=0.25$, normalized gradient amplitude $B/I_d=0.25$, width of the gradient $\eta=300\mu\text{m}$, nonlinear coefficient $\gamma=2*10^{-4}$.

For a homogeneous lattice ($I_m=0$) the propagation of light is determined by Bloch waves, which have the form

$$E(x, y, z) = u(x, y) e^{i(k_x x + k_y y + \beta(k_x, k_y) z)},$$

with the Bloch vector $\mathbf{k}=(k_x, k_y)$. The band structure of the two-dimensional lattice describes the dependence of propagation constant β of the two components of the Bloch vector k_x and k_y . The first Brillouin zone is determined by the symmetry points of the lattice, which are depicted

in Fig. 57 (a). The three special points Γ , M and X correspond to $k_{x,\Gamma}=k_{y,\Gamma}=0$, $k_{x,M}=\sqrt{2} g/2$ and $k_{y,M}=0$ and to $k_{x,X}=k_{y,X}=g/(2*\sqrt{2})$ with $g=2\pi/d$. They determine the corners of the irreducible part of the first Brillouin zone. Usually the band structure has to be calculated inside the whole irreducible part of the Brillouin zone. However, essential information about the propagation of waves is already included in a scan through the band structure along the connections of the three symmetry points [Joannopoulos95], as it is depicted in Fig. 57 (b). For reasons of simplicity we often refer to this scan as band structure in the following. To calculate the band structure, again the program *MIT photonic bands* has been used [Johnson01]. As it was already shown for the band structure of a one-dimensional lattice, also here the band structure includes information about the propagation direction and diffraction properties. However, it has to be taken into account, that therefore usually the whole band structure instead of the scan is necessary. But due to symmetry reasons the scan still includes information about the group velocity of the respective Bloch waves. For these waves the Bloch vector has no component, which is orientend perpendicular to the path of the scan. At all three symmetry points the transverse velocity of the Bloch waves vanishes.

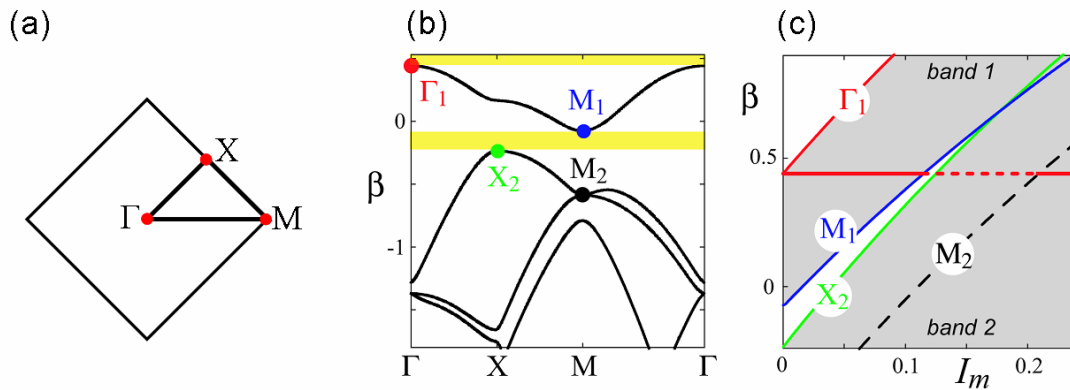


Fig. 57 (a) Symmetry points of the first Brillouin zone for a lattice as shown in Fig. 53, (b) calculated band structure of the lattice for $I_m=0$ and (c) band structure of the lattice vs. I_m . The horizontal line is the adiabatic value of the propagation constant. The dashed segment indicated Zener tunnelling through the gap.

Between the first and second band of the structure we obtain a band gap. The total gap is marked as a yellow region. Its width is narrower than the bands itself. However, the width of the local gap depends on the exact position in Fourier space. The local gap is largest at the Γ -point and decreases from there towards the X- and M-points of the lattice. Between these

points the gap width is almost constant. The small gap width at the M-point enables for a high tunnelling rate for our orientation of the gradient.

The superposition of the modulated illumination I_m results in a varying modulation depth of the lattice (see Fig. 56) due to saturation of the index change. Fig. 57 (c) shows how the band structure changes for increasing background illumination corresponding to the gradient in x -direction. We find that the total gap decreases and finally closes for high background illumination. The horizontal line in Fig. 56 (c) shows the value of the propagation constant for a wave packet that starts to propagate at the top of the first band in the low index region. Under the assumption that the propagation constant β is conserved, the wave packet follows this line while moving in x -direction in real space.

The dashed segment of the line indicates Zener tunnelling from the M-point at the bottom of the first band into the M-point of the second and third bands. For high values of I_m the total gap between first and second band vanishes. However, for Zener tunnelling the local gap (between the M-points of first and second band) is important. In Fig. 56 (c) we find this gap always open and almost independent of the gradient.

5.3. Results of simulations and experiments

In this section the propagation of a probe beam through an optical lattice with superimposed linear potential is discussed. For experiments the setup described in the last section was used. Results from numerical simulations and experiments are compared for different excitations and gradients.

Fig. 58 displays the calculated intensity distribution of a probe beam inside the optically induced lattice with a transversely superimposed gradient for different propagation distances. The parameters for this simulation are the same as determined in the last section. The width of the input beam is $37.5\mu\text{m}$ (full width half maximum-FWHM). White crosses mark the centres of the lattice maxima.

After propagating a distance of 18mm (Fig. 58 (a)) the beam is strongly modulated, indicating that neighbouring intensity maxima are out of phase. This occurs for a Bloch vector close to $k=\pi/d$ at the edge of the Brillouin zone. Intensity maxima of the left part of the beam are centred on the lattice maxima, indicating that the light is located inside the first band. In the right part of the beam intensity maxima lie in between lattice maxima and correspondingly this light can be assigned to higher order bands. Thus, the right part already has tunneled from the first to higher bands.

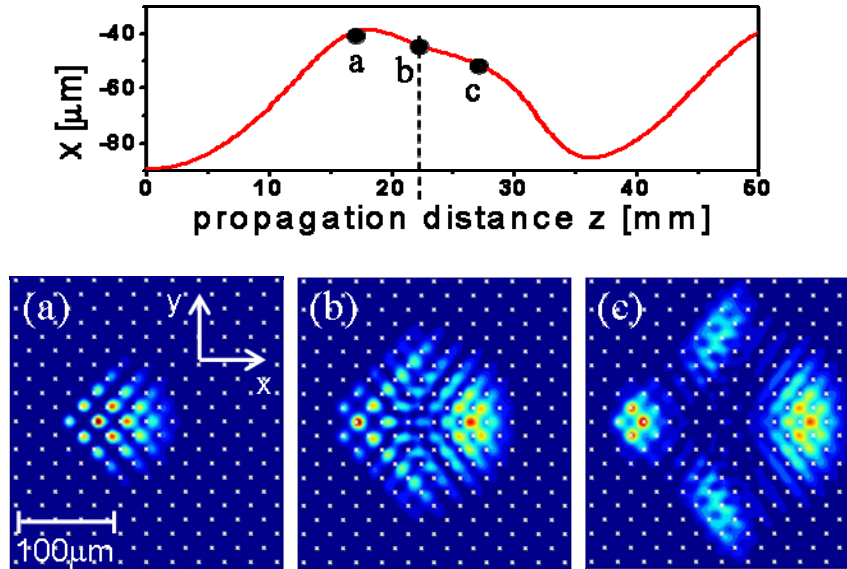


Fig. 58 Simulation of trajectory of the probe beam inside the first band and intensity distribution of the probe beam for propagation distance of (a) 18mm, (b) 23mm and (c) 28mm. The gradient is directed along x .

For longer propagation distances ((Fig. 58 (b) and (c)) the light inside different bands separates. Light inside the first band is Bragg reflected at the lattice and moves back into the opposite direction corresponding to Bloch oscillations inside the first band. Its trajectory is shown in the upper part of Fig. 58. Three other beams are located inside the second and third band. It can be seen from the band structure that these bands degenerate at the M-point. Therefore tunnelling from the first band occurs into the second and third band simultaneously. In real space one of the tunnelled beams moves further towards the right. The two other beams have tunnelled to another band and move up and down. Later they are accelerated by the gradient and thus gaining speed as well to the right. Now clearly the tunnelled beams have their intensity maxima located in between the lattice maxima, indicating that they belong to higher order bands.

In experiment we cannot monitor the evolution of light inside the crystal, but only observe the intensity at the crystal output. Thus, we have to follow a different strategy to obtain information about the evolution of the light during the propagation. We tilt the input beam to obtain an excitation with a linearly varying phase. With this excitation we are able to excite Bloch oscillations at different points of their trajectory. In order to check the validity of this assumption we calculated the trajectories for different angles. The results are depicted in Fig. 59. It can be clearly seen that the trajectory is shifted in propagation direction for an excitation with an input angle. Thereby a negative angle corresponds to an initial motion against the

gradient and vice versa. Besides a shift of the trajectory in propagation direction a shift in transverse direction occurs, leading to a small transverse shift of the output intensity distribution in the experiments.

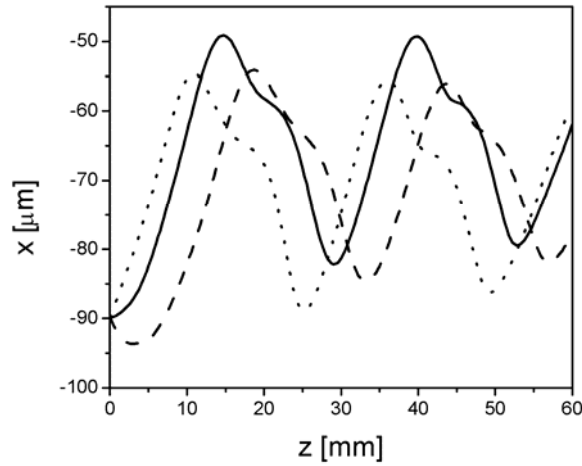


Fig. 59 Simulated Bloch trajectory for three different angles of input beam. Dashed line: -0.15° , solid line: 0.0° and dotted line: 0.15° tilt of input beam.

The measurements obtained with this technique are presented in Fig. 60. They show good qualitative agreement with the simulations. Only the tunnelling rate deviates slightly from the simulations. The lattice or gradient used in this experiment might have been stronger than the one used in simulations, leading to slightly higher reflection.

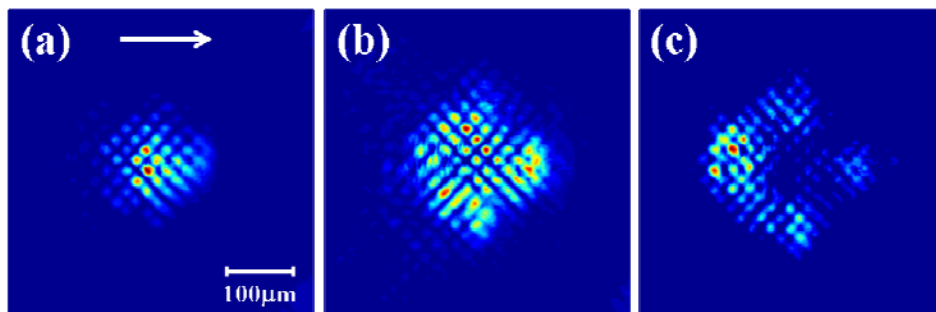


Fig. 60 Measured output intensity distribution for input angles of (a) -0.10° , (b) 0.00° and (c) 0.12° .

To understand better what happens during the tunnelling we performed another experiment, where not only the intensity distribution at the output but also the Fourier transform of the output field was observed [Bartal05]. Therefore an experimental setup as shown in Fig. 61 was used, where the Fourier plane (FT) of the imaging lens 1 at the crystal output is imaged by a

second lens (imaging lens 2) to a second CCD camera. This enables to take pictures from real and Fourier space simultaneously.

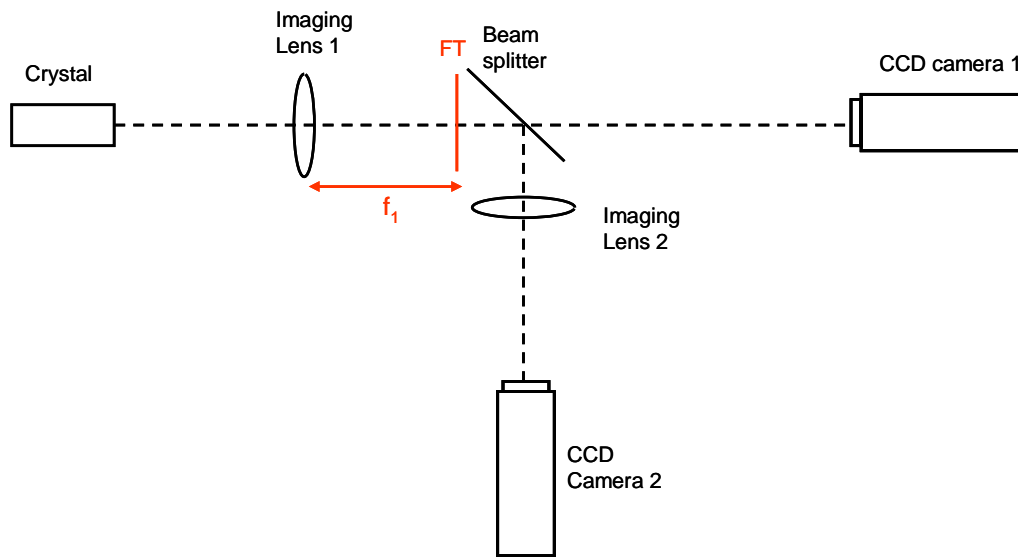


Fig. 61 Schematic representation of setup to detect simultaneously the intensity distribution and Fourier transform of the field at the output facet of the crystal.

In the images taken from Fourier space the first Brillouin zone is determined by the position of the four lattice beams (not shown), which define its corners. The results of the measurements are shown in Fig. 62.

For a negative angle of -0.10° we observe in real space a beam that is strongly modulated (Fig. 62 (a)). Between the intensity maxima the intensity decreases to zero. Hence we can infer that adjacent intensity maxima are out of phase, as it is the case at the edge of the Brillouin zone. This is confirmed by the picture from Fourier space, where we find the beam located at the M-point. Accordingly the measurement shows the intensity distribution at the centre of a Bloch period, where the elongation of the beam inside the first band is largest.

After a slight increase of the angle to -0.04° we took the next pictures (Fig. 62 (b)). While in real space still only one beam is visible, in Fourier space now three more beams appear, indicating tunnelling into higher bands. In real space we see this as an increase of the size of the beam corresponding to a beginning of the splitting into four beams. In Fourier space we find the beam inside the first band now appearing at the opposite side of the first Brillouin zone and moving again with the gradient. Three more beams are located close to the three other M-points of the first Brillouin zone.

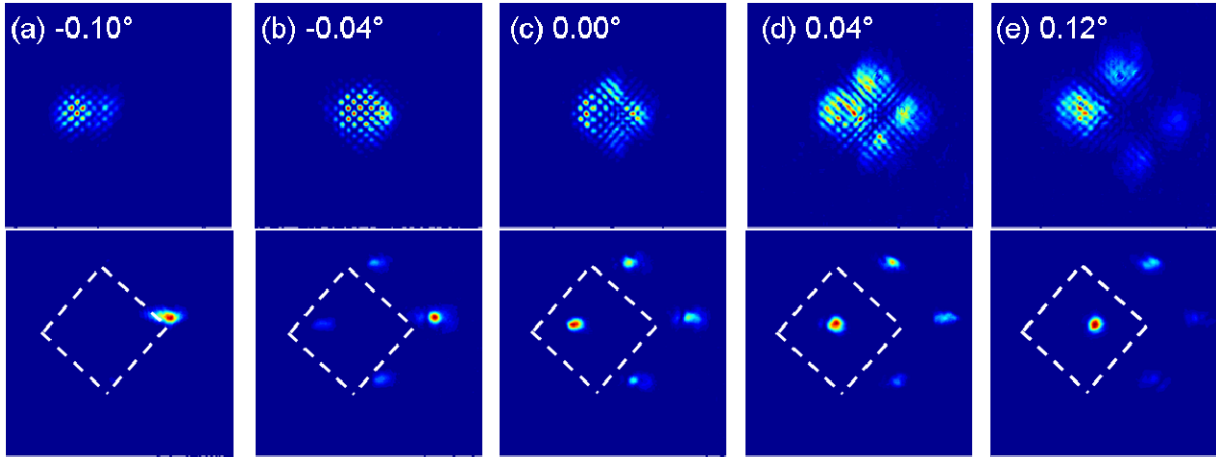


Fig. 62 Measurements of intensity distribution in real space (top) and Fourier space (bottom) after propagation through a 23mm long crystal with optically induced lattice and gradient. The angular tilt of the input beam is increased from (a) to (e) corresponding to measurements at larger propagation distance. The values of the input angle are shown in the top pictures. The white squares mark the first Brillouin zone.

We infer from this picture that light starts to tunnel, when the edge of the first Brillouin zone (M-point) is reached by the original beam. The tunnelled light couples from the first band into the M-point of higher bands and appears correspondingly at the M-points of the first Brillouin zone in the measurements. Due to the gradient it is again accelerated, as can be seen from Fig. 62 (c)-(e). The acceleration leads to a motion of the beams towards the right in the pictures from Fourier space. In real space the splitting into four beams becomes clearly visible, as the beams move away from each other. From the intensities inside the different beams, we can find that the described process does not occur instantaneously, but needs some propagation distance to happen. While in Fig. 62 (b) the original beam is still the strongest one, later one again the beam inside the first band becomes stronger than the tunnelled beams.

Besides experiments with a broad input beam we again performed experiments with a narrow beam exciting mainly one lattice maximum. Analogue to the experiments in planar waveguide arrays the Bloch oscillations are replaced by periodic diffraction and refocusing of the beam. As Bloch waves with all Bloch vectors k are excited by a narrow beam, Zener tunnelling is expected to appear continuously during the propagation, because there are always components which propagate in the vicinity of the band edge. To observe this effect we used a tightly focused signal beam which was launched into the crystal directly on one of the lattice maxima. As we cannot use the technique to tilt the input angle for narrow excitation, we recorded the

light intensity distribution at the exit facet of the crystal varying the strength of the transverse index gradient instead. In simulations this was achieved by changing the width of the tanh-function η (cp. eq. (106)). In Fig. 63 results of simulations for three different cases are presented. Except for the gradient, the parameters are the same as for the simulations with excitation by a broad beam. In (a) to (c) the propagation in a homogeneous lattice is demonstrated. The pictures show the intensity distribution after (a) 18mm, (b) 23mm and (c) 28mm propagation distance. We observe a typical discrete diffraction pattern.

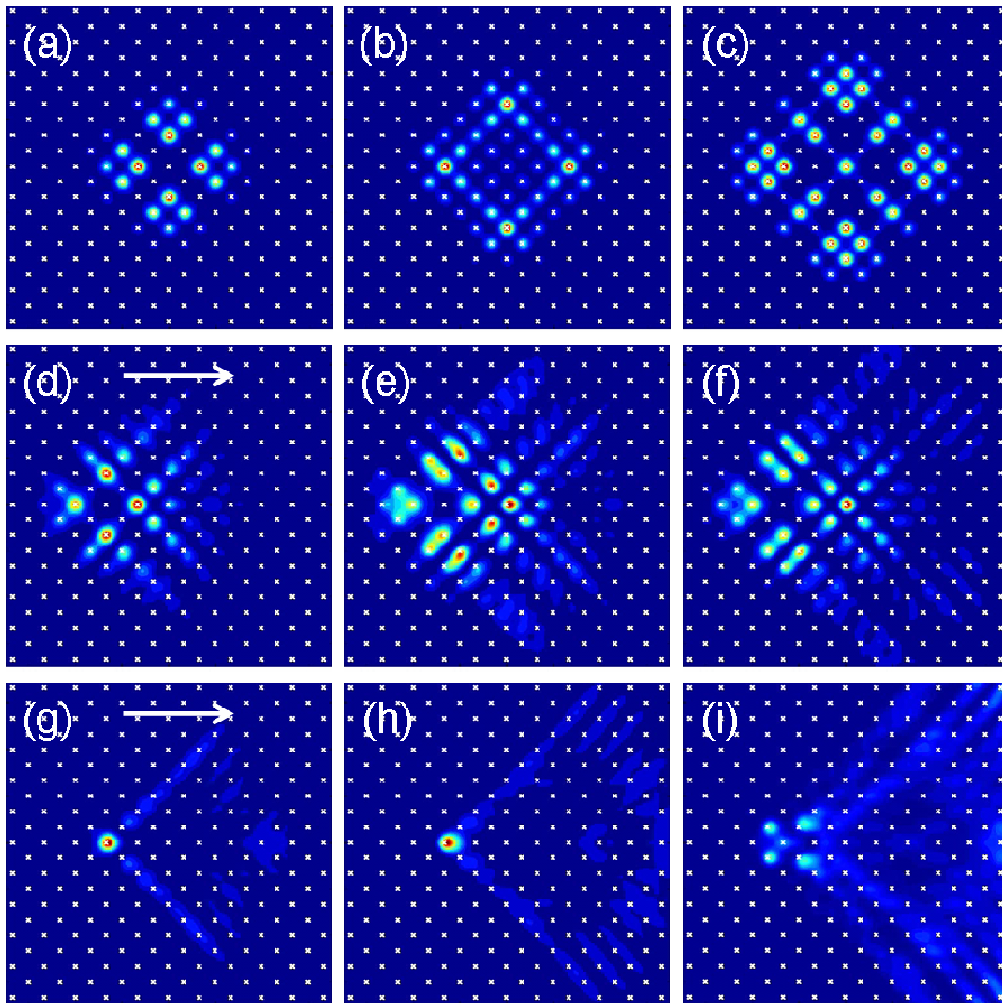


Fig. 63 Simulated propagation with excitation of a single waveguide in (a-c) a homogeneous lattice, (d-e) a weak and (g-i) a strong index gradient. Intensity distributions are shown after propagation distance of (a,d,g) 18mm, (b,e,h) 23mm and (c,f,i) 28mm. Arrows show direction of gradient.

Fig. 63 (d)-(f) show the propagation, if a weak gradient with $\eta=166\mu\text{m}$ is superimposed onto the lattice. Due to the gradient the beam starts to diffract asymmetrically while a part of the intensity is radiated into higher order bands (see Fig. 63 (d)). For a longer propagation distance

the beam first continues to diffract (Fig. 63 (e)), but then starts to refocus (Fig. 63 (f)). Radiation appears as expected continuously during propagation. A completely different behaviour can be observed for propagation inside a strong gradient. The stronger gradient was achieved by decreasing the width of the gradient to $\eta=66\mu\text{m}$. Analyzing Fig. 63 (g) and (h) the excited waveguide seems almost to decouple from the array, as the main part of the light is trapped in the excited guide. As before, also here radiation to higher order bands can be observed continuously. However, for longer propagation distance of 23mm (Fig. 63 (i)) this picture does not hold anymore. The light does not stay inside the excited guide but diffracts. We found that for such a gradient as used here, Bloch oscillations are destroyed as the gradient varies inside the area where the beam propagates. Thus the conditions for Bloch oscillations are not given anymore.

Additional to the simulations we again performed experiments. The results are presented in Fig. 64. Fig. 64 (a) shows the discrete diffraction of a narrow beam in the lattice with no superimposed index gradient. The spatial symmetry of the field distribution is almost perfect, which reflects the good symmetry of the lattice.

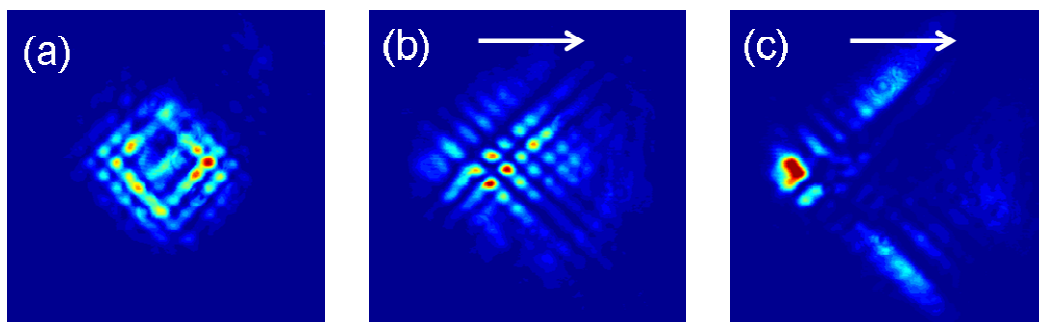


Fig. 64 Measured light intensity profiles at the crystal output for excitation of a single site. (a) Discrete diffraction with no background modulation, propagation in (b) weak and (c) strong index gradient.

In the case of a rather weak gradient (Fig. 64 (b)) the light has approximately travelled two thirds of a Bloch period before reaching the end of the crystal. The central part of the beam starts to refocus again while some light already tunnelled to the second band. Although no pronounced spatial separation of the light in the first and second bands has occurred so far, the induced asymmetry of the field distribution is a clear indication that tunnelling has taken place. To obtain a stronger gradient as in Fig. 64 (b) we observed propagation in an area close to the top of the crystal and thus as well close to the mask. In contrast to before, where the beam

propagated about 3mm under the mask, we were then only 1mm away from it. As can be seen in Fig. 64 (c), almost no breathing is visible and the light in the first band is confined to the input waveguide and its direct neighbours. The gradient is so strong that light cannot escape from this area as it is immediately Bragg or total reflected at the surrounding. Now, the tunnelled light appears as radiation along the Γ -X-directions of the lattice. Note that only the light inside higher bands follows the action of the gradient by performing a transverse motion and thus breaking the symmetry. The experimental results again are in excellent agreement with the simulations.

Concluding this chapter, we were able to perform the first experimental demonstration of two-dimensional Bloch oscillations and Zener tunnelling. To this end we investigated the propagation of a light beam in a 2D optically-induced lattice with a superimposed transverse gradient. For broad excitation tunnelling appeared as a splitting of the beam into four parts, three of them propagating in higher order bands. Our measurements in Fourier space gave clear evidence that Bloch oscillations in the first band correspond to a motion through the first Brillouin zone, as it was predicted already by Zener [Zener34]. When the light beam reaches the edge of the Brillouin zone, it jumps to the other side and keeps moving in the same direction afterwards. Simultaneously Zener tunnelling occurs and three tunnelled beams appear at the M-points. In contrast to the oscillatory motion of a broad beam, for excitation of a single lattice site periodical diffraction and refocusing of the beam was observed. In this case tunnelling appears continuously during propagation.

6. Conclusions

The dynamics in discrete or periodical systems under the influence of a perturbation is a subject of active research in various branches of physics. Examples are investigations of electrons in semiconductor superlattices [Esaki70, Mendez88, Feldmann92], ultra-cold atoms in accelerated optical lattices [Dahan96] and photons in photonic lattices [Pertsch99a, Morandotti99, Sapienza03, Argawal04]. The subject of this thesis is the theoretical and experimental investigation of the propagation of light waves in inhomogeneous waveguide arrays.

Defects and interfaces were introduced into waveguide arrays by varying the width or spacing of the waveguides. The existence of localized states at defects in otherwise homogeneous arrays has been analytically predicted and experimentally confirmed. To induce a defect the propagation constant of one guide and the corresponding coupling constants have been varied with respect to the homogeneous array. The observed intensity patterns at the output facet of the arrays gave clear evidence of the existence of defect modes. Both an increase of the coupling constant as well as the variation of the effective index gave rise to the formation of localized states. Depending on the parameters a staggered mode, an unstaggered mode or both could exist. Furthermore it turned out that symmetric defects even if they are multimode cannot support antisymmetric modes. Defects, which do not support a bound state, were found to be repulsive. Excellent agreement was achieved between the theoretical predictions and the experimental verification.

To demonstrate an application of defects in waveguide arrays, an electro-optical switch was designed, which could act either as an on-off-switch or as a Y-branch with a controllable split-ratio.

In a next step the optical properties of interfaces between two distinct arrays were investigated on the basis of a coupled mode theory. For certain parameters bound states were found to exist, which have no analogon at interfaces in bulk media. Furthermore, analytical expressions for the reflection and transmissions coefficients of Bloch waves at interfaces were derived and interpreted by means of the band structure.

Photonic Zener tunnelling has been studied in planar and two-dimensional waveguide arrays. While this effect was originally predicted for electrons in crystals, we demonstrated that it can also happen to photons, which move in a periodic structure with a superimposed index gradient. An analytical expression for the tunnelling rate was derived analogous to the tunnelling rate for electrons presented in [Zener34, Holthaus00]. The experimental demonstration of Zener tunnelling in planar arrays was performed in polymer waveguides. To this end a new setup has been developed, which enables to directly observe the propagation inside the arrays by detecting the fluorescence. With this system we observed damped Bloch oscillations, which were accompanied by Zener tunnelling. The latter one appeared as regular outbursts of radiation into higher order bands. This is the first direct visualization of Zener tunnelling.

For the excitation by a narrow beam the Bloch oscillations appeared as periodic de- and refocusing. In this case Zener tunnelling was found to appear continuously. If additionally to the first band cladding modes were excited by a broad beam the interaction became more complex, as Bloch oscillations in different bands were observed simultaneously. Furthermore coupling between higher order bands could be observed as additional radiation. All measurements were in perfect qualitative agreement with numerical simulations.

While so far Bloch oscillations and Zener tunnelling were restricted to one-dimensional systems, first observations of these effects in two-dimensional lattices were presented in this work. For this purpose both, the two-dimensional periodic structure and the refractive index gradient were optically induced into a photorefractive crystal. The propagation of light in the resulting structure was analyzed by BPM simulations and measurements. We were able to observe an initial state of Bloch oscillations from up to one period. These oscillations were accompanied by Zener tunnelling to higher order bands. For the first time the motion of a beam through the first Brillouin zone corresponding to Bloch oscillations in real space was directly detected in Fourier space. Zener tunnelling appeared as radiation into three different directions in real space. In Fourier space tunnelling into three different symmetry points of the lattice was observed. The propagation of the three corresponding beams outside the first Brillouin zone gave clear evidence that this light belongs to higher order bands. The presented measurements gave the first evidence of Bloch oscillations and Zener tunnelling in a two-dimensional system.

For a continuation of the research presented in this work, different interesting tasks can be imagined. While the experimental verification of bound states at defects was already presented in this work, it should be also possible to observe bound states at interfaces. Furthermore so far no measurements on reflection and transmission at defects and interfaces in planar waveguide arrays were performed.

Bloch oscillations and Zener tunnelling still are a hot topic of research. While in this work first direct observations of photonic Zener tunnelling in one and two dimensions were presented, it is worth to investigate these effects more precisely. In a two-dimensional lattice Bloch oscillations and Zener tunnelling were presented only for one particular orientation of the gradient with respect to the lattice. However, it was shown theoretically that for gradients, which are not oriented along the symmetry axes of the lattice Lissajous-like trajectories can be expected [Pertsch99b, Kolovsky03, Witthaut04]. Furthermore also the phenomenon of Zener tunnelling becomes more complex in this case, as it does not necessarily appear at the symmetry points anymore. Therefore I think it is worth to investigate systems which enable for the observation of these effects.

As in this work only qualitative results on Zener tunnelling were presented, also quantitative investigations on the tunnelling rate should follow. The tunnelling rate has been a controversially discussed subject of research during the last years (see e.g. [Glutsch04] and references therein). It would be worth to study experimentally the dependence of the tunnelling rate on the system parameters, in particular on the refractive index gradient, and compare it with the different theoretical predictions.

Besides a straight forward continuation of this work, also the transfer of other quantum mechanical effects to optical systems would be worthwhile to study. For example, publications can be found, which suggest the demonstration of optical analogies to Fano resonances [Miroshnichenko05], quantum tunnelling [Longhi05a] and dynamic localization of electrons in an alternating electric field [Longhi05b].

7. Bibliography

References

[Agarwal04] V. Agarwal, J.A. del Rio, G. Malpuech, M. Zamfirescu, A. Kavokin, D. Coquillat, D. Scalbert, M. Vladimirova, and B. Gil, “Photon Bloch oscillations in porous silicon optical superlattices,” *Phys. Rev. Lett.* **92**, 097401 (2004)

[Bartal05] G. Bartal, O.Cohen, H. Buljan, J. W. Fleischer, O. Manela, and M. Segev, „Brillouin zone spectroscopy of nonlinear photonic lattices,“ *Phys. Rev. Lett.* **94**, 163902 (2005)

[Birks97] T. A. Birks, J. C. Knight and P. St. J. Russell, “Endlessly single-mode photonic crystal fiber ,” *Opt. Lett.* **22**, 961-963 (1997).

[Bloch28] F. Bloch, “Über die Quantenmechanik der Elektronen in Kristallgittern,” *Z. Phys.* **52**, 555-600 (1928).

[Börner90] M. Börner, R. Müller, R.Schiek and G. Trommer, “Elemente der integrierten Optik,” Teubner Studienbücher (1990)

[Bourlon04] B. Bourlon, D.C. Glatli, B. Placais, J.M. Berroir, C. Miko, L. Forro, and A.Bachtold, “Geometrical dependence of high-bias current in multiwalled Carbon nanotubes, ” *Phys. Rev. Lett.* **92**, 026804 (2004).

[Crank75] J. Crank, “The mathematics of diffusion,” Oxford university press, New York (1975)

[Dahan96] M. B. Dahan, E. Peik, J. Reichel, Y. Castin, and C. Salomon, “Bloch oscillations of atoms in an optical potential,” *Phys. Rev. Lett.* **76**, 4508-4511 (1996).

[Darmanyany98] S. Darmanyany, A. Kobayakov, E. Schmidt, and F. Lederer, “Strongly localized vectorial modes in nonlinear waveguide arrays,” *Phys. Rev. E* **57**, 3520-3530 (1998)

- [Desyatnikov05]** A.S. Desyatnikov, D.N. Neshev, Yu.S. Kivshar, N. Sagemerten, D. Träger, J. Jaegers, C. Denz and Ya.V. Kartashov, “Nonlinear photonic lattices in anisotropic nonlocal self-focusin media,” *Opt. Lett.* **30**, 869-871 (2005)
- [Droulias05]** S. Droulias, K. Hizanidis, D. N. Cristodoulides, and R. Morandotti, “Waveguide array-grating compressors,” *Appl. Phys. Lett.* **87**, 131104 (2005)
- [Efremidis02]** N. K. Efremidis, S. Sears, D. N. Christodoulides, J. W. Fleischer and M. Segev, “Discrete solitons in photorefractive optically induced photonic lattices,” *Phys. Rev. Lett. E* **66**, 046602 (2002)
- [Eisenberg98]** H. S. Eisenberg, Y. Silberberg, R. Morandotti, A. R. Boyd, and J. S. Aitchison, „Discrete spatial optical solitons in waveguide arrays,“ *Phys. Rev. Lett.* **81**, 3383-3386 (1998)
- [Esaki70]** L. Esaki and R. Tsu, “Superlattice and negative differential conductivity in semiconductors,” *IBM J. Res. Dev.* **14**, 61 (1970).
- [Esaki74]** L. Esaki, “Long journey into tunnelling,” *Rev. Mod. Phys.* **46**, 237–244 (1974).
- [Feldmann92]** J. Feldmann, K. Leo, J. Shah, D. A. B. Miller, J. E. Cunningham, T. Meier, G. von Plessen, A. Schulze, P. Thomas, and S. Schmitt–Rink, “Optical investigation of Bloch oscillations in a semiconductor superlattice,” *Phys. Rev. B* **46**, 7252-7255 (1992).
- [Fleischer03]** J.W. Fleischer, M. Segev, N. K. Efremidis, and D. N. Christodoulides, “Observation of two-dimensional discrete solitons in optically induced nonlinear photonic lattices,” *Nature* **422**, 147-150 (2003)
- [Freymanna03]** G. von Freymanna, W. Koch, D. C. Meisel and M. Wegener, “Diffraction properties of two-dimensional photonic crystals,” *Appl. Phys. Lett.* **83**, 614-616 (2003).
- [Ghulinyan05]** M. Ghulinyan, C. J. Oton, Z. Gaburro, and L. Pavesi, “Zener Tunnelling of LightWaves in an Optical Superlattice,” *Phys. Rev. Lett.* **94**, 127401 (2005)
- [Glutsch04]** S. Glutsch, “Excitons in low-dimensional semiconductors,” Springer-Verlag Berlin Heidelberg (2004)
- [Günter88]** P. Günter and J.-P. Huignard (editors), “Photorefractive materials and their application I,” Springer-Verlag Berlin Heidelberg (1988)
- [Hocker77]** G.B. Hocker, and W.K. Burns, “Mode dispersion in diffused channel waveguides by the effective index method,” *Appl. Opt.* **16**, 113-118 (1977)

- [Holthaus00]** M. Holthaus, “Bloch oscillations and Zener breakdown in an optical lattice,” *J. Opt. B: Quantum Semiclass. Opt.* **2**, 589-604 (2000).
- [Houbertz03]** R. Houbertz, G. Domann, C. Cronauer, A. Schmitt, H. Martin, J.-U. Park, L. Fröhlich, R. Buestrich, M. Popall, U. Streppel, P. Dannberg, C. Wächter and A. Bräuer, “Inorganic-organic hybrid materials for application in optical devices,” *Thin Solid Films* **422**, 194-200 (2003)
- [Ithier05]** G. Ithier, E. Collin, P. Joyez, D. Vion, D. Esteve, J. Ankerhold, and H. Grabert, “Zener Enhancement of Quantum Tunnelling in a Two-Level Superconducting Circuit”, *Phys. Rev. Lett.* **94**, 057004 (2005)
- [Jin91]** H. Jin, M. Belanger, and Z. Jacubczyk, „General analysis of electrodes in integrated-optics and electrooptic devices,“ *J. Quant. Electron.* **27**, 243-251 (1991)
- [Joannopoulos95]** J. D. Joannopoulos, R. D. Meade, and J. N. Winn “Photonic Crystals: Molding the flow of light,” Princeton University Press, Princeton (1995)
- [Johnson01]** S. G. Johnson and J. D. Joannopoulos, "Block-iterative frequency-domain methods for Maxwell's equations in a planewave basis," *Optics Express* **8**, 173-190 (2001)
- [Jones65]** A. L. Jones, “Coupling of optical fibers and scattering in fibers,” *J. Opt. Soc. Am.* **55**, 261-271 (1965)
- [Karthe91]** W. Karthe, and R. Müller, “Integrierte Optik,” Akademische Verlagsgesellschaft Geest und portig, Leipzig (1991)
- [Kirejew74]** P. S. Kirejew, „Physik der Halbleiter,“ Akademie-Verlag, Berlin (1974)
- [Knight03]** J. C. Knight, T. A. Birks, R. F. Cregan, P. ST. J. Russell, and J.-P. de Sandro, “Large Mode Area Photonic Crystal Fiber,” *Electron. Lett.* **34**, 1347-1348 (1998).
- [Kolovsky03]** A. R. Kolovsky, and H. J. Korsch, “Bloch oscillations of cold atoms in two-dimensional optical lattices,” *Phys. Rev. A* **67**, 063601 (2003)
- [Landau67]** L.D. Landau and E.M. Lifschitz, “Lehrbuch der theoretischen Physik,” Band 3, Akademie-Verlag Berlin (1967)
- [Longhi05a]** S. Longhi, “Coherent destruction of tunnelling in waveguide directional couplers,“ *Phys. Rev. A* **71**, 065801 (2005)

[Longhi05b] S. Longhi, “Self-imaging and modulational instability in an array of periodically curved waveguides,” *Opt. Lett.* **30**, 2137-2139 (2005)

[Mendez88] E. E. Mendez, F. Agullo-Rueda, and J. M. Hong, “Stark Localization in GaAs-GaAlAs Superlattices under an Electric Field,” *Phys. Rev. Lett.* **60**, 2426-2429 (1988).

[Miroshnichenko05] A. E. Miroshnichenko, Y. S. Kivshar, R. A. Vicencio, and M. I. Molina, “Fano resonance in quadratic waveguide arrays,” *Opt. Lett.* **30**, 872-874 (2005)

[Mogilevtsev98] D. Mogilevtsev, T. A. Birks and P. St. J. Russell, “Group-velocity dispersion in photonic crystal fibers,” *Opt. Lett.* **23**, 1662-1664 (1998).

[Morandotti99] R. Morandotti, U. Peschel, J. S. Aitchison, H. S. Eisenberg, and Y. Silberberg, “Experimental observation of linear and nonlinear optical Bloch oscillations,” *Phys. Rev. Lett.* **83**, 4756-4759 (1999).

[Morandotti03] R. Morandotti, H. S. Eisenberg, D. Mandelik, Y. Silberberg, D. Modotto, M. Sorel, C. R. Stanley and J. S. Aitchison, “Interactions of discrete solitons with structural defects,” *Opt. Lett.* **28**, 834-836 (2003).

[Neshev03] D. Neshev, E. Ostrovskaya, Y. Kivshar, and W. Krolikowski, “Spatial solitons in optically induced gratings,” *Opt. Lett.* **28**, 710-712 (2003)

[Notomi00] M. Notomi, “Theory of light propagation in strongly modulated photonic crystals: Refractionlike behavior in the vicinity of the photonic band gap,” *Phys. Rev. B* **62**, 10696-10705 (2000).

[Paulsen95] C. Paulsen and J.-G. Park; M. A. Novak and R. Sessoli, in *Quantum Tunnelling of Magnetization*, edited by L. Gunther and B. Barbara, Kluwer, Dordrecht, 1995

[Pendry03] Focus Issue: “Negative Refraction and Metamaterials,” ed. by J.B. Pendry, *Opt. Express* **11**, 639 (2003).

[Pertsch99a] T. Pertsch, P. Dannberg, W. Elflein, A. Bräuer, and F. Lederer, “Optical Bloch oscillations in temperature tuned waveguide arrays,” *Phys. Rev. Lett.* **83**, 4752-4755 (1999).

[Pertsch99b] T. Pertsch, U. Peschel, and F. Lederer, “Bloch oscillations in two dimensional lattices,” in *Quantum Electronics and Laser Science Conference*, OSA Technical Digest (Optical Society of America, Washington DC, 1999), p. 208.

- [Pertsch02]** T. Pertsch, T. Zentgraf, U. Peschel, A. Bräuer and F. Lederer, “Anomalous Refraction and Diffraction in Discrete Optical Systems,” *Phys. Rev. Lett.* **88**, 093901-093904 (2002).
- [Pertsch04]** T. Pertsch, U. Peschel, F. Lederer, J. Burghoff, M. Will, S. Nolte, and A. Tünnermann, “Discrete diffraction in two-dimensional arrays of coupled waveguides in silica”, *Opt. Lett.* **29**, 468-470 (2004)
- [Peschel98]** U. Peschel, T. Pertsch and F. Lederer, “Optical Bloch oscillations in waveguide arrays,” *Opt. Lett.* **23**, 1701-1703 (1998)
- [Peschel99]** U. Peschel, R. Morandotti, J. S. Aitchison, H. S. Eisenberg and Y. Silberberg, “Nonlinearly induced escape from a defect state,” *Appl. Phys. Lett.* **75**, 1384-1386 (1999).
- [Petrov91]** M. P. Petrov, S. I. Stepanov and A.V. Khomenko, “Photorefractive crystals in coherent optical systems,” Springer-Verlag Berlin Heidelberg (1991)
- [Roey81]** J. Van Roey, J. van der Donk and P.E. Lagasse, “Beam-propagation method: analysis and assesment,” *J. Opt. Soc. Am.* **71** (1981)
- [Rosam01]** B. Rosam, D. Meinhold, F. Löser, V. G. Lyssenko, S. Glutsch, F. Bechstedt, F. Rossi, K. Köhler, and K. Leo, " Field-Induced Delocalization and Zener Breakdown in Semiconductor Superlattices", *Phys. Rev. Lett.* **86**, 1307-1310 (2001)
- [Russel03]** P Russell, “Photonic Crystal Fibers,” *Science* **299**, 358-363 (2003).
- [Sapienza03]** R. Sapienza, P. Costantino, D. Wiersma, M. Ghulinyan, C. J. Oton, and L. Pavesiprl, “Optical Analogue of Electronic Bloch Oscillations,” *Phys. Rev. Lett.* **91** 263902 (2003).
- [Sibille98]** A. Sibille, J. F. Palmier, and F. Laruelle, “Zener interminiband resonant breakdown in superlattices,” *Phys. Rev. Lett.* **80**, 4506-4509 (1998).
- [Somekh73]** S. Somekh, E. Garmire, A. Yariv, H. L. Garvin and R. G. Hunsperger, “Channel optical waveguide directional couplers,” *Appl. Phys. Lett.* **22**, 46-48 (1973).
- [Somekh73]** S. Somekh, E. Garmire, A. Yariv, H.L. Garvin and R.G. Hunsperger, “Channel optical waveguide directional couplers,” *Appl. Phys. Lett.* **22**, 46-48 (1973).

[Strake88] E. Strake, G.P. Bava, and I. Montrosset, "Modes of a channel waveguide: A novel quasi-analytical technique in comparison with scalar finite-element method," *J. Ligth. Technol.* **6**, 1126-1135 (1988)

[Streppel02] U. Streppel, P. Dannberg, C. Wächter, A. Bräuer, L. Fröhlich, R. Houbertz and M. Popall, "New wafer-scale fabrication method for stacked optical waveguide interconnects and 3D micro-optic structures using photo-responsive (inorganic-organic hybrid) polymers," *Opt. Mat.* **21**, 475-483 (2002).

[Wannier60] G. H. Wannier, "Wave functions and effective Hamiltonian for Bloch electrons in an electric field," *Phys. Rev.* **117**, 432-439 (1960).

[Witthaut04] D. Witthaut, F. Keck, H. J. Korsch, and S. Mossmann, "Bloch oscillations in two-dimensional lattices," *New J. Phys.* **6**, 41 (2004)

[Yellin95] j. Yellin, "Two exact lattice propagators," *Phys. Rev. E* **52**, 2208-2215 (1995)

[Zener34] C. Zener, "A theory of the electrical breakdown of solid dielectrics," *Proc. R. Soc. London Ser. A* **145**, 523-529 (1934).

List of publications

[T03] H. Trompeter, U. Peschel, T. Pertsch, F. Lederer, U. Streppel, D. Michaelis, and A. Bräuer, „Tailoring guided modes in waveguide arrays,“ *Opt. Express* **11**, 3403-3411 (2003)

[T04] H. Trompeter, U. Peschel, T. Pertsch, F. Lederer, U. Streppel, D. Michaelis, and A. Bräuer, „Tailoring defect modes in waveguide arrays,“ *Conference on Lasers and Electro Optics 2004 (CLEO), OSA Technical Digest, paper CThCC4* (2004).

[T05a] H. Trompeter, U. Streppel, D. Michaelis, A. Bräuer, U. Peschel, T. Pertsch, and F. Lederer, "Experimental and theoretical investigations on localized states in waveguide arrays," *Proc. SPIE* **5728**, 44-53 (2005)

[T05b] U. Streppel, D. Michaelis, A. Bräuer, H. Trompeter, U. Peschel, T. Pertsch, and F. Lederer, „Experimental and theoretical investigations in inhomogeneous polymer waveguide arrays,“ *International Conference on Frontiers of polymers and Advanced Materials (ICFPAM), Cancun, Mexico, 234, invited, 22.-28.4* (2005)

[T05c] H. Trompeter, D. Michaelis, U. Streppel, U. Peschel, T. Pertsch, A. Bräuer, and F. Lederer, “Inhomogeneous waveguide arrays,” Proc. 12th European Conference on Integrated Optics (ECIO), 100-103 (2005)

[T05d] H. Trompeter, U. Peschel, T. Pertsch, F. Lederer, D. Michaelis, U. Streppel, and A. Bräuer, „Photonic Zener tunnelling,“ in Quantum Electronics and Laser Science Conference (QELS) 2005, OSA Technical Digest, paper QFA2 (2005)

[T05e] H. Trompeter, W. Krolikowski, D. Neshev, A.S. Desyatnikov, A.A. Sukhorukov, Y. Kivshar, T. Pertsch, U. Peschel, and F. Lederer, “Optical Bloch oscillations and Zener tunnelling in two-dimensional photonic lattices,” Photonic Crystals: Fundamentals to Devices, Sydney Australia (2005)

[T05f] H. Trompeter, W. Krolikowski, D. Neshev, A.S. Desyatnikov, A.A. Sukhorukov, Y. Kivshar, T. Pertsch, U. Peschel, and F. Lederer, “Optical Bloch oscillations and Zener tunnelling in two-dimensional photonic lattices,” in Nonlinear Guided Waves and Their Application (NLGW) 2005, OSA technical digest, paper ThD1 (2005)

[T06a] U. Peschel, H. Trompeter, T. Pertsch, and F. Lederer, „Light in Photonic Lattices,“ International Conference on Electronic and Photonic Materials, Devices and Systems (EPMDS), Calcutta India, invited (2006)

[T06b] H. Trompeter, T. Pertsch, F. Lederer, D. Michaelis, U. Streppel, A. Bräuer, and U. Peschel, „Visual observation of Zener tunnelling,“ Phys. Rev. Lett. **96**, 023901 (2006)

[T06c] H. Trompeter, W. Krolikowski, D. N. Neshev, A. S. Desyatnikov, A. A. Sokhorukov, Y. S. Kivshar, T. Pertsch, U. Peschel and F. Lederer, “Photonic Bloch oscillations and Zener tunnelling in two-dimensional optical lattices,” Phys. Rev. Lett. (in press)

Kurzfassung

Ein aktuelles Forschungsthema in der Optik ist die Lichtausbreitung in künstlichen Materialien, wie zum Beispiel in photonischen Kristallen oder Metamaterialien. Auch photonische Kristallfasern und Wellenleiterarrays gehören dieser Klasse von Systemen an. Im Rahmen dieser Arbeit werden Wellenleiterarrays untersucht. Unter Wellenleiterarrays werden dabei in einer oder beiden transversalen Richtungen periodisch wellenleitende Strukturen verstanden

Aufgrund ihrer Periodizität weisen Wellenleiterarrays viele Ähnlichkeiten mit anderen physikalischen Systemen aus der Quantenmechanik oder Festkörperphysik auf. Teilchen in periodischen Potentialen, z.B. Elektronen in Kristallen oder Super-Gittern oder Bose-Einstein-Kondensate in optischen Gittern, haben Energien die im Impulsraum auf so-genannte Bänder beschränkt sind. Diese Bänder werden durch Bandlücken voneinander getrennt. Analog dazu sind auch die Propagationskonstanten der Bloch-Wellen in Wellenleiterarrays in Bändern angeordnet. Dies ermöglicht, dass viele aus der Quantenmechanik bekannte Effekte auch in Wellenleiterarrays beobachtet werden können.

In der Vergangenheit wurde gezeigt, dass sich bereits in homogenen Wellenleiterarrays die Lichtausbreitung von derjenigen in homogenen Materialien deutlich unterscheidet [Pertsch02]. Erste Untersuchungen von inhomogenen Arrays ergaben, dass Bloch-Oszillationen beobachtet werden können, falls einer periodischen Struktur zusätzlich eine lineare Brechungsindexänderung in transversaler Richtung überlagert wird [Pertsch99a, Morandotti99].

In der vorliegenden Arbeit werden weitere theoretische und experimentelle Untersuchungen zur Ausbreitung von Licht in inhomogenen Wellenleiterarrays vorgestellt. Der Schwerpunkt liegt dabei auf der Untersuchung lokaler Inhomogenitäten (Kapitel 3) und dem experimentellen Nachweis von photonischem Zener-Tunneln (Kapitel 4 und 5).

Vor der Präsentation der Ergebnisse der theoretischen und experimentellen Untersuchungen, wird in Kapitel 1 eine Einleitung gegeben. In Kapitel 2 werden die grundlegenden Gleichungen zur theoretischen Untersuchung von Wellenleiterarrays vorgestellt. Ausgehend von den Maxwell'schen Gleichungen wird das Eigenwertproblem für planare Wellenleiterarrays hergeleitet und diskutiert.

In Kapitel 3 wird der Einfluss von Defekten und Grenzflächen auf die Lichtausbreitung in Wellenleiterarrays analysiert. Für theoretische Untersuchungen wird dabei die Theorie gekoppelter Moden angewendet. Dadurch können die Eigenschaften jedes einzelnen Wellenleiters durch die Propagationskonstante der in ihm geführten Mode und die Kopplung

zu Moden benachbarter Wellenleiter beschrieben werden. Um Defekte und Grenzflächen zu erzeugen, werden genau diese zwei Größen variiert. Die Existenz gebundener Zustände wird für einen Defekt, der aus einem einzelnen gestörten Wellenleiter innerhalb eines ansonsten homogenen Arrays besteht, theoretisch vorausgesagt und in Experimenten in Polymer-Wellenleiterarrays bestätigt. Sowohl für eine Vergrößerung der Koppelkonstante als auch für eine Änderung des effektiven Index des Defektwellenleiters treten Defektmoden auf. Abhängig von den Parametern können diese entweder eine konstante Phase oder Phasensprünge von π zwischen den Feldern in benachbarten Wellenleitern aufweisen. Bemerkenswert ist, dass auch in mehrmodigen Defekten nur symmetrische Moden existieren. Weiterhin wird gezeigt, dass Defekte, die keine Mode führen, abstoßend wirken. Als Anwendungsbeispiel für Defektmoden wird ein elektro-optische Element, das als Schalter oder steuerbarer Strahlteiler verwendet werden kann, theoretisch untersucht. Im letzten Teil von Kapitel 3 werden theoretische Untersuchungen zu Grenzflächen in Wellenleiterarrays vorgestellt. Es wird gezeigt, dass im Gegensatz zu Grenzflächen zwischen ansonsten homogenen dielektrischen Medien, im Array Grenzflächenmoden existieren können. Des Weiteren werden die Reflexions- und Transmissionskoeffizienten für Bloch-Wellen an Grenzflächen berechnet. Die untersuchten Effekte werden mit Hilfe der Bandstruktur interpretiert.

Im 4. Kapitel der Arbeit wird Zener-Tunneln in planaren Wellenleiterarrays untersucht. Zener-Tunneln ist ein Effekt, der ursprünglich in der Quantenmechanik vorhergesagt wurde. Wird ein Elektron in einem periodischen Potential einem zusätzlich überlagerten elektrischen Feld ausgesetzt, so führt es eine oszillierende Bewegung aus, die als Bloch-Oszillationen bekannt wurde. Dabei tunnelt es mit einer bestimmten Wahrscheinlichkeit in höhere Bänder der Struktur. In der Vergangenheit wurden bereits photonische Bloch-Oszillationen in Wellenleiterarrays demonstriert. In dieser Arbeit wird theoretisch und experimentell nachgewiesen, dass auch Zener-Tunneln in Wellenleiterarrays auftreten kann. Der Schwerpunkt liegt dabei auf der experimentellen Demonstration des Effektes. Dazu wurde ein neuer Aufbau entwickelt, der es ermöglicht die Lichtausbreitung innerhalb des Arrays zu beobachten. Hierfür wird die Fluoreszenz des Polymers, aus dem die Arrays hergestellt werden, mit einer CCD Kamera oberhalb der Probe detektiert. Unter dem Einfluss eines transversalen Brechungsindexgradienten führt ein Lichtbündel in einem Wellenleiterarray Bloch-Oszillationen aus, d.h. es folgt während der Ausbreitung einer oszillierenden Bewegung in transversaler Richtung. Wenn die Bandlücke zwischen dem ersten und zweiten Band des Arrays klein ist, koppelt periodisch Licht aus Bloch-Oszillationen im ersten Band in das zweite Band. Dieser Effekt ist das optische Analogon zu quantenmechanischem Zener-Tunneln. Die

präsentierten Ergebnisse stellen die erste direkte Beobachtung von Zener-Tunneln dar. Die Ergebnisse der Messungen zeigen dabei eine gute qualitative Übereinstimmung mit numerischen Simulationen.

Alle bisher existierenden experimentellen Untersuchungen zu Zener-Tunneln und Bloch-Oszillationen beschränken sich auf so genannte eindimensionale periodische Systeme, die nur in eine transversale Richtung periodisch sind. In Kapitel 5 werden erste experimentelle Beobachtungen dieser Effekte in zweidimensionalen (2D) Strukturen vorgestellt. Hierzu wird ein 2D-Gitter optisch in einen photorefraktiven Kristall induziert. Diesem wird ein näherungsweise linearer Brechungsindexverlauf überlagert, der ebenfalls optisch erzeugt wird. Um Bloch-Oszillationen und Zener-Tunneln zu beobachten wird die Intensitätsverteilung eines Teststrahls nach der Propagation durch die im Kristall erzeugte Struktur beobachtet. In den Experimenten können Bloch-Oszillationen und Zener-Tunneln in höhere Bänder beobachtet werden. Im Unterschied zu den Experimenten in planaren Wellenleiterarrays tritt im 2D Fall Tunneln in verschiedene Richtungen auf. Zusätzlich zur Intensitätsverteilung wird auch die Fouriertransformierte (Fernfeld) des Feldes am Kristallausgang gemessen. Dadurch kann die zu den Blochoszillationen gehörende Bewegung des Strahls innerhalb der ersten Brillouinzone erstmals direkt beobachtet werden. Zenertunneln tritt wie vorausgesagt beim Erreichen des Randes der ersten Brillouinzone auf, wo das Licht in drei Symmetriepunkten des Gitters tunnelt.

Acknowledgements

This work would not have been possible without the support of a number of people. It is a pleasure to express my sincere thanks toward them.

First of all I would like to thank my supervisors Professor Falk Lederer and Professor Ulf Peschel for the support and ideas they provided.

I owe special thanks to Dr. Dirk Michaelis for his consistent assistance and numerous stimulating discussions.

I would like to thank Dr. Andreas Bräuer for giving me access to the excellent facilities of the Fraunhofer Institute for Applied Optics and Precision Engineering and Professor Thomas Pertsch for his ideas and discussion concerning my experiments.

I am indebted to my supervisors and colleagues from The Australian National University, in particular Professor Wieslaw Krolikowski, Dr. Dragomir Neshev, Dr. Anton Desyatnikov, Dr. Andrey Sukhorukov and Professor Yuri Kivshar, for their support during my research period in Canberra and a wonderful time in Australia.

Furthermore I would like to thank all colleagues from the Institute of Condensed Matter Theory and Solid State Optics and from the Fraunhofer Institute for Applied Optics and Precision Engineering for the stimulating working atmosphere.

Last, but certainly not least, I would like to express my gratitude to Dr. Ulrich Streppel, not only for providing the samples, but also for his encouragements, understanding and moral support.

Ehrenwörtliche Erklärung

Ich erkläre hiermit ehrenwörtlich, dass ich die vorliegende Arbeit selbständig, ohne unzulässige Hilfe Dritter und ohne Benutzung anderer als der angegebenen Hilfsmittel und Literatur angefertigt habe. Die aus anderen Quellen direkt oder indirekt übernommenen Daten und Konzepte sind unter Angabe der Quellen gekennzeichnet.

Weitere Personen waren an der inhaltlich-materiellen Erstellung der vorliegenden Arbeit nicht beteiligt. Insbesondere habe ich hierfür nicht die entgeltliche Hilfe von Vermittlungs- bzw. Beratungsdiensten (Promotionsberater oder andere Personen) in Anspruch genommen. Niemand hat von mir unmittelbar oder mittelbar geldwerte Leistungen für Arbeiten erhalten, die im Zusammenhang mit dem Inhalt der vorgelegten Dissertation stehen.

Die Arbeit wurde bisher weder im In- noch im Ausland in gleicher oder ähnlicher Form einer anderen Prüfungsbehörde vorgelegt.

Die geltende Promotionsordnung der Physikalisch-Astronomischen Fakultät ist mir bekannt.

Ich versichere ehrenwörtlich, dass ich nach bestem Wissen die reine Wahrheit gesagt und nichts verschwiegen habe.

Jena, den 30.01.2006

Lebenslauf

Henrike Trompeter
09.04.1976 geboren in Detmold
1983-1996 Schulbesuch
1996 Abitur
1996-2002 Studium der Elektrotechnik an der
Universität-Gesamthochschule Paderborn
2001-2002 Diplomarbeit am Fraunhofer Institut für
Angewandte Optik und Feinmechanik
2002 Abschluss als Diplomingenieur der Elektrotechnik
2002-2006 Doktorandin an der Friedrich-Schiller-Universität Jena
2004-2005 Forschungsaufenthalt an der Australian National University

Jena, den 30.01.2006